NASA-CR-197449

FINAL
IN-71-CR
395860
P-81

Department of

Mechanical and Aerospace Engineering and Engineering Mechanics

DUCTED FAN ACOUSTIC RADIATION INCLUDING THE EFFECTS OF NONUNIFORM MEAN FLOW AND ACOUSTIC TREATMENT

Walter Eversman

Indranil Danda Roy

July 1993

Submitted to

NASA LEWIS RESEARCH CENTER
NAG 3-178

University of Missouri-Rolla

N95-16401

(NASA-CR-197449) DUCTED FAN ACOUSTIC RADIATION INCLUDING THE EFFECTS OF NONUNIFORM MEAN FLOW AND ACOUSTIC TREATMENT Final Technical Report, 31 Aug. 1981 - 30 Jun. 1993 (Missouri Univ.) 80 p

Unclas

G3/71 0033789

DUCTED FAN ACOUSTIC RADIATION INCLUDING THE EFFECTS OF NONUNIFORM MEAN FLOW AND ACOUSTIC TREATMENT

Walter Eversman and Indranil Danda Roy
Mechanical and Aerospace Engineering
and Engineering Mechanics
University of Missouri-Rolla
Rolla, Missouri 65401

ABSTRACT

Forward and aft acoustic propagation and radiation from a ducted fan is modelled using a finite element discretization of the acoustic field equations. The fan noise source is introduced as equivalent body forces representing distributed blade loading. The flow in and around the nacelle is assumed to be nonuniform, reflecting the effects of forward flight and flow into the inlet. Refraction due to the fan exit jet shear layer is not represented. Acoustic treatment on the inlet and exhaust duct surfaces provides a mechanism for attenuation. In a region enclosing the fan a pressure formulation is used with the assumption of locally uniform flow. Away from the fan a velocity potential formulation is used and the flow is assumed nonuniform but irrotational. A procedure is developed for matching the two regions by making use of local duct modal amplitudes as transition state variables and determining the amplitudes by enforcing natural boundary conditions at the interface between adjacent regions in which pressure and velocity potential are used. Simple models of rotor alone and rotor/exit guide vane generated noise are used to demonstrate the calculation of the radiated acoustic field and to show the effect of acoustic treatment. The model has been used to asses the success of four techniques for acoustic lining optimization in reducing far field noise.

INTRODUCTION

Figure 1 shows in idealized form a rotor/exit guide vane configuration imbedded in a nacelle with a centerbody or a core engine. The rotor represents the fan in a high bypass turbofan engine or a ducted propeller. The exit guide vanes provide a source of interaction noise. In the numerical examples considered in this investigation the number of blades and exit guide vanes is characteristic of a ducted propeller. The rotor/exit guide vane source generates noise which is propagated through the inlet and exhaust ducts and is radiated to the far field. Nonuniform steady flow exists in and around the nacelle due to inflow, outflow, and forward flight effects. It is required to predict the far field radiated noise at harmonics of the blade passage frequency.

In a previous investigation [1] ducted fan noise was studied with the assumption that the mean flow in and around the inlet could be assumed to be uniform. This allowed the

acoustic field equations to be simplified to a convected wave equation in the acoustic pressure. The fan noise source was introduced as equivalent body forces representing distributed blade loading. In the investigation reported here the flow in and around the nacelle is assumed to be nonuniform, reflecting the effects of forward flight and flow into the inlet. Refraction due to the fan exit jet shear layer is not accounted for in the current model. Nonuniform mean flow eliminates the possibility of using the convected wave equation as in Reference [1]. Nonuniform flow effects have been included in studies of forward radiated noise from turbofan inlets [2,3]. In this case the mean flow is assumed to be irrotational, as is the acoustic perturbation, and the introduction of a velocity potential simplifies the field equations. The fan noise source is introduced as a boundary condition on the fan face defining the amplitude of incident and reflected duct modes.

In order to ensure an efficient numerical model it is desirable to represent the acoustic field in terms of a single state variable. In the previous studies this was done in terms of the acoustic pressure or the velocity potential. In the extension discussed here the pressure formulation is not suitable because the mean flow is nonuniform in most of the region of propagation and radiation. The velocity potential formulation is not suitable for introducing the fan noise source as an equivalent body force distribution. For these reasons a mixed method is introduced. In the fan region a pressure formulation is used and away from the fan a velocity potential formulation is used. When pressure is used as the state variable in a region near the fan where it is assumed possible to consider a locally uniform flow, the fan noise source, either rotor alone noise, or interaction noise, can be introduced as equivalent body forces. In regions away from the fan where the mean flow is nonuniform but irrotational, a velocity potential description has proven to be appropriate. A procedure is developed for matching the two regions by making use of local duct modal amplitudes as transition state variables and determining the amplitudes by enforcing natural boundary conditions at the interface between adjacent regions in which pressure and velocity potential are used.

An additional feature introduced in the present study is the provision for modelling an acoustic lining on the surfaces of the fan inlet and exhaust ducts. The lining is assumed to be point reacting and to have a frequency dependent impedance or admittance. The lining representation is consistent with the physical characteristics of current acoustical materials.

The details of the introduction of the noise source have been discussed in [1]. In this paper the extension of the formulation of the finite element model required to admit nonuniform mean flow and acoustic treatment is explained. Results are presented for the far field radiated acoustic field for examples of rotor alone noise and for rotor/EGV interaction noise to demonstrate the cut off of subsonic tip speed rotor alone noise, the propagation of interaction tones, and the influence of acoustic treatment on the radiated field.

PROBLEM FORMULATION

In previous studies acoustic radiation from fan sources embedded in a shroud or duct has been modeled using two different formulations. In the case of forward radiated noise

from turbofan nacelles [2,3] the model was based on the assumption that the mean flow in and around the nacelle is irrotational and that the acoustic perturbation is also irrotational. This makes it possible to introduce mean flow and acoustic perturbation velocity potentials. The governing field equations are the linearized acoustic continuity equation and a linearized acoustic Bernoulli equation, written in terms of the acoustic potential and the acoustic pressure (or density). As shown in [2,3], the acoustic potential is the solution of

$$\frac{\partial \rho}{\partial t} + \nabla\cdot(\rho_r \nabla\phi + \rho \nabla\phi_r) = 0 \tag{1}$$

and

$$\rho = -\frac{\rho_r}{c_r^2}\left(\frac{\partial \phi}{\partial t} + \nabla\phi_r \cdot \nabla\phi\right) \tag{2}$$

where ϕ is the acoustic potential, ϕ_r is the local mean flow (reference) potential, ρ is the acoustic density, ρ_r is the local mean flow density, and c_r is the local speed of sound in the mean flow. All quantities are nondimensional with respect to the density in the far field, ρ_∞ , the speed of sound in the far field, c_∞ , and a reference length, R, which is the fan radius. The acoustic potential is nondimensional with respect to $c_\infty R$, and the acoustic pressure with respect to $\rho_\infty c_\infty^2$. Time is scaled with R/c_∞ . The fan or EGV source is input by specifying complex amplitudes of duct modes at a boundary of the computational domain designated as the source plane. In the acoustic potential formulation the option to describe the source in terms of equivalent volumetric forces within the computational domain does not appear to be available because of the use of the acoustic Bernoulli equation. The acoustic field equations (1) and (2) form the basis of the finite element models for acoustic radiation from turbofan inlets including the effect of forward flight developed in [2,3]. Comparisons of results with flight test data are described in [4].

Acoustic radiation from unshrouded propellers in a free field and in a wind tunnel environment has been investigated with the assumption that the mean flow field, representing the forward flight effect or the flow in the wind tunnel, is nearly uniform [5-8]. In this case the governing acoustic field equation is the convected wave equation in terms of the acoustic pressure

$$\nabla\cdot\left(\nabla p - \frac{M_r^2}{c_r^2}\frac{\partial p}{\partial x}\bar{i} - \rho_r \bar{f}\right) - 2\frac{M_r}{c_r^2}\frac{\partial^2 p}{\partial x \partial t} - \frac{1}{c_r^2}\frac{\partial^2 p}{\partial t^2} = 0 \tag{3}$$

The fan or EGV source is introduced by an equivalent distribution of body forces per unit mass $\bar{f}$ (referred to herein as volumetric force). Equation (3) is in nondimensional form with the body force nondimensionalized by c_∞^2/R . The volumetric forces have been derived from a simplified lifting line theory in Reference [1]. The appearance of c_r is due to the use of c_∞ in the definition of dimensionless variables. M_f/c_r is the local Mach number M_f. The rotor alone model considers the steady blade loading rotating with the blades, while the EGV noise considers stationary blades with unsteady loading produced by the sweeping of rotor wakes past the blades. While simplified in the details, this approach contains the essential physics of two principal types of turbomachinery noise.

The extension of the propeller acoustic radiation model to shrouded and ducted fans was done with the assumption that in this case also the entire flow field, both internal and external to the nacelle, is uniform [1]. This is probably acceptable for a shrouded propeller and for a very high bypass ratio ducted fan. For a more typical turbofan nacelle the assumption is clearly not satisfied. The physical appeal of the source model motivates the extension of the concept to include nonuniform mean flow. The virtue of the representation of the source is that it provides a direct link between blade loading and acoustic source strength and distribution. It is not required to specify the acoustic duct modal amplitudes produced by the source.

The approach used is a mixed method in which the region containing the noise source is a pressure formulation based on the convected wave equation (3), and away from the source the acoustic potential formulation of equations (1) and (2) provides the field equations. The only assumption required is that within the narrow source region it is sufficiently accurate to treat the mean flow as uniform. Figure 2 is a sketch of a fan or EGV blade row embedded in a nacelle, with flow moving from right to left. A finite element mesh based on quadrilateral elements in the axially symmetric geometry is shown superimposed on the nacelle fan inlet and fan exhaust ducts. Of particular interest in this discussion is a region near the blade row consisting of four columns of elements in which the field equation is based on pressure. The shaded column contains the acoustic volumetric forces describing the blade loading. In this narrow region the flow is taken as axially directed and uniform. Outside this region the potential formulation is used. The details of the finite element formulation in the pressure region are given in [5,6] and the corresponding development for the potential formulation is found in [2,3]. Reference [1] should be consulted for the source model.

The main issue to be resolved is the matching between the two regions. In order to see how this can be done it is necessary to reiterate the finite element procedure for the weak formulation of the two types of problems. In both cases a Galerkin weighted residual method is used. In the case of the convected wave equation a solution for the pressure field $p(x,r)e^{i(\eta t - m\theta)}$ is sought such that the weighted residual statement

$$\iiint_V W\{\nabla\cdot(\nabla p - \frac{M_r^2}{c_r^2}\frac{\partial p}{\partial x}\bar{i} - \rho_r\bar{f}) - 2i\eta_r\frac{M_r}{c_r^2}\frac{\partial p}{\partial x} + \frac{\eta_r^2}{c_r^2}p\}\,dV = 0 \tag{4}$$

for every member $W(x,r)e^{i(\eta_r t + m\theta)}$ of a complete set of functions. In equation (4) the harmonic time dependence of the source is explicitly represented by the nondimensional frequency η_r defined as $\omega R/c_\infty$. In the form shown the operations implied require that W(x,r) be piecewise continuous and that p(x,r) have a continuous first derivative, requirements which would lead to seeking solutions in a very restrictive class of functions. A weaker solution, one which admits the possibility of a solution in a less restrictive class of functions is obtained by integration by parts to yield the weighted residuals statement that solutions $p(x,r)e^{i(\eta_r t - m\theta)}$ from the class of continuous functions are sought which satisfy

$$\begin{aligned}\iiint_V \{\nabla W\cdot(\nabla p - \frac{M_r^2}{c_r^2}\frac{\partial p}{\partial x}\bar{i} - \rho_r\bar{f}) + 2i\eta_r\frac{M_r}{c_r^2}W\frac{\partial p}{\partial x} - \frac{\eta_r^2}{c_r^2}Wp\}\,dV \\ - \iint_S W(\nabla p - \frac{M_r^2}{c_r^2}\frac{\partial p}{\partial x}\bar{i})\cdot\bar{n}\,dS = 0\end{aligned} \tag{5}$$

for every member $W(x,r)e^{i(\eta_r t + m\theta)}$ of a set of continuous functions. The volume integral is over the domain in which the pressure formulation is used, and the surface integral is over the boundary of this domain. The unit normal $\bar{n}$ is directed out of the domain. The boundary integral introduced plays a significant role in the matching procedure.

In the case of the potential region the weak formulation seeks solutions $\phi(x,r)e^{i(\eta_r t - m\theta)}$ in the class of continuous functions which satisfy the weighted residual equation

$$\begin{aligned}\iiint_V \{\nabla W\cdot(\rho_r\nabla\phi + \nabla\phi_r\rho) - i\eta_r W\rho\}\,dV \\ - \iint_S W(\rho_r\nabla\phi + \nabla\phi_r\rho)\cdot\bar{n}\,dS = 0\end{aligned} \tag{6}$$

in which $\rho(x,r)e^{i(\eta_r t - m\theta)}$ is defined by equation (2), for every member $W(x,r)e^{i(\eta_r t + m\theta)}$

of a set of continuous functions. The boundary integral is important in the matching procedure.

The boundary integrals represent natural boundary conditions which must be imposed on the boundary of the domain. The use of the boundary integrals on the boundaries of the problem is discussed in [2]. These boundaries of the computational domain are shown in Figure 3. The far field boundary is at a large distance from the nacelle and is a non reflecting surface on which a radiation condition is applied [2,3]. This surface is the outer boundary of wave envelope elements which allow a transition from a fine mesh near the nacelle to a very coarse mesh in the far field. Most of the nacelle and centerbody surfaces are rigid, where the normal component of acoustic particle velocity vanishes. In the pressure region this corresponds to $\frac{\partial p}{\partial n} = 0$. With the additional condition that the flow is taken to be axially directed in the pressure region, it follows that $\bar{i} \cdot \bar{n} = 0$, so that the boundary integral vanishes. In the velocity potential region $\frac{\partial \phi}{\partial n} = 0$. In addition, the flow tangency condition requires that $\nabla \phi_r \cdot \bar{n} = 0$. The boundary integral vanishes in this case as well. A portion of the nacelle and centerbody is acoustically treated. On these surfaces an impedance relation is specified, as discussed later.

In the mixed formulation there are two domains, one in which pressure is the dependent variable, and one in which velocity potential is the dependent variable. The boundary integrals at the interface of the two domains represent the natural boundary conditions which one domain imposes on the other. For the pressure region this integral is

$$I_p = \mp \iint_S W(1 - \frac{M_r^2}{c_r^2}) \frac{\partial p}{\partial x} dS \tag{7}$$

The positive sign applies if the pressure region boundary has its normal in the positive x direction. The velocity potential region boundary integral is

$$I_V = \mp \rho_r \iint_S W\{(1 - \frac{M_r^2}{c_r^2}) \frac{\partial \phi}{\partial x} - i\eta_r \frac{M_r}{c_r^2} \phi\} dS \tag{8}$$

The sign choice is the same as noted for the pressure case. These integrals will form contributions to the "stiffness" matrices obtained in the finite element formulation for the elements on the boundary between the regions.

MATCHING OF SOLUTIONS

The matching at the interface between the two domains is accomplished by using the connection between pressure and velocity potential provided by combining equation (2) and the linearized equation of state $p = c_r^2 \rho$ to yield

$$p = -\rho_r (i\eta_r \phi + M_r \frac{\partial \phi}{\partial x}) = -\rho_r c_r (i\eta_f \phi + M_f \frac{\partial \phi}{\partial x}) \tag{9}$$

The nondimensional frequency η_f and Mach number M_f are defined relative to the local conditions at the interface, taken as those at the fan source.

At the interface the velocity potential is written as an expansion in terms of the local acoustic modes for the duct,

$$\phi = \sum_{i=1}^{M} [a_i \psi_1^+(r) e^{-ik_{x_i}^+ x} + b_i \psi_i^-(r) e^{-ik_{x_i}^- x}] \tag{10}$$

where the duct eigenfunctions $\psi_i^{\pm}(r)$ are computed using a finite element formulation at the interface cross section.

The duct eigenfunctions $\psi_i(r)$ are solutions of the Bessel equation and boundary conditions on the duct wall

$$\begin{aligned} &\frac{1}{r}\frac{d}{dr}(r\frac{d\psi}{dr}) + [\kappa^2 - \frac{m^2}{r^2}]\psi = 0 \\ &\frac{d\psi}{dr} = 0 \qquad r = \sigma \\ &\frac{d\psi}{dr} = 0 \qquad r = 1 \end{aligned} \tag{11}$$

σ is the nondimensional inner radius of the duct. The duct eigenfunctions are the same for upstream propagation and downstream propagation so that $\psi_1^+(r) = \psi_i^-(r) = \psi_i(r)$. The axial wave numbers $k_{x_i}^{\pm}$ are calculated from the duct eigenvalues κ_i according to

$$\frac{k_{x_i}^{\pm}}{\eta_f} = \frac{1}{(1-M_f^2)}\left[-M_f \pm \sqrt{1-(1-M_f^2)(\frac{\kappa_i}{\eta_f})^2}\right] \tag{12}$$

where the mach number M_f and the nondimensional frequency η_r are local values at the interface cross section. The eigenvalue problem posed by equations (11) and (12) is solved utilizing a finite element formulation on a one dimensional grid of quadratic elements which matches the grid used in the duct interior. This very robust routine produces eigenvalues and eigenfunctions of high accuracy which are completely consistent with the interior grid. Reference [9] provides some details of the procedure. Equation (9) then provides an expansion for the pressure at the interface in terms of the velocity potential modal amplitudes

$$p = -i\rho_r c_r \eta_f \sum_{i=1}^{M} [a_i \psi_i^+(r)(1-M_f\frac{k_{x_i}^+}{\eta_f})e^{-ik_{x_i}^+ x} + b_i \psi_i^-(r)(1-M_f\frac{k_{x_i}^-}{\eta_f})e^{-ik_{x_i}^- x}] \tag{13}$$

Equations (10) and (13) also provide expansions for terms in the integrands of equations (7) and (8)

$$(1-\frac{M_r^2}{c_r^2})\frac{\partial p}{\partial x} = -\rho_r c_r \eta_f^2 (1-M_f^2)\sum_{i=1}^{M}\left[a_i(1-M_f\frac{k_{x_i}^+}{\eta_f})(\frac{k_{x_i}^+}{\eta_f})\psi_i(r)e^{-ik_{x_i}^+ x} + b_i(1-M_f\frac{k_{x_i}^-}{\eta_f})(\frac{k_{x_i}^-}{\eta_f})\psi_i(r)e^{-ik_{x_i}^- x}\right] \tag{14}$$

$$(1-\frac{M_r^2}{c_r^2})\frac{\partial \phi}{\partial x} - i\eta_r\frac{M_r}{c_r^2}\phi = -i\rho_r\eta_f\sum_{i=1}^{M}\left\{a_i\left[(1-M_f^2)(\frac{k_{x_i}^+}{\eta_f})+M_f\right]\psi_i(r)e^{-ik_{x_i}^+ x} + b_i\left[(1-M_f^2)(\frac{k_{x_i}^-}{\eta_f})+M_f\right]\psi_i(r)e^{-ik_{x_i}^- x}\right\} \tag{15}$$

The expansions are written in vector-matrix form as

$$\phi = [\psi_i(r) \mid \psi_i(r)][e]\begin{Bmatrix} a \\ b \end{Bmatrix} \tag{16}$$

$$p = [\psi_i(r) \mid \psi_i(r)][\beta][e]\begin{Bmatrix} a \\ b \end{Bmatrix} \tag{17}$$

$$(1 - \frac{M_r^2}{c_r^2})\frac{\partial p}{\partial x} = -i[\psi_i(r) \mid \psi_i(r)][\gamma][e]\begin{Bmatrix} a \\ b \end{Bmatrix} \tag{18}$$

$$(1 - \frac{M_r^2}{c_r^2})\frac{\partial \phi}{\partial x} - i\eta_f \frac{M_r}{c_r^2}\phi = -i[\psi_i(r) \mid \psi_i(r)][\alpha][e]\begin{Bmatrix} a \\ b \end{Bmatrix} \tag{19}$$

The row matrix $[\psi(r)] = [\psi_i(r) \mid \psi_i(r)]$ has 2M columns constructed from the continuous eigenfunctions generated by the eigenvalue problem of equation (11). It is partitioned with two blocks of M columns of the eigenfunctions retained in the expansion. The diagonal square matrix $[e]$ of size 2M x 2M has elements e_{ii}^{+} ,$i = 1,M$ and e_{ii}^{-} ,$i = M+1,2M$, where

$$e_{ii}^{\pm} = e^{-ik_{x_i}^{\pm}x} \tag{20}$$

The diagonal square matrix $[\alpha]$ has elements α_{ii}^{+} ,$i = 1,M$, and α_{ii}^{-} ,$i = M+1,2M$, where

$$\alpha_{ii}^{\pm} = \rho_r \eta_f \left[(1 - M_f^2)(\frac{k_{x_i}^{\pm}}{\eta_f}) + M_f \right] \tag{21}$$

The diagonal square matrix $[\beta]$ has elements β_{ii}^{+} ,$i=1,M$, and β_{ii}^{-} ,$i=M+1,2M$, where

$$\beta_{ii}^{\pm} = -i\rho_r c_r \eta_f (1 - M_f \frac{k_{x_i}^{\pm}}{\eta_f}) \tag{22}$$

Finally, the diagonal square matrix $[\gamma]$ has elements γ_{ii}^{+} ,$i=1,M$, and γ_{ii}^{-} ,$i=M+1,2M$, where

$$\gamma_{ii}^{\pm} = -i\rho_r c_r \eta_f^2 (1 - M_f^2)(1 - M_f \frac{k_{x_i}^{\pm}}{\eta_f})(\frac{k_{x_i}^{\pm}}{\eta_f}) \tag{23}$$

The vector $\begin{Bmatrix} a \\ b \end{Bmatrix}$ is partitioned with the complex amplitudes a_i , i=1,M for right running acoustic modes and b_i , i=1,M for left running modes.

The finite element implementation of the Galerkin Method of Weighted Residuals (MWR) is characterized by interpolation within subdomains of the computational domain (elements) based on values of the field variable, pressure or velocity potential, at nodes of the elements. In the work reported here the elements are isoparametric quadrilaterals with eight nodes. This type of discretization provides continuity of the field variable at element boundaries, but does not produce solutions with continuous derivatives. This is consistent with the weak formulation. Each element contributes an element "stiffness matrix" to the set of linear equations whose solution yields the nodal values of the field variable.

Figure 4 shows the interface between a region of pressure and a region of velocity potential. The elements in the two regions which are on the boundary are the key to the matching of the solutions in the two regions. In Figure 4 the pressure elements have their right boundary on the interface and the potential elements have their left boundary on the interface. The continuity of the solution across the interface is accomplished by using the fact that both pressure and velocity potential at the interface can be expanded in terms of the duct acoustic modes appropriate to the geometry and flow conditions at the interface as described in equations (16) and (17). These finite eigenfunction expansions contain M duct modes in each direction. The value of M is chosen to include all propagating modes plus perhaps three to five cutoff modes to assure radial resolution of the pressure field.

The velocity potential element stiffness matrices on the boundary are transformed by using the discrete eigenvectors to form a transformation matrix such that

$$\{\phi\} = [\Psi_1]\begin{Bmatrix} a \\ b \\ \phi_i \end{Bmatrix} \tag{24}$$

where $\{\phi\}$, the vector of nodal values of the velocity potential for an element, are replaced by the modal amplitudes a_i , b_i and the nodal values of ϕ at the interior nodes ϕ_i in the element (nodes not on the boundary). A similar transformation is made for pressure elements

$$\{p\} = [\Psi_2]\begin{Bmatrix} p_i \\ a \\ b \end{Bmatrix} \tag{25}$$

The elements of $[\Psi_1]$ and $[\Psi_2]$ are constructed by using the discrete eigenvectors, sampled at the boundary nodes for the element, and by using the eigenvector expansions of equations (16) and (17). They are "modal matrices" which serve as transformations from nodal values of the field variable in the interior of the element and modal amplitudes to values of the field variable at all of the nodes. A similar interpretation can be given to an eigenfunction expansion of the weighting functions. The weighting function evaluated at the element nodes $\{W\}$ is obtained in velocity potential elements as

$$\{W\} = [\Psi_1]\begin{Bmatrix} a \\ b \\ W_i \end{Bmatrix} \tag{26}$$

and in pressure elements as

$$\{W\} = [\Psi_2]\begin{Bmatrix} W_i \\ a \\ b \end{Bmatrix} \tag{27}$$

The transformed element stiffness matrices are for pressure

$$\left[\kappa_p^e\right] = \left[\Psi_2\right]^T \left[k_p^e\right] \left[\Psi_2\right] \tag{28}$$

and for the velocity potential

$$\left[\kappa_v^e\right] = \left[\Psi_1\right]^T \left[k_v^e\right] \left[\Psi_1\right] \tag{29}$$

The right boundary of the pressure elements and the left boundary of the potential elements at the interface are now discretized in terms of the modal amplitudes a_i ,b_i . The assembly process is carried out on the basis that a_i and b_i on the pressure and potential elements are the same.

The element stiffness matrices on the boundary must be augmented by the addition of the boundary integrals. These integrals can be conveniently evaluated directly in terms of the modal amplitudes and interior nodal values. This is accomplished by using the eigenfunction expansions for the integrands given by equations (18) and (19). For example, consider the integral of equation (7) evaluated on the right boundary. It can be written

$$I_p = -(-i) \iint_S W \left[\psi(r)\right] \left[\gamma\right] \begin{Bmatrix} a \\ b \end{Bmatrix} dS \tag{30}$$

The integral of equation (8) evaluated on the left boundary is similarly written

$$I_v = +(-i) \iint_S W \left[\psi(r)\right] \left[\alpha\right] \begin{Bmatrix} a \\ b \end{Bmatrix} dS \tag{31}$$

The eigenfunctions $\psi_i(r)$, treated in the expansions as continuous functions of r, are known only in terms of their discrete values (eigenvectors) at the nodal points on the interface in the finite element eigenvalue problem described by equation (11). The row matrix of continuous eigenfunctions is obtained by interpolation of the corresponding discrete modal matrix $\left[\Psi\right] = \left[\Psi_i \middle| \Psi_i\right]$ of discrete eigenvectors according to

$$\left[\psi(r)\right] = \left[N_b\right] \left[\Psi\right] \tag{32}$$

where $[N_b]$ is the element interpolation matrix on the right boundary of a pressure element or left boundary of a potential element. In standard finite element procedure, $[N_b]$ produces a continuous version of a function on the boundary in terms of discrete values of the function at nodes on the boundary. The continuous weighting functions can also be obtained from discrete values at the nodes $\{W\}$. This is accomplished using the same interpolation matrix

$$W = [N_b]\{W\} \tag{33}$$

For pressure element weighting functions

$$\{W\} = [\Psi \mid \beta]\begin{Bmatrix} a \\ b \end{Bmatrix} \tag{34}$$

and for potential weighting functions

$$\{W\} = [\Psi]\begin{Bmatrix} a \\ b \end{Bmatrix} \tag{35}$$

The boundary integrals I_p and I_v can be written as

$$I_p = i[\beta]^T[\Psi]^T \int_S \int [N_b]^T [N_b] dS [\Psi \mid \gamma]\begin{Bmatrix} a \\ b \end{Bmatrix} \tag{36}$$

$$I_v = -i[\Psi]^T \int_S \int [N_b]^T [N_b] dS [\Psi \mid \alpha]\begin{Bmatrix} a \\ b \end{Bmatrix} \tag{37}$$

The element integral contributions are added to the element stiffness matrices prior to assembly. The addition of the boundary

integral contributions to the stiffness matrices for elements on the boundary can be simplified if additional "modal matrices" $[\Psi_3]$ and $[\Psi_4]$, constructed by using the discrete eigenvectors, sampled at the boundary nodes for the element, and by using the eigenvector expansions of equations (18) and (19), are introduced to relate internal nodal values of the field variables and modal amplitudes on the boundary to values of the field variables at the element nodes. Equations (36) and (37) can be rewritten as

$$I_p = i[\Psi_2]^T \int_S \int [N]^T [N] dS [\Psi_4] \begin{Bmatrix} p_i \\ a \\ b \end{Bmatrix} \tag{38}$$

$$I_v = -i[\Psi_1]^T \int_S \int [N]^T [N] dS [\Psi_3] \begin{Bmatrix} a \\ b \\ \phi_i \end{Bmatrix} \tag{39}$$

The interpolation matrix $[N]$ is the element interpolation matrix which produces a continuous function within an element in terms of the nodal values of the function. The advantage of this formulation is that the boundary contribution is the same dimension as the transformed stiffness matrix to which it is appended.

ACOUSTIC TREATMENT

No previously published studies of fan noise radiation have addressed the placement of acoustic treatment on the surfaces of the fan inlet and fan exhaust ducts. In the formulation described here provision has been made for acoustic treatment in the region in which the acoustic field is described in terms of the velocity potential. This excludes only a very small region in which the fan noise generation process is described in terms of a pressure formulation.

The boundary integral of equation (6) is the mechanism by which the boundary condition imposed by locally reacting acoustic treatment is introduced. On surfaces on which acoustic treatment is present the normal component of mean flow velocity vanishes and the lining boundary integral simplifies to

$$I_L = -\int_S \int \rho_r W v_n dS \tag{40}$$

where v_n is the acoustic particle velocity directed normally into the acoustic treatment. The acoustic treatment is described in terms of the impedance relationship

$$\frac{p}{\boldsymbol{v}\cdot\boldsymbol{n}} = z = \frac{1}{A} \tag{41}$$

p is the acoustic pressure and $\boldsymbol{v}\cdot\boldsymbol{n}$ is the normal component of lining velocity at the wall. The impedance z is a prescribed function of frequency and is nondimensional with respect to $\rho_\infty c_\infty$. A is defined as the nondimensional acoustic admittance. The relation between the fluid particle velocity at the wall and the wall velocity is one of continuity of particle displacement. This yields

$$v_n = \frac{\partial \zeta}{\partial t} + M_r \frac{\partial \zeta}{\partial x} \tag{42}$$

where $\zeta(x,\theta,t) = \zeta(x)e^{i(\eta_r t - m\theta)}$ is the normal component of wall displacement, directed into the wall, evaluated at the wall surface. It is assumed that all lined surfaces are nearly parallel to the duct axis of symmetry so that there are no high flow accelerations (particularly accelerations normal to the wall) in the lining region and so that the description of the lining displacement in terms of x is equivalent to a description in terms of the arc length along the wall. These assumptions are consistent with reality, and greatly simplify the lining model. Since $\boldsymbol{v}\cdot\boldsymbol{n} = \frac{\partial \zeta}{\partial t}$ it follows that with harmonic time dependence

$$v_n = (1 - i\frac{M_r}{\eta_r}\frac{\partial}{\partial x})\boldsymbol{v}\cdot\boldsymbol{n} \tag{43}$$

The relation between acoustic particle velocity and pressure is

$$v_n = (1 - i\frac{M_r}{\eta_r}\frac{\partial}{\partial x})Ap \tag{44}$$

The relation between pressure and acoustic velocity potential is provided by the acoustic Bernoulli equation of equation (9). Equation (44) can be rewritten

$$v_n = -i\eta_r\left(1 - i\frac{M_r}{\eta_r}\frac{\partial}{\partial x}\right)\left\{\rho_r A\left(\phi - i\frac{M_r}{\eta_r}\frac{\partial\phi}{\partial x}\right)\right\} \tag{45}$$

The boundary integral becomes

$$\begin{aligned} -\iint_S \rho_r W v_n dS &= i\eta_r \iint_S WA\rho_r^2\phi\, dS + \iint_S WA\rho_r^2 M_r \frac{\partial\phi}{\partial x} dS \\ &+ \iint_S W\rho_r M_r \frac{\partial}{\partial x}[A\rho_r\phi] dS - \frac{i}{\eta_r}\iint_S W\rho_r M_r \frac{\partial}{\partial x}\left[A\rho_r M_r \frac{\partial\phi}{\partial x}\right] dS \end{aligned} \tag{46}$$

The first two integrals on a boundary where acoustic treatment is present are easy to implement in the finite element formulation because only continuity of acoustic potential is required. The admittance, A, is assumed piecewise continuous. The third and fourth integrals have continuity problems because of A and $\partial\phi/\partial x$ and are not compatible with the weak formulation. However, integration by parts can be performed to reduce the continuity requirement. This process begins with the observation that

$$\begin{aligned} \iint_S W\rho_r M_r \frac{\partial}{\partial x}[A\rho_r\phi] dS &= \iint_S \frac{\partial}{\partial x}\left[WA\rho_r^2 M_r\phi\right] dS \\ &- \iint_S \frac{\partial}{\partial x}[W\rho_r M_r]\left[A\rho_r M_r \frac{\partial\phi}{\partial x}\right] dS \end{aligned} \tag{47}$$

and

$$\begin{aligned} \frac{i}{\eta_r}\iint_S W\rho_r M_r \frac{\partial}{\partial x}\left[A\rho_r M_r \frac{\partial\phi}{\partial x}\right] dS &= \frac{i}{\eta_r}\iint_S \frac{\partial}{\partial x}\left[WA\rho_r^2 M_r^2 \frac{\partial\phi}{\partial x}\right] dS \\ &- \frac{i}{\eta_r}\iint_S \frac{\partial}{\partial x}[W\rho_r M_r]\left[A\rho_r M_r \frac{\partial\phi}{\partial x}\right] dS \end{aligned} \tag{48}$$

Stokes' Theorem for non-planar surfaces is

$$\iint_S curl\bar{V}\cdot\bar{n}dS = \oint \bar{V}\cdot d\bar{l} \tag{49}$$

where $\bar{n}$ is the normal to S and $d\bar{l}$ is the incremental line element on the curve C bounding S. The first integrals in equations (47) and (48) become

$$\iint_S \frac{\partial}{\partial x}\left[WA\rho_r^2 M_r \phi\right]dS = \oint\left[WA\rho_r^2 M_r \phi\right]dl \tag{50}$$

$$\frac{i}{\eta_r}\iint_S \frac{\partial}{\partial x}\left[WA\rho_r^2 M_r^2 \frac{\partial \phi}{\partial x}\right]dS = \frac{i}{\eta_r}\oint\left[WA\rho_r^2 M_r^2 \frac{\partial \phi}{\partial x}\right]dl \tag{51}$$

In arriving at equations (50) and (51) advantage was taken of the fact that the surfaces on which acoustic lining is present are very nearly cylindrical. The bounding curve C is considered to consist of segments parallel to the duct axis and circular arcs bounding the lined region. The integrals on the line segments parallel to the duct axis cancel because of continuity considerations. The bounding circular arcs are chosen to be located just outside the lined region so that the admittance vanishes. With these arguments the line integrals discarded. The weak formulation for the boundary condition on the acoustically treated surface can now be written

$$\begin{aligned} -\iint_S \rho_r W v_n dS &= i\eta_r \iint_S WA\rho_r^2 \phi dS + \iint_S WA\rho_r^2 M_r \frac{\partial \phi}{\partial x} dS \\ &\quad - \iint_S \frac{\partial}{\partial x}\left[W\rho_r M_r\right]\left[A\rho_r \phi\right]dS + \frac{i}{\eta_r}\iint_S \frac{\partial}{\partial x}\left[W\rho_r M_r\right]\left[A\rho_r M_r \frac{\partial \phi}{\partial x}\right]dS \end{aligned} \tag{52}$$

Equation (52) is in a form which is appropriate for application of standard finite element techniques to generate "boundary matrices" which are appended to the element stiffness matrices of elements whose outer boundaries represent acoustically treated surfaces.

SOLUTION METHOD

When the matching procedure is carried out and assembly is accomplished by standard finite element methods, the acoustic field is discretized in terms of nodal values of pressure in the pressure elements, nodal values of velocity potential in the potential elements, and amplitudes of the duct acoustic modes at the interfaces. The force integral I_f is produced by the evaluation of the weighted residual volume integral

$$I_f = \rho_r \iiint_V \nabla W \cdot \bar{f} dV \tag{53}$$

formed in the pressure elements in which the blade force distribution $\{f_b\}$ is defined at the element nodes [1].

The nodal values of pressure or velocity potential can be recovered from the modal amplitudes at the interfaces by post processing using the transformations described. The modal amplitudes are themselves useful information as they can be used to quantify the acoustic modes generated by the source and reflected from the fan inlet or and exhaust exits. All other aspects of the implementation of the finite element method are the same as described in connection with previous work [1,2,3,9].

The set of algebraic equations which arises from the finite element formulation is solved by using the frontal solution method of Irons [10], modified to deal with unsymmetric problems. Solutions have been obtained with over 20,000 degrees of freedom (nodes) with good success.

GEOMETRY AND FLOW FIELD CALCULATIONS

In Reference [1] it was assumed that the mean flow field is everywhere uniform. In addition to simplification of the acoustic field equations, this eliminated the complication of producing input data for a nonuniform mean flow field. In the present formulation the nonuniform flow field is required to be known. In previous studies of turbofan inlet noise radiation [2-4] it was noted that this data was obtained from a finite element formulation for incompressible potential flow based on the same mesh as the acoustic calculations. This potential flow code has been extended to the geometry of the simultaneous forward and aft radiation problem which now arises. The issue of the shear layer which is present at the boundary of the exhaust jet and the surrounding flow is not addressed in this study. Also not included in the model are energy and momentum jumps in the mean flow field which occur across the rotor. In the last case, a much more detailed analysis of the noise generation mechanism would be required to include this in a rigorous way.

An automated mesh generation procedure which was developed for the inlet radiation has been extended to cover the forward and aft radiation geometry required in the new formulation. The mesh is constructed from input data which describes the nacelle and

centerbody.

VERIFICATION OF THE COUPLING SCHEME

The technique used to couple the pressure region and the velocity potential region requires verification. In order to do this, a uniform duct example has been considered in which the duct terminations have been made reflection free by use of a mode matching procedure not unlike the scheme described here for the coupling of the two regions [6]. Figure 5 shows the example with a region in the center of the duct in which the propagation is described by the pressure formulation. The remainder of the duct is represented by a velocity potential formulation. At the downstream end of the duct (x=0) a single acoustic mode propagating in the positive x direction is introduced. The reflected mode amplitudes at x=0 and the transmitted mode amplitudes at x=1 are computed. The expected result is the absence of reflected modes and the presence at x=1 of only the incident wave. This tests not only the scattering introduced by the coupling procedure but also that caused by the reflection free termination formulation.

Table 1 provides results which are typical. In this case an angular mode m=10 with the first radial mode n=1 at nondimensional frequency $\eta_r = 20$ is introduced at x=0 with unit pressure amplitude. There are three radial modes which are propagating. The table shows the first five incident, reflected and transmitted velocity potential modal coefficients. The largest reflected mode coefficient amplitude, which is the reflection of the incident mode, is .009 % of the incident mode coefficient amplitude. The transmitted modal coefficient corresponding to the introduced mode is very close to the result which would be obtained analytically by accounting for the phase shift introduced by the phase term $e^{-ik_{x_1}^{+}l}$. $k_{x_1}^{+}$ is the axial wave number for the first radial mode and l is the duct section length.

A second example in which the third radial mode is introduced produces even better results. This is not unexpected because the effective wave length is longer than for the lower order modes and the discretization errors associated with mesh refinement should be less critical. The maximum reflected modal coefficient amplitude is .0006 % of the input amplitude and the complex modal coefficient for the transmitted mode is again very close to the analytical result. These calculations are shown in Table 2.

The calculations described were based on a finite element mesh which was chosen to be refined enough to cope with the specified frequency. Numerical experiments have shown that five elements per wave length (accounting for Doppler effects) is reasonable and the results here are consistent with this rule of thumb.

The conclusion to be drawn here is that the mechanics of the coupling procedure as described are sound, producing spurious scattering only to a level which can be related to discretization errors and errors introduced by using a coupling procedure and an anechoic termination model based on finite acoustic mode expansions.

Table 1 Verification of Coupling - First Radial Mode
Angular Mode m = 10
Frequency η_r = 20
Flow Mach M = -0.30
L/R = 0.4

Mode	Incident Coefficient	Reflected Amplitude	Transmitted Amplitude	Transmitted Coefficient	Transmitted Coefficient (Th.)
1	0.00 + i 0.365(-1)	0.30(-5)	0.365(-1)	-0.168(-1) - i 0.324(-1)	-0.171(-1) - i 0.322(-1)
2		0.98(-8)	0.42(-6)		
3		0.47(-8)	0.83(-7)		

Table 2 Verification of Coupling - Third Radial Mode
Angular Mode m = 10
Frequency η_r = 20
Flow Mach M = -0.30
L/R = 0.4

Mode	Incident Coefficient	Reflected Amplitude	Transmitted Amplitude	Transmitted Coefficient	Transmitted Coefficient (Th.)
1		0.86(-8)	0.19(-7)		
2		0.21(-7)	0.43(-6)		
3	0.00 + i 0.422(-1)	0.60(-9)	0.422(-1)	-0.409(-1) + i 0.101(-1)	-0.409(-1) + i 0.104(-1)
4		0.26(-6)	0.27(-8)		
5		0.28(-7)	0.43(-9)		

ACOUSTIC LINING PARAMETERS

In carrying out calculations to demonstrate the effect of acoustic treatment on the far field acoustic radiation it is necessary to choose suitable admittance values. This has been done by using a lining optimization code which uses a Simplex scheme to determine the optimum impedance for a uniform duct. Optimization can be done by seeking the maximum attenuation in a given mode (the equivalent to the "Cremer" optimum [11] when mean flow is present), or on the basis of power attenuation with several choices of modal amplitude distribution. The choices in the code are (a) The "Cremer" optimum; (b) specified modal amplitudes and optimization on the basis of transmitted acoustic power; (c) equal modal amplitudes and optimization on the basis of transmitted acoustic power; and (d) equal modal power and optimization based on transmitted acoustic power. In the present study we have used the "Cremer" optimum based on the first radial mode, two specified modal coefficients defined by the source model, and the equal modal amplitude and equal modal power assumptions for sample calculations. The duct has been taken as annular with the radius ratio at the fan, and the acoustic treatment on the inner and outer walls is the same. For the cases involving transmitted power the lining length has been taken as 60 % of the fan radius. The lining design is constrained by the requirement that the real part of the normalized admittance be greater than zero and less than one. This restriction on the maximum value of the admittance, which has been used to demonstrate the optimization capability, limits the effectiveness of the exhaust duct lining. The Mach number is taken as that at the fan face. The frequency and angular mode number are chosen according to the characteristics of the source. Table 3 provides the admittances for the inlet and exhaust ducts for the four cases.

Table 3 Optimum Admittances
Inlet Mach = 0.4
Exhaust Mach = 0.4
Radius Ratio = 0.3
Angular Mode m = 1
Frequency η_r = 6.40
Frequency η_f = 6.44
Propagating modes: 2 inlet and exhaust
Constraint: 0.0 < Real[admittance] < 1.0

	Radial Mode 1	Specified Coefficients	Equal Amplitudes	Equal Power
Inlet	0.22 + i 0.45	0.68 + i 0.30	0.10 + i 0.38	0.18 + i 0.39
Exhaust	1.00 + i 0.82	0.97 + i 0.35	1.00 + i 0.98	1.00 + i 0.22

COMPUTATIONAL RESULTS

Example calculations will be shown for EGV interaction noise for a ducted fan. The principal feature which will be addressed is the attenuation predicted in the far field due to the insertion of acoustic treatment in the inlet and exhaust ducts of an inlet of simplified geometry. The geometry is for a model scale ducted fan with radius 0.311 m (1.02 ft). The blade chord is uniform at 0.052 m (0.17 ft). A nondimensional rotor angular velocity of η_r =0.8 is for a case of subsonic tip speed. At a speed of sound of 344 m/sec (1128 ft/sec) this corresponds to a rotor rotational speed of 8448 RPM. The geometry of the simple nacelle is shown in Figure 6. The forward flight speed of the nacelle is M=0.3 and the flow entering and leaving the fan is M=0.4. In the EGV case considered here there are eight blades on the fan and seven exit guide vanes. The interaction mode number is m=1. The nondimensional frequency at the fan plane is η_f = 6.44 which produces two propagating modes in both the inlet and exhaust ducts.

Calculations have been made for the case of untreated walls in the inlet and exhaust duct and for four cases of optimal acoustic treatment on the duct and centerbody in the inlet and exhaust ducts. As noted previously, the four methods of optimization depend on how the modal amplitudes are chosen. The classical, or "Cremer Optimum", is obtained by seeking the impedance which will maximize the attenuation in a particular mode. This occurs when two modal attenuations coalesce. In the present study the first radial mode is chosen and the optimization process maximizes the attenuation in the least attenuated mode. The remaining three optimal treatments depend on the choice of the mix of modal amplitudes and a maximum decrease of acoustic power in a specified duct length is the objective of the optimization. As a consequence of the matching of pressure and potential regions of the solution, the source acoustic modal amplitudes are available. These are used to determine the optimal impedance for the case of known amplitudes. The other two cases of equal modal amplitudes and equal modal acoustic power circumvent the necessity of knowledge of the modal structure of the source. The lining length in both the inlet and exhaust ducts is 60 % of the fan radius on the nacelle and 87 % of the fan radius on the centerbody. The calculations in this example will shed some light on the most appropriate way to choose the optimal acoustic treatment for this configuration.

The mesh for the example calculation is shown in Figure 7. The most important feature to note is the outer boundary of the computational domain which is a circle with center offset in the direction of the flow approaching the inlet. This is a constant phase surface for an apparent acoustic source at the origin, consistent with the use of wave envelope elements in the outer reaches of the domain to economically introduce the reflection free condition at "infinity".

Figure 8 is a plot showing contours of constant sound pressure level around the nacelle in a plane through the axis of symmetry for the case when there is no acoustic treatment. It shows the presence of two lobes in both the forward and aft radiated fields. In the region of 90 degrees to the axis of symmetry other lobes appear which are the result of diffraction and interference between the forward and aft radiated fields. The peak of the forward radiated noise is about 2 dB less than the aft radiated noise (this observation is

more clearly seen in Figure 10). The contours near the inlet tend to be slightly ragged due to postprocessing velocity potential data at the element nodes to obtain pressure. The pressure requires derivatives of the velocity potential and it is known that the weak formulation does not ensure continuity of derivatives on element boundaries. A superior postprocessing procedure computes the pressure at Gauss points within the elements where continuity is assured. This has not been done in this investigation because the contour plotting software requires nodal values of pressure. In Reference [9] the more accurate scheme was used and shown to generate better contours. It is interesting to note that the contours are more smooth in the wave envelope region where interpolation includes the wave structure.

When acoustic treatment is present the radiated sound field is considerably altered. Figure 9 shows the result when the "Cremer" optimum is used. The optimization process indicates that the exhaust duct lining is only about 25 % as effective as the inlet lining (in terms of dB per unit length attenuation). While the contours in Figure 9 are not identified quantitatively, it is found that the acoustic field in the forward arc now has a distinct single lobe, and this lobe is down more than 10 dB relative to the aft radiated noise which has had its peak level reduced by about 7 dB due to acoustic treatment. The aft radiated noise now has a broad single peak. Quantitative observations are more easily deduced from Figure 10.

Figure 10 is the polar directivity of the radiated acoustic field on a circle with radius of 10 fan radii. The five cases are shown on this plot with the largest Sound Pressure Level normalized to 100 dB. The scale level shown of 105.97 dB indicates the highest SPL, so that the actual level on any of the curves is obtained by adding 5.97 dB. The radiation pattern in the unlined case can be compared to Figure 8 to identify lobes and to quantify the levels. The characteristics of the level curves in Figure 9 can also be identified on Figure 10. Due to the low angular mode number, $m=1$, the acoustic field has its maximum levels at relatively low angles from the axis of symmetry.

The four cases of duct acoustic treatment show generally similar effects on the acoustic far field. Both attenuation and shift in location of the lobes is a characteristic of all four cases. One could view attenuation as the decrease in SPL in easily identifiable lobes, regardless of angular shifts in the lobes. This would provide the most optimistic definition because it would obscure the fact that the new lobes might move into previously low SPL regions. The definition of attenuation adopted here will be the decrease of SPL at a specific polar angle. This is the most conservative definition because it is adversely affected by low SPL levels in the field for the untreated nacelle. For this fan configuration two choices of optimization philosophy appear to produce superior results for attenuation in the far field. The "Cremer" optimum and the equal modal amplitude scheme give generally good results in the entire field, with the attenuation being 10 dB or more for forward radiated noise and sideline attenuation in the same range except for isolated angular locations. In the case of aft radiated noise the attenuation is 7 or 8 dB except in the neighborhood of 150 degrees where an interference dip in the unattenuated field is present. The equal power choice does well in the forward region but does not do as well in the aft region. It is surprising that the specification of modal amplitudes in the optimization scheme is the least successful of the four choices. One can rationalize this by noting that the design procedure focuses on a section of an infinitely long lining. Scattering due to the leading and trailing edges of the

lining is not present and input modal amplitudes are not altered by this scattering. These results can not be taken as general because of the constrained range of the real part of the admittance, and because of the modal structure of the source, which has only two propagating radial modes, both of which are strongly affected by the "Cremer" procedure. In fact, the two modes tend to coalesce, accounting for the loss of the distinctness in the far field lobes in the directivity. It might be expected that if many modes are propagating different conclusions would be made.

CONCLUSIONS

The finite element modeling of ducted fan acoustic radiation has been extended to include a source which represents the loading on rotating or stationary blades. The loading is introduced by volumetric forces in the acoustic field equations written in a pressure formulation for a small region in which the flow is uniform. Away from this source region an acoustic velocity potential formulation is used which includes the effects of a nonuniform mean flow field due to inlet flow and forward flight effects. The two regions are coupled by using the transition between acoustic velocity potential and pressure which is available in an acoustic Bernoulli equation. At the interface between the regions eigenfunction expansions are used to express both pressure and acoustic velocity potential in terms of modal amplitude coefficients which become unknowns in the finite element formulation. The matching at the interface also requires the appending of the natural boundary conditions which are appropriate for the two regions. A consequence of the matching procedure is that the modal amplitudes are calculated as part of the solution, thus providing information on the duct modes generated by the source. Knowledge of the modal amplitudes is useful for the design of optimum acoustic treatment. The mechanics of the matching procedure has been tested in an example calculation and it is found that scattering at the interface is well within other sources of computational error associated with the FEM.

An additional extension of the FEM model is the provision for the acoustic treatment of the surfaces of the nacelle and centerbody. Designated acoustic admittances can be used in a model of a locally reacting acoustic lining in both the inlet duct and exhaust duct.

Example calculations have been made for the case of EGV interaction noise to investigate the effectiveness of acoustic treatment which is specified on the basis of several forms of optimization criteria. It is found that an optimum admittance based on the "Cremer" optimization or by the choice of equal modal amplitudes provides the best far field performance. Because of the complex nature of the propagation and radiation, the result must be considered as specific to the configuration in this example. Calculation of the radiated field provides a useful supplement to acoustic design techniques based on infinite duct theory.

ACKNOWLEDGEMENT

The work reported here is the result of support provided by a grant from NASA Lewis Research Center.

REFERENCES

1. W. Eversman 1992 Paper DGLR/AIAA 92-02-139, DGLR/AIAA 14th Aeroacoustics Conference, May 11-14,1992, Aachen, Federal Republic of Germany. Radiated noise of ducted fans.
2. W. Eversman, A. V. Parrett, J. S. Preisser, and R. J. Silcox 1985 ASME Journal of Vibration, Acoustics, Stress, and Reliability in Design 107(2), 216-223. Contributions to the finite element solution of the fan noise radiation problem.

3. A. V. Parrett and W. Eversman 1986 AIAA Journal 24(5), 753-760.Wave envelope and finite element approximations for turbofan noise radiation in flight.

4. J. S. Preisser, R. J. Silcox, W. Eversman, and A. V. Parrett 1985 Journal of Aircraft 22(1), 57-62. Flight study of induced turbofan inlet acoustic radiation with theoretical comparisons.

5. W. Eversman and J. E. Steck 1986 Journal of Aircraft 23(4),275-282. Finite element modeling of acoustic singularities with application to propeller noise.

6. W. Eversman and K. J. Baumeister 1986 Journal of Aircraft 23(6), 455-463. Modeling of wind tunnel wall effects on the radiation characteristics of acoustic sources.

7. K. J. Baumeister and W. Eversman 1989 Journal of Propulsion and Power 5(1), 55-63. Effects of wind tunnel wall absorption on acoustic radiation of propellers.

8. W. Eversman 1990 Journal of Aircraft 27(10), 851-858. Analytical study of wind tunnel acoustic testing of propellers.

9. I. Danda Roy and W. Eversman 1993 Improved finite element modeling of the turbofan engine inlet radiation problem. Journal of Vibration and Acoustics (in review).

10. B. M. Irons 1970 International Journal for Numerical Methods in Engineering 2, 5-32. A frontal solution program for finite element analysis.

11. L. Cremer 1953 Acoustica 3, 249-263. Theorie der Luftschall-Dampfung in Rechtekkanal mit Schluckender Wand und das sich dabei Ergebende hochste Dampfungsmass.

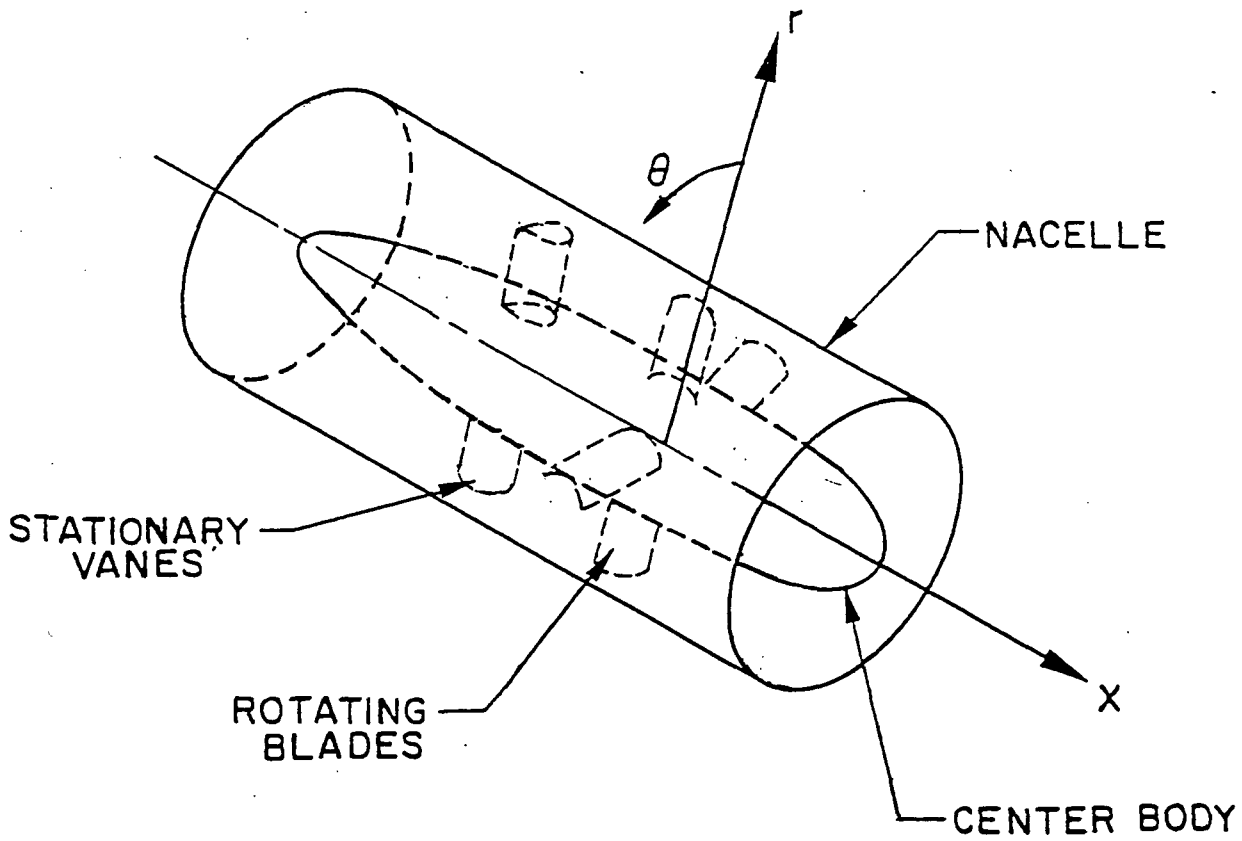

Figure 1. Idealized view of rotor/EGV imbedded in a nacelle with a centerbody.

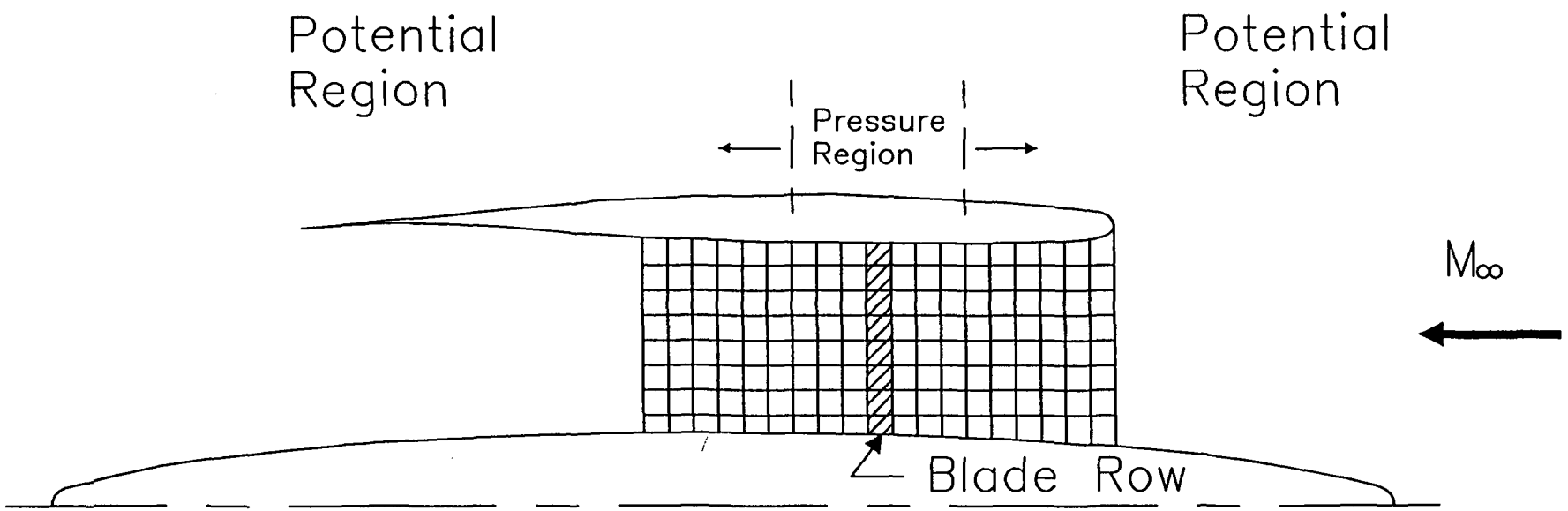

Figure 2. View of the inlet and exhaust ducts showing the pressure region near the blade row and the potential region away from the blade row.

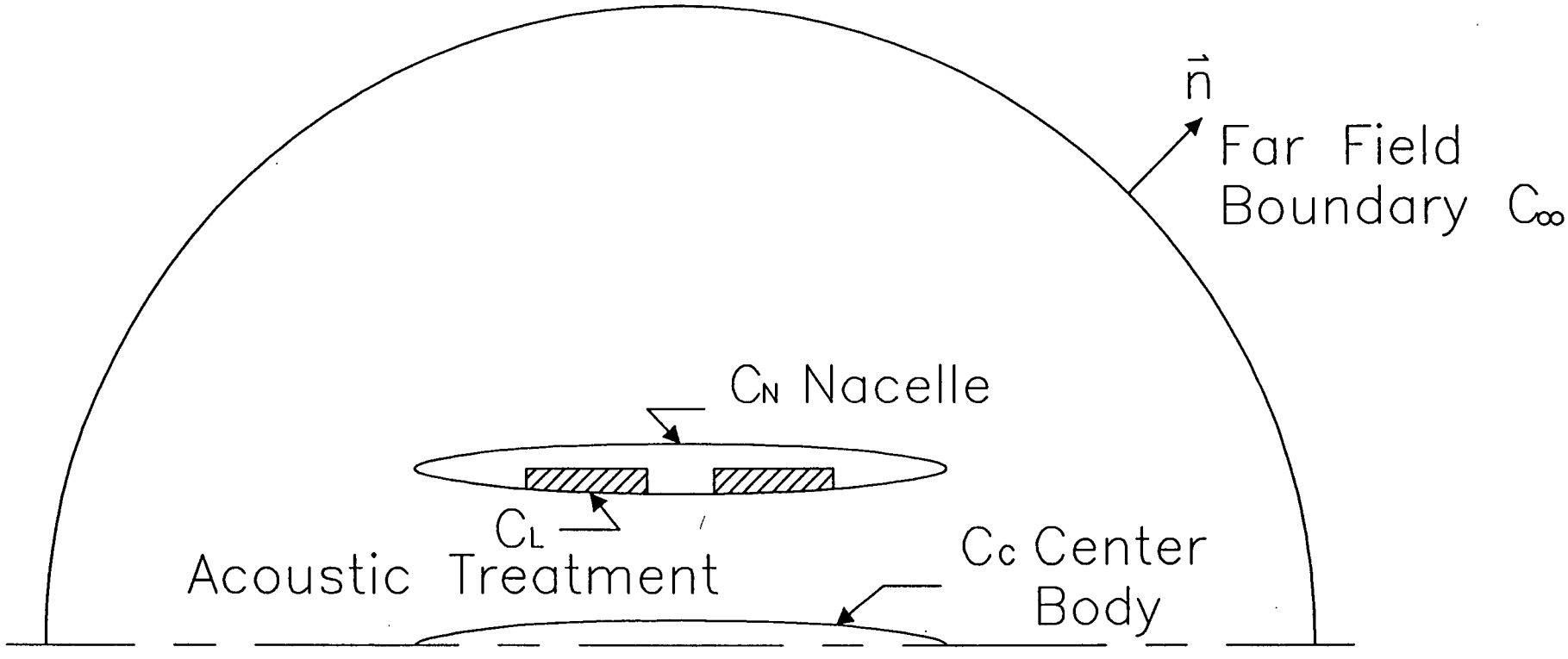

Figure 3. Boundaries of the computational domain showing the center body, nacelle with acoustically treated areas, and far field boundary.

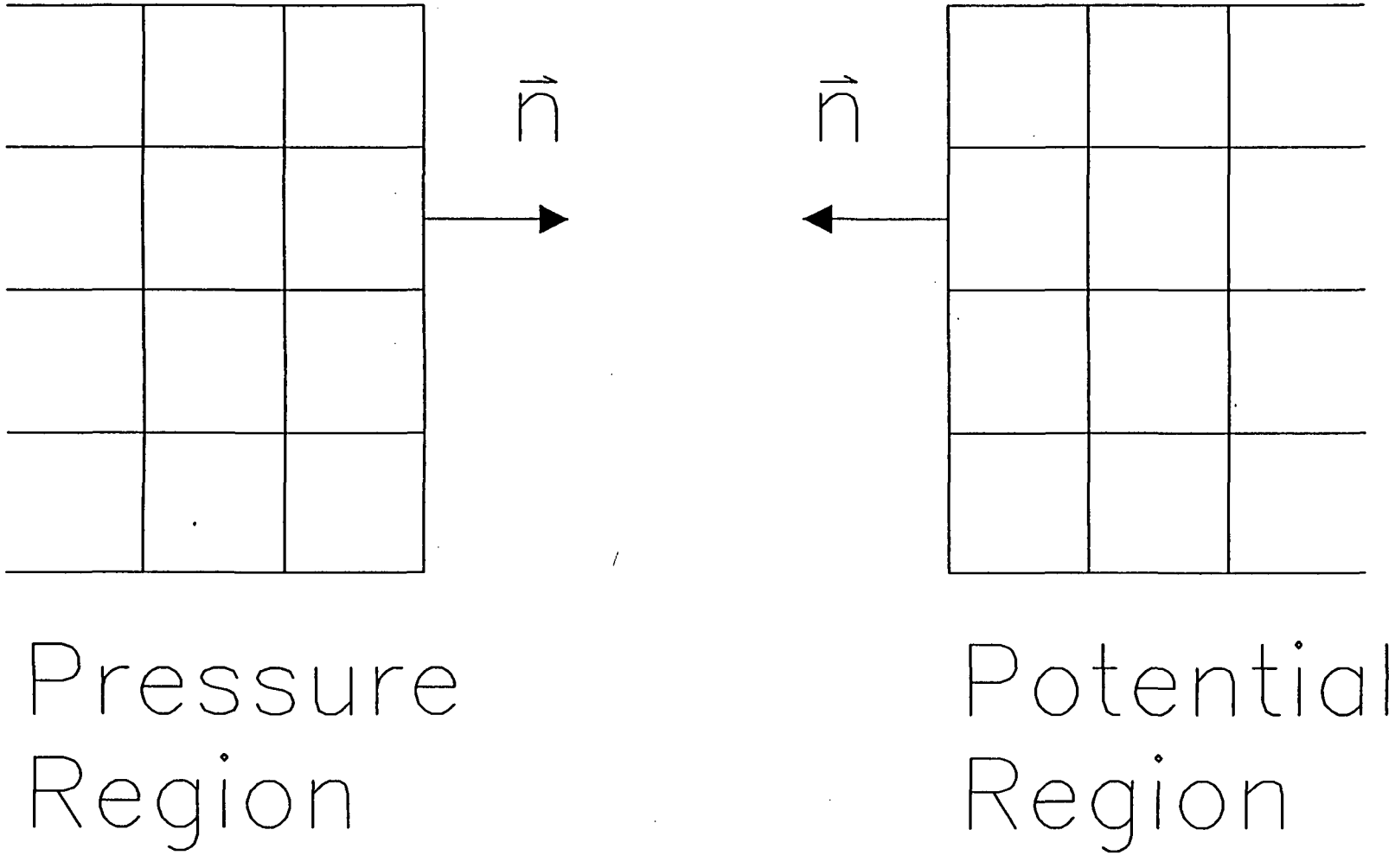

Figure 4. Interface of a pressure region and a potential region emphasizing the outward normals to the surfaces on which natural boundary conditions apply.

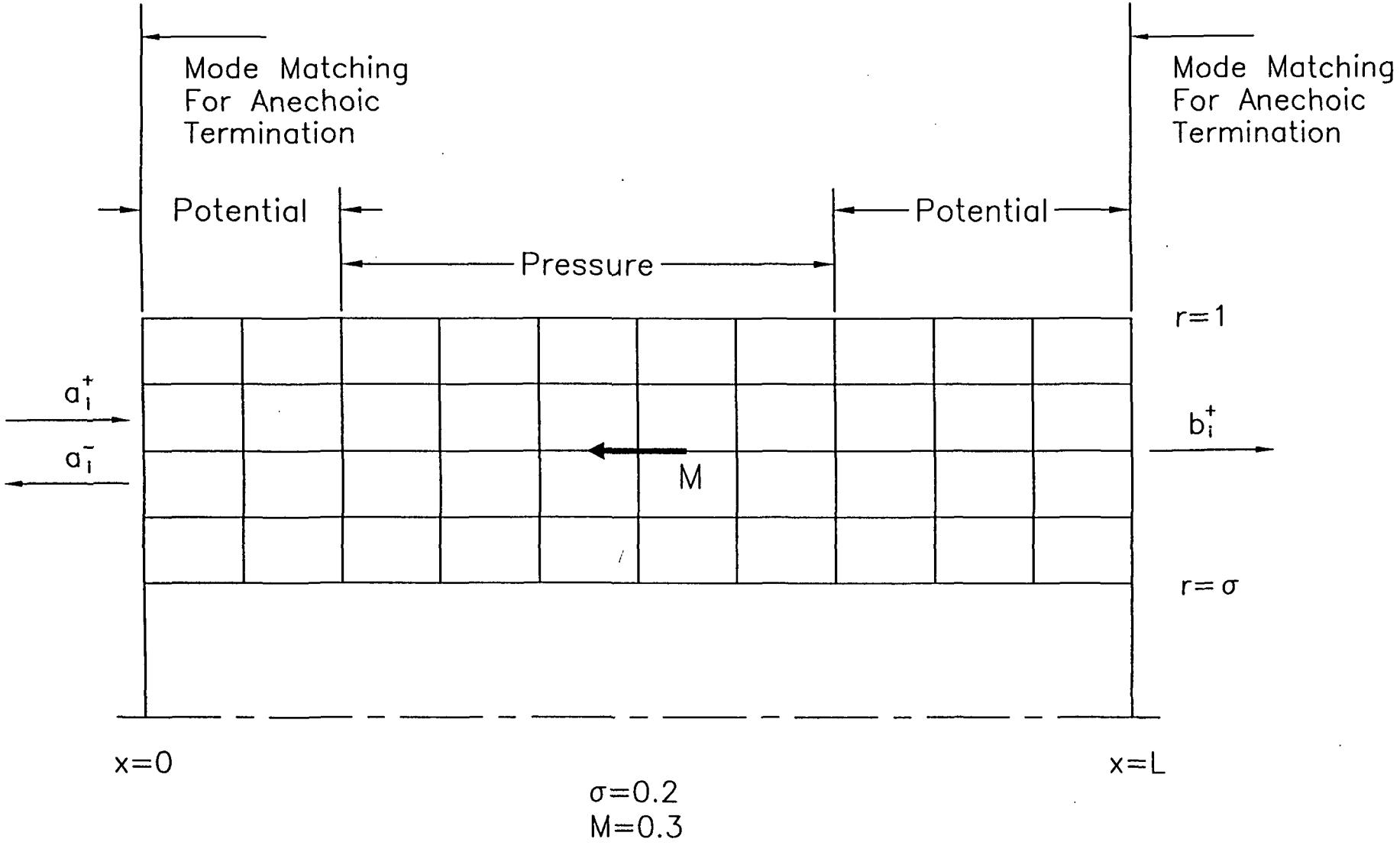

Figure 5. Annular computational region used to test coupling procedure for pressure and potential regions.

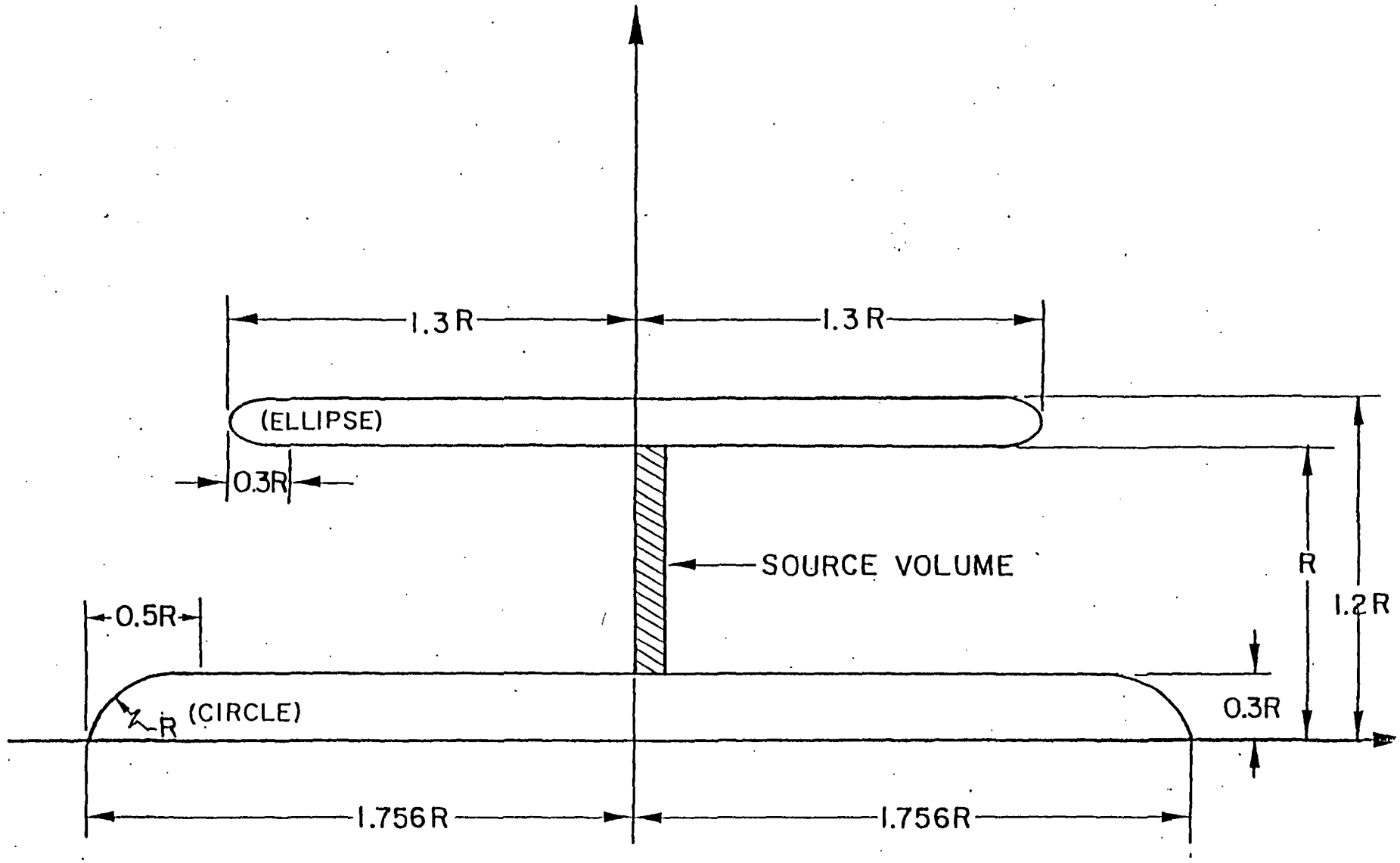

Figure 6. Geometry of simple nacelle shape used in example calculations.

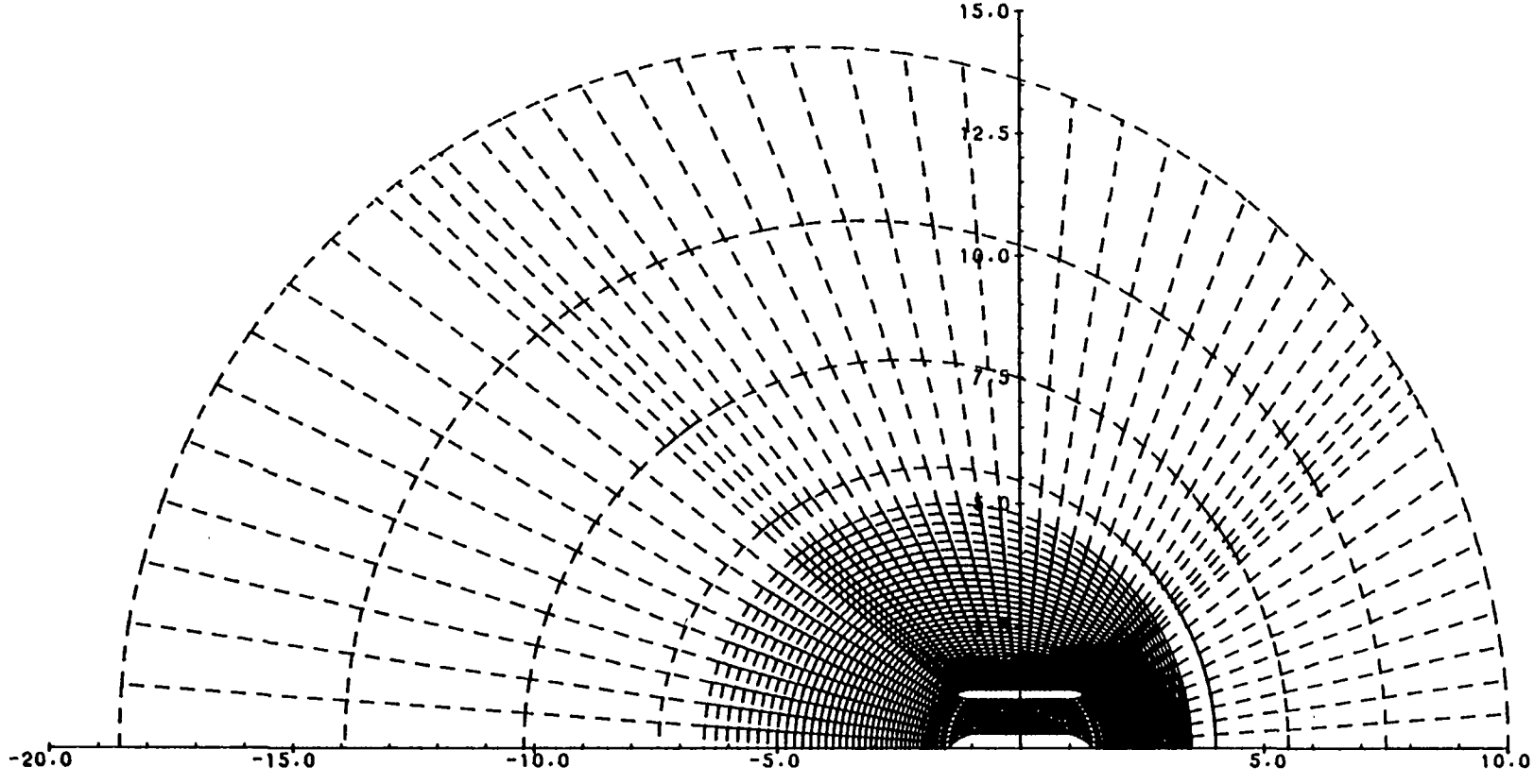

Figure 7. Mesh generated for example calculations.

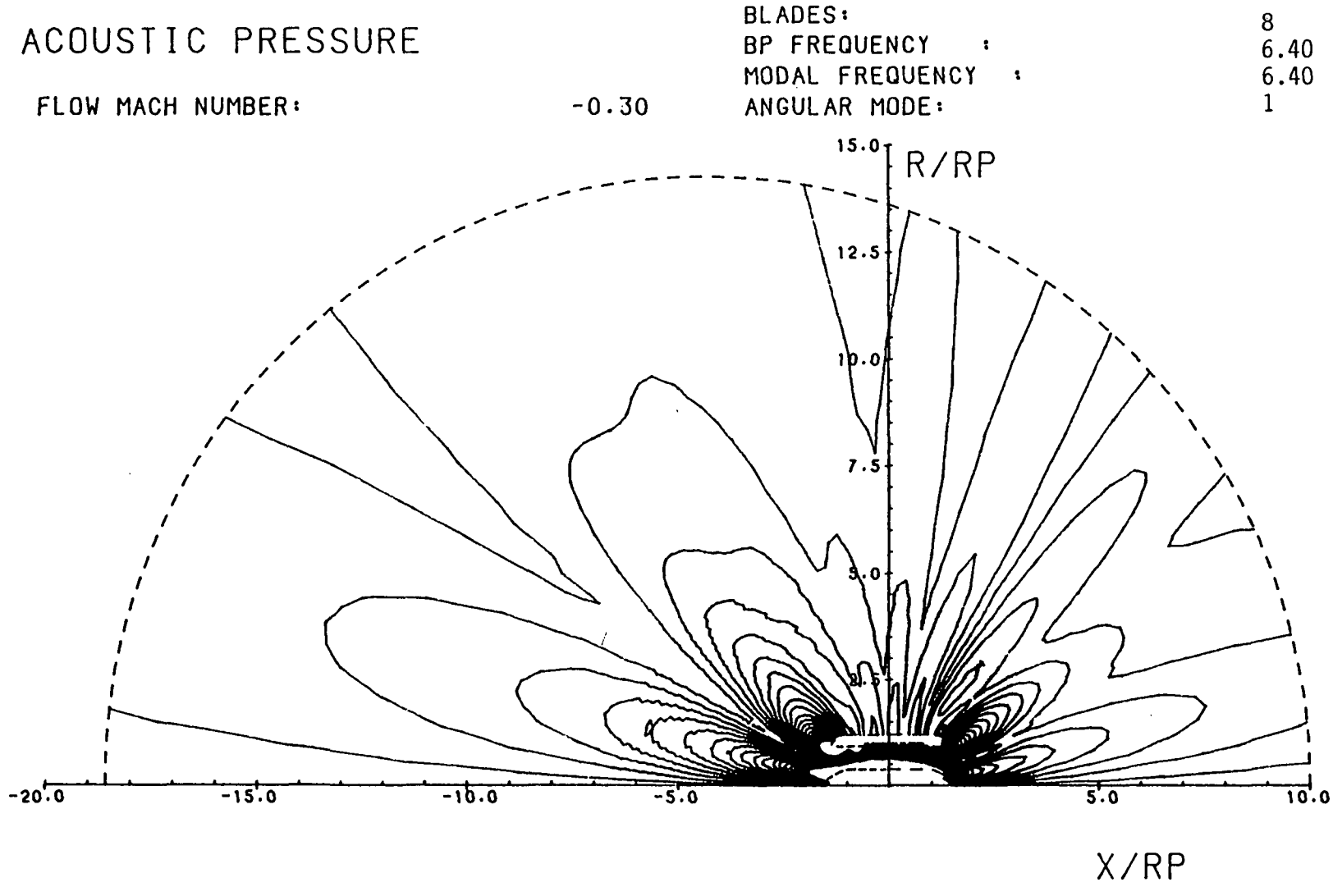

Figure 8. Contours of constant Sound Pressure Level around the nacelle in the case of EGV interaction noise with 8 blades and 7 exit guide vanes creating the angular mode m=1. The blade tip Mach number is M=0.8. The inlet and exhaust ducts are unlined.

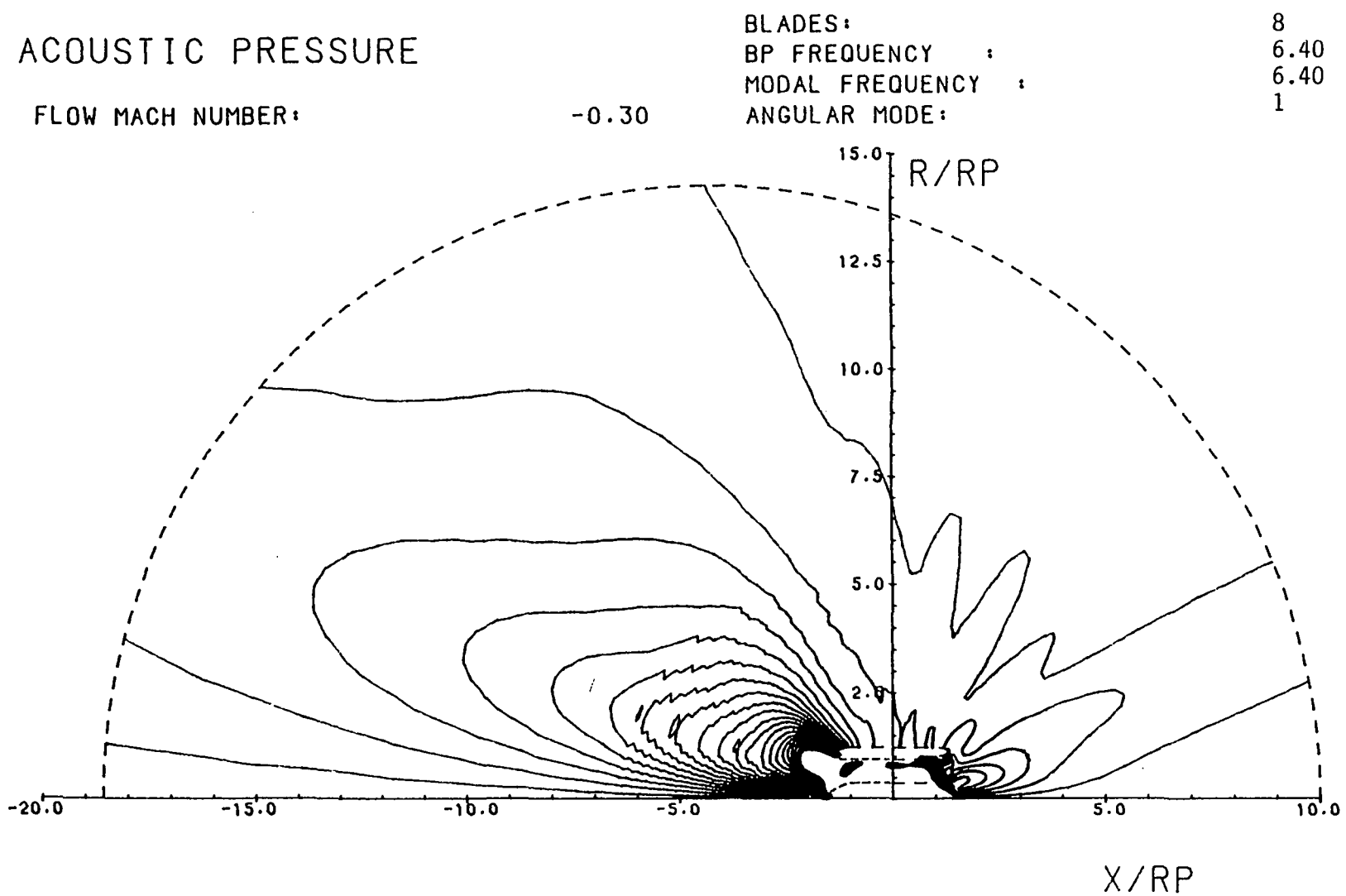

Figure 9. Contours of constant Sound Pressure Level around the nacelle in the case of EGV interaction noise with 8 blades and 7 exit guide vanes creating the angular mode m=1. The blade tip Mach number is M=0.8. The inlet and exhaust ducts are lined with a "Cremer" optimum lining.

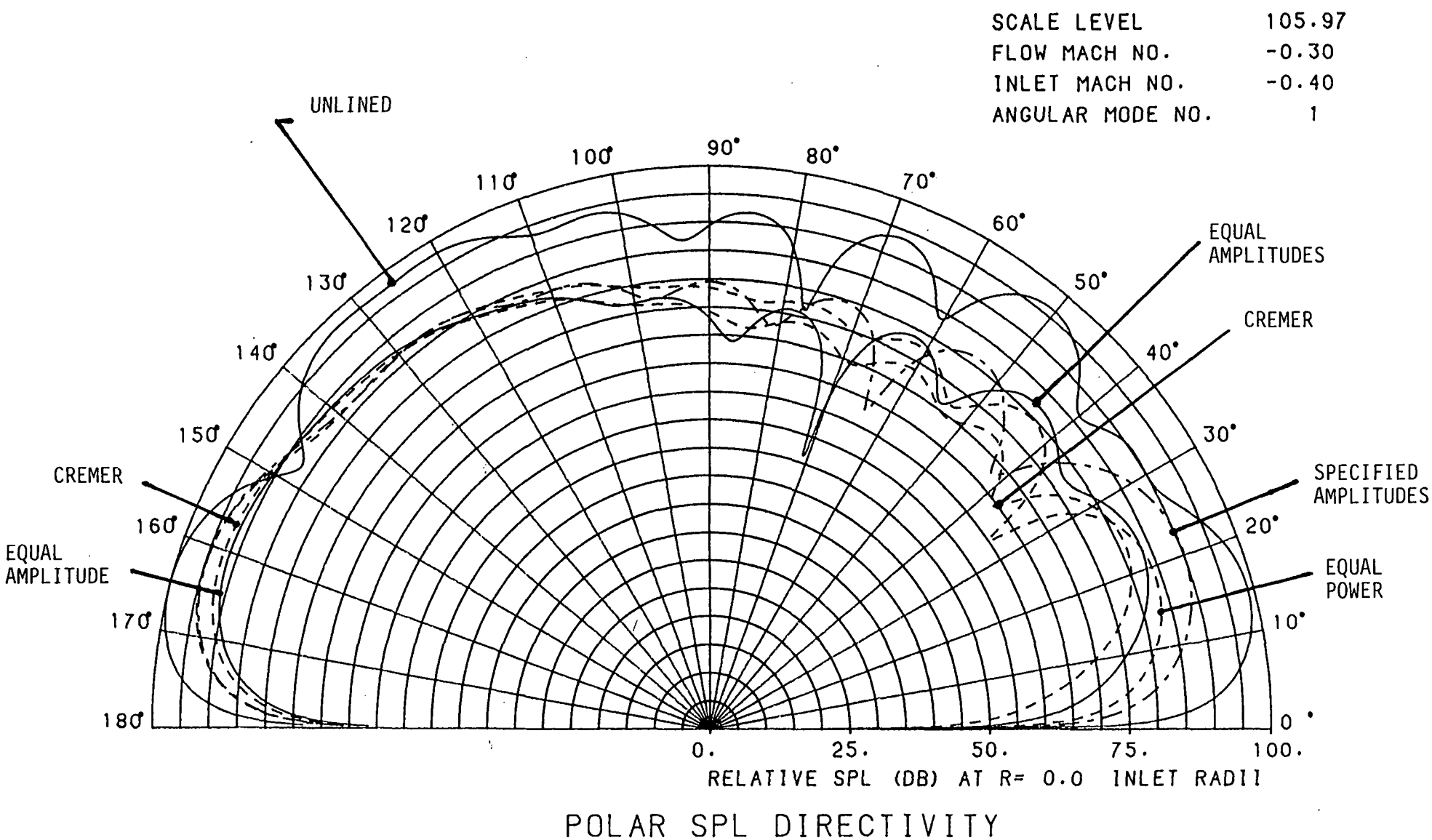

Figure 10. Polar directivity at 10 duct radii for EGV interaction noise. 8 blades and 7 exit guide vanes. Blade tip Mach number is 0.8. Amplitude normalized to 100 dB. Computed level is obtained by noting the scale level of 106 dB.

APPENDIX A

"Radiated Noise of Ducted Fans"
DGLR/AIAA 92-02-139
May, 1992

RADIATED NOISE OF DUCTED FANS

Walter Eversman
Mechanical and Aerospace Engineering
and Engineering Mechanics
University of Missouri-Rolla
Rolla, Missouri 65401

ABSTRACT

A finite element model is created for the generation, propagation, and radiation of steady, rotor alone noise and rotor and exit guide vane interaction noise of a ducted fan. In the case of rotor alone noise the acoustic source is represented by a rotating lifting line of thrust and torque dipoles distributed radially on the blade. For a specified number of blades, angular mode harmonic, and rotor angular velocity, the acoustic field is described in a cylindrical coordinate system reduced to only the axial and radial directions. The blade loading is imposed on a radial line at the axial location of the fan. The blade loading is assumed to vary linearly from the hub to the tip. The blade tip loading is determined by a specified thrust requirement and the inflow velocity. In the case of interaction noise the acoustic source is a stationary lifting line of torque and thrust dipoles which represents the fluctuating lift on the exit guide vane created by the velocity deficit associated with wakes in the steady velocity field behind the rotor. The fan and exit guide vanes are imbedded in a duct which can be contoured to represent a realistic installation. In the configurations considered in the present study, emphasis is on ducted fans or ducted propellers for which the by-pass ratio is very large. In this case the usual assumption is made that the fan, or propeller, is operating in a mean flow environment which is uniform and the same as the forward flight velocity. The flow acceleration in the inlet, acceleration in the fan duct, and jet free shear layer are not accounted for in the present model. The model accounts for the noise generation process, the propagation through the inlet and fan duct, and the radiation to the near and far field. The major issue addressed in the computational examples is the relationship between the far field radiated Sound Pressure Level (SPL) and directivity and fan tip speed.

INTRODUCTION

Ultra high by-pass ratio turbo-fan engines and ducted or shrouded propellers are attractive from the standpoint of propulsive efficiency. In addition there are possible advantages to be gained in radiated noise levels due to the imbedding of the propeller or fan acoustic source within the nacelle or shroud. An unducted propeller generates an acoustic field which tends to produce high levels on the sideline, and therefore may create unaccceptable noise levels in the interior of the aircraft. A ducted propeller is restricted in the way in which it can radiate to the near and far field. It is known that steady, rotor alone noise, created by blade loading, is a principle source mechanism for unducted propellers. It is generally assumed that in the case of a ducted propeller the rotor alone noise is not propagated to the far field if the tip speed does not exceed the speed of sound. This result, due to pioneering work of Tyler and Sofrin [1], is true for rotor generated noise in a thin annulus with the absence of duct mean flow.

In the case of ducted fans and propellers an additional source mechanism exists associated with the presence of exit guide vanes. The EGV operate in a helical velocity field behind the rotor, which is for the most part steady and defined in direction by the thrust of the rotor. The mainly steady character of the rotor generated velocity is periodically interrupted by the viscous wakes downstream of the individual rotating blades. The EGV produce lift in response to the rotor velocity field, and because of the fluctuating velocity field behind the rotor, produce fluctuating lift and provide an acoustic source mechanism. This interaction source mechanism was also addressed by Tyler and Sofrin [1] and was shown to have the potential for the creation of acoustic modes of very low angular order. Modes of this type will propagate and radiate with a directivity pattern which may produce high levels near the axis of symmetry.

The purpose of the work presented here is to investigate the differences in the radiated acoustic fields of ducted and unducted propellers of the same thrust operating under similar conditions. Hanson [2] has created a comprehensive acoustic model for unducted propellers which accounts for spanwise and chordwise details of the blade loading. It is not the intent in the present study to focus on such a refined model. Instead, the approach is to generate a very simple source model, similar to the classic lifting line theory suggested by Gutin [3], to concentrate on the propagation and radiation effects introduced by the duct, and to compare the acoustic performance of similar ducted and unducted propellers based on the same source model.

The finite element method (FEM) has been used in previous studies to model the wind tunnel acoustic testing of propellers and the free field acoustic radiation of propellers [4-7]. In the present study the FEM is used to model the ducted propeller in the free field. This combines the propeller modeling previously reported and some aspects of earlier work on the prediction of the radiated acoustic field from turbofan engine inlets [8-9].

The generation, propagation, and radiation of sound from a ducted fan is described in this study by the convected wave equation with volumetric body forces. Body forces are used to introduce the blade loading for rotating blades and stationary exit guide vanes (EGV). For an axisymmetric nacelle or shroud, the problem is formulated in cylindrical coordinates. For a specified angular harmonic the angular coordinate is eliminated and a two dimensional representation results. A finite element discretization based

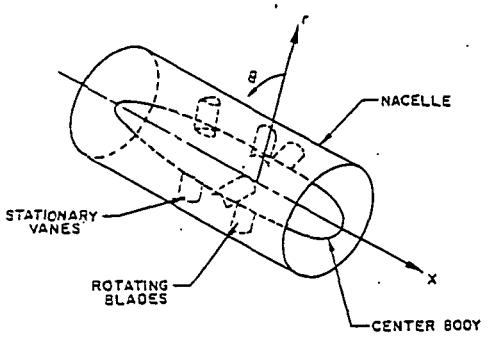

Figure 1.

Geometry of Shrouded Propeller or Rotor.

on nine node quadratic isoparametric elements is used. The nacelle and center body or core engine are defined as rigid surfaces. The assumption is made that the bypass ratio is large enough so that the entire flow field is uniform, consistent with the usual model in propeller acoustic analyses. Features not modeled are the nonuniform flow in the inlet and fan duct, and the free shear layer in the fan duct exhaust jet.

Geometry and Coordinate System

In this investigation the acoustic field is conveniently represented in a cylindrical geometry with the axis of the propeller or rotor/nacelle designated as the x axis. It is assumed that the nacelle/centerbody combination is axially symmetric and that the inlet flow field is axially symmetric. Specifically excluded by this restriction are drooped inlets and nacelles for which the inlet duct is not circular. The acoustic field is not required to be axially symmetric, and it would be unlikely that it is. The acoustic field is periodic in the angular coordinate of the cylindrical system. It is represented as the components of a Fourier Series in the angular coordinate θ. The acoustic field for each angular component, or "angular mode," is represented by a field equation in only the axial and radial components x, r of the cylindrical system.

Figure 1 shows an idealized geometry for a rotor/nacelle arrangement. Noise sources related to the rotating blades and the interaction of the blades with stationary exit guide varies can be modeled.

The steady velocity field in and around the nacelle is assumed to be uniform. For many applications, notably the case of the ultra high bypass fan or the ducted propeller this is probably satisfactory. For other cases it may be necessary to model the flow in and around the nacelle. It may also be required to consider the effects of the shear layer in the interface between the fan exhaust and the surrounding steady flow.

Mathematical Model

The acoustic field is described by the convected wave equation with body forces

$$\nabla^2 p^* - \frac{1}{c^2}\frac{D^2 p^*}{Dt^{*2}} = \rho_o \nabla \cdot \bar{f}^* \qquad (1)$$

where p^* is the acoustic pressure, ρ_o is the ambient density, c is the ambient speed of sound, and $\bar{f}^*$ represents the body force per unit mass acting on the fluid. $\rho_o \bar{f}^*$ is the body force per unit volume. Equation (1) is in dimensional form. In the development which follows a nondimensional form of equation (1) is used with the following scaling

$$x = \frac{x^*}{L}, \quad p = \frac{p^*}{\rho_o c_o^2}, \quad t = \frac{ct^*}{L}, \quad \bar{f} = \frac{L}{c_o^2}\bar{f}^*$$

t^* is the dimensional time and x^* is any of the linear spatial coordinates. The reference length L is the propeller radius R. The nondimensional form of the acoustic field equation is

$$\nabla \cdot \left(\nabla p - M^2 \frac{\partial p}{\partial x}\bar{i} - \bar{f}\right) - 2M \frac{\partial^2 p}{\partial x \partial t} - \frac{\partial^2 p}{\partial t^2} = 0 \qquad (2)$$

The body force per unit mass $\bar{f}$ is related to the force exerted on the fluid by the rotating blade or stationary vane.

The major deficiency in this model is the assumption that the interior flow and external flow are uniform and at the flight Mach number. This is required because a pressure formulation has been chosen to introduce the acoustic source model for the rotor or EGV via equivalent body forces acting on the fluid. This is consistent with previous models of propellers [4-7]. In the pressure formulation it is required that the flow field be uniform in order that the acoustic field equations can be reduced to the convected wave equation.

By modeling the acoustic field using the pressure formulation some liberties have been taken. Even though for ducted propellers or high by-pass ratio ducted fan types of flow fields the internal and external flows over most of the region may be approximated as being uniform and tangent to the nacelle, a region will exist near the inlet lip where the flow is clearly not uniform. The formulation of the problem using the convected wave equation does not account for this. Although the primary convective effect of the mean flow is modeled, effects due to localized flow gradients will not be included.

In addition to the requirement that the flow be uniform there is a more subtle restriction that is introduced by the natural boundary condition for the convected wave equation that would require

$$\left(\nabla p - M^2 \frac{\partial p}{\partial x}\bar{i}\right) \cdot \bar{n} = 0 \qquad (3)$$

if no forced boundary condition exists. $\bar{n}$ is the outward normal on the nacelle surface. On the nacelle surface the rigid wall boundary condition requires that

$$\nabla p \cdot \bar{n} = 0$$

which is equivalent to specifying that the acoustic particle velocity normal to the surface vanishes. Equation (3) does not reduce to this condition except where $\bar{i} \cdot \bar{n} = 0$. This is clearly violated where the surface normal is not perpendicular to the duct axis, and particularly near the inlet lip. The natural boundary condition (3) is used here with the argument that its apparent failure where $\bar{i} \cdot \bar{n} \neq 0$ is an artifact of the assumption of uniform flow. No

apparent effect of this approximation can be seen in the computational results.

A second modeling option has been used in previous studies of acoustic radiation from turbofan inlets [8,9]. The assumption is made that the mean flow and acoustic field are irrotational. The acoustic source is introduced through the specification of acoustic modal amplitudes at the fan face. This is accomplished by including suitable boundary terms. It is therefore not required to include the body forces in the momentum equation. This allows a first integral of the linearized momentum equation to be obtained, which can be interpreted as an acoustic Bernoulli equation. The combination of the continuity equation and the acoustic Bernoulli equation written in terms of the acoustic velocity potential provides the basis of the mathematical model in [8,9].

The velocity potential formulation does not seem to be appropriate if the source model is to be introduced through equivalent body forces. The critical feature which is lost is the first integral of the momentum equation leading to the acoustic Bernoulli equation. This integral is not possible unless the body force is derivable from a potential. This does not appear to be the case for the types of body forces required to represent a propeller, rotor, or EGV.

The finite element formulation of the convected wave equation (2), is the same as described in previous work related to propeller acoustic radiation [4-7]. Nine node quadratic isoparametric elements are used with special attention given to the elements spanning the propeller and containing the source terms. A frontal solver is used and models with as many as 18000 degrees of freedom have been handled routinely.

The models used for the propeller or rotor and exit guide vane acoustic sources are discussed in the following sections.

Blade Loading

The blade loading of the propeller or rotor will be considered as the only source of rotor alone noise. No effects of blade thickness will be modeled in this investigation. Blade loading will be based on isolated lifting surface theory using a strip analysis. The discussion of Dommasch, Sherby and Connolly [10] is directly relevant to the following development.

Figure 2 shows an airfoil section at the radius r from the hub. The local angle of attack of the section at radius r depends on the inflow velocity, U, the relative velocity due to rotation $r\Omega/U$, where Ω is the angular velocity of the rotor or propeller, and the blade twist ϕ. The velocity seen by the section is

$$V = U\sqrt{1+\left(\frac{1}{j}\right)^2}, \quad j(r) = \frac{U}{r\Omega} \tag{4}$$

The angle β defining the direction of the velocity seen by the section and the angle of attack α are given by

$$\cos\beta = \frac{\frac{1}{j}}{\sqrt{1+\left(\frac{1}{j}\right)^2}}, \quad \sin\beta = \frac{1}{\sqrt{1+\left(\frac{1}{j}\right)^2}}, \quad \alpha = \phi - \beta \tag{5}$$

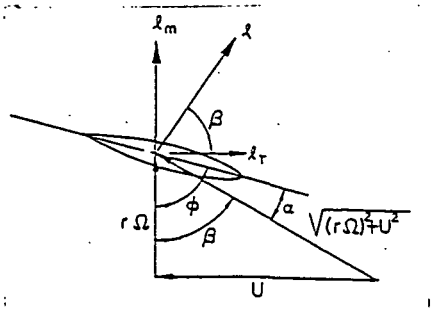

Figure 2. Velocities and Inflow Angles Experienced by a Blade Element.

The lift per unit span at the tip is

$$l_{dp} = \frac{1}{2}\rho U^2\left[1+\left(\frac{1}{J}\right)^2\right] c_{dp} c_{l_\alpha} \alpha_{dp}, \quad J = \frac{U}{R\Omega} \tag{6}$$

c(r) is the local blade chord and c_{l_α} is the section lift coefficient taken as constant in the present study. The lift per unit span as a function of radius is

$$l(r) = l_{dp}\frac{\left[1+\left(\frac{1}{j}\right)^2\right]}{\left[1+\left(\frac{1}{J}\right)^2\right]}\bar{c}(r)\,\bar{\alpha}(r) \tag{7}$$

For the present investigation it is assumed that the blade loading is linearly distributed from root to tip, that is

$$l(r) = l_{dp}\left(\frac{r}{R}\right) \tag{8}$$

The thrust on N_B blades is given by

$$T = N_B\int_{R_1}^{R} l(r)\cos\beta\,dr = N_B\, l_{dp}\int_{R_1}^{R}\left(\frac{r}{R}\right)\frac{\left(\frac{1}{j}\right)}{\sqrt{1+\left(\frac{1}{j}\right)^2}}\,dr \tag{9}$$

or

$$T = N_B l_{dp} R J^2 D(J) \tag{10}$$

where

$$D(J) = \left[\frac{\left(\frac{1}{j}\right)}{2}\sqrt{1+\left(\frac{1}{j}\right)^2} - \frac{1}{2}\ln\left(\frac{1}{j}+\sqrt{1+\left(\frac{1}{j}\right)^2}\right)\right]_{R_1}^{R} \tag{11}$$

R_1 is the inner radius of the propeller or rotor. The required tip loading for a given thrust can now be determined from equation (10)

$$l_{dp} = \frac{T}{N_B R J^2 D(J)} \tag{12}$$

The thrust and torque loading are

$$l_t = l_{dp} \cos\beta \left(\frac{r}{R}\right), \qquad l_n = l_{dp} \sin\beta \left(\frac{r}{R}\right) \tag{13}$$

Other types of loading can be considered by reformulating equation (8) and the subsequent analysis. Since the investigation reported here centers primarily on comparisons of unshrouded and shrouded propellers, it is not deemed critical to precisely specify the loading.

The lift distribution discussed here is dimensional, and thus based on full scale parameters.

Rotor Alone Noise

Rotor alone noise generation is viewed from the perspective of a volumetric force fixed in space which is active during the passage of a blade with its associated lift distribution. It is assumed that the duration of passage of the blade past a fixed point is $\tau = \frac{a}{\Omega r}$ where a(r) is the projection of the blade chord on the rotor plane. The strength of the volumetric force representing the blade passage is taken as the negative of the lifting pressure differential across the blade, approximated by l(r)/c(r) where c(r) is the local chord.

The strength is

$$\rho_o \bar{f} = - \frac{l(r)}{c(r)} \delta(y^*) \bar{e}_n \tag{14}$$

where y^* is a dimensional coordinate normal to the blade. The lift per unit span here is taken to act normal to the blade chord, which is oriented by the twist angle ϕ. The unit vector $\bar{e}_n$ is taken normal to the blade. The relationship between x^*, the dimensional axial coordinate, and y^*, the normal to the blade chord, for θ = constant, is

$$y^* = x^* \cos\phi$$

By making use of the property of the Dirac delta function that $\delta(ax) = a^{-1}\delta(x)$, equation (14) can be written

$$\rho_o \bar{f}^2 = \frac{l(r)}{c(r)\cos\phi} \delta(x^*) \bar{e}_n \tag{15}$$

$c(r)\cos\phi$ is the projection of the blade chord on the rotor plane so that

$$\rho_o \bar{f} = - \frac{l(r)}{a} \delta(x^*) \bar{e}_n \tag{16}$$

At a fixed angular position $\theta = 0$, for the successive passage of N_B blades

$$\begin{aligned} \rho_o \bar{f} &= - \frac{l(r)}{a} \delta(x^*) \bar{e}_n \qquad 0 \le t \le \tau \\ &= 0 \qquad\qquad\qquad\quad \tau \le t \le \frac{2\pi}{N_B\Omega} \end{aligned} \tag{17}$$

The body force per unit volume is periodic with period

$$T = \frac{2\pi}{N_B\Omega}$$

and can be expressed in the Fourier Series

$$\rho_o \bar{f} = - \frac{l(r)}{a} \delta(x^*) \sum_{m=-\infty}^{\infty} C_m e^{imN_B\eta t} \tag{18}$$

where $\eta = \frac{\Omega R}{c}$ and

$$C_m = \frac{\sin mN_B\Omega\tau + i(\cos mN_B\Omega\tau - 1)}{2\pi m} \tag{19}$$

The body force per unit volume can be resolved into thrust and torque components on the basis of the angle which orients the velocity seen by the blade. The components are

$$\rho_o f_t = - \frac{l(r)}{a} \cos\beta \, \delta(x^*) \sum_{m=-\infty}^{\infty} C_m e^{imN_B\eta t} \tag{20}$$

$$\rho_o f_m = \frac{l(r)}{a} \sin\beta \, \delta(x^*) \sum_{m=-\infty}^{\infty} C_m e^{imN_B\eta t} \tag{21}$$

Note that these body forces are on the fluid and are therefore opposite to the corresponding forces on the blade. The thrust component is rearward and the torque component is in the direction of blade rotation.

The development to this point is for the reference location $\theta = 0$. At any other location the same temporal event occurs with the phase lag $\Delta t = \theta/\Omega$. Hence at any angle, in non-dimensional form

$$f_t = - \frac{1}{\rho c_o^2} \left(\frac{l(r)}{a}\right) \cos\beta \, \delta(x) \sum_{m=-\infty}^{\infty} C_m e^{imN_B\eta t} e^{-imN_B\theta} \tag{22}$$

$$f_m = \frac{1}{\rho c_o^2} \left(\frac{l(r)}{a}\right) \sin\beta \, \delta(x) \sum_{m=-\infty}^{\infty} C_m e^{imN_B\eta t} e^{-imN_B\theta} \tag{23}$$

The body force per unit volume has frequencies which are integer multiples of the blade passgage frequency $N_B\Omega$. The nondimensional form is obtained by noting that the nondimensional body force per unit volume is obtained from the dimensional form by dividing by c_o^2/R. Furthermore, the dimensional Dirac delta function with the dimensional argument is nondimensionalized by division by R.

EGV Interaction Noise

In order to estimate the noise generating mechanism of the exit guide vanes (EGV) in their interaction with the rotating blades, a simplified model has been constructed. This model assumes that the EGV are on the average under the influence of a steady lift dictated by the magnitude and direction of the absolute velocity field leaving the rotor. This can be approximated from a knowledge of the steady blade loading in the rotor stage. The flow field downstream of the rotor is not steady, but is interrupted by the wakes downstream of the blade trailing edges. The velocity deficit in the wake, which is dependent on the distance downstream of the blade trailing edge, creates a fluctuating lift on the EGV. It is this fluctuation which becomes the noise source.

r =RADIUS OF BLADE SECTION
Ω =ROTOR ANGULAR VELOCITY

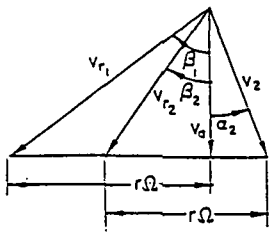

Figure 3. Velocity Triangles for Flow Behind the Rotor.

The model used here is based on quasi-steady strip theory aerodynamics and is intended only as an estimate of the actual source mechanism.

From the elementary theory of axial flow turbomachines [11] the absolute inlet velocity, v_a, the velocity relative to the rotor at the inlet, v_{r_1}, the velocity relative to the rotor at the exit, v_{r_2}, and the absolute velocity at the exit v_2 can be determined from the velocity triangle of Figure 3. The pressure rise across the rotor is given by

$$\Delta p = \frac{\rho}{2} U^2 (\tan^2\beta_1 - \tan^2\beta_2) \tag{24}$$

The pressure rise is balanced by the thrust component of force per unit span

$$N_B l_T(r) = 2\pi r \Delta p \tag{25}$$

Therefore, for a known thrust loading

$$l_T(r) = \frac{\rho}{2} U^2 \left(\frac{2\pi r}{N_B}\right) (\tan^2\beta_1 - \tan^2\beta_2) \tag{26}$$

For a local blade section β_1 and β_2 are defined by

$$\tan\beta_1 = \frac{\Omega r}{U}, \quad \tan\beta_2 = \sqrt{\left(\frac{\Omega r}{U}\right)^2 - \frac{N_B l_T(r)}{2\pi r q_A}} \tag{27}$$

where $q_A = 1/2\ \rho U^2$ is the approach dynamic pressure. From the velocity triangle

$$\alpha_2 = \tan^{-1}\left(\frac{\Omega r}{U} - \tan\beta_2\right), \quad v_2 = U\sqrt{1 + \tan^2\alpha_2} \tag{28}$$

The steady lift per unit span on an EGV is estimated to be

$$l_s = \frac{1}{2} \rho v_2^2 c_e c_{l_\alpha} \alpha_2 \tag{29}$$

with the assumption that the EGV has no twist. c_e is the chord of the EGV and the lift curve slope is c_{l_α}. The steady lift per unit span on the EGV can be estimated from equation (29) at the same time that the rotor blade loading is calculated.

The load fluctuations on a reference EGV are stipulated to occur due to the velocity deficit in the wakes behind the reference rotor blade. The unsteady lift per unit span is

$$\begin{aligned} l_u(t) &= \epsilon l_s \qquad 0 \le t \le \tau \\ &= l_s \qquad \tau \le t \le T \\ & \qquad 0 \le \epsilon \le 1 \end{aligned} \tag{30}$$

where

$$T = \frac{2\pi}{\Omega} \tag{31}$$

is the period of passage of the reference blade in front of the reference EGV. The duration of the reduced velocity is established by the wake thickness h according to

$$\tau = \frac{hT}{2\pi r} \tag{32}$$

With this picture of the fluctuating lift, the Fourier Series for this periodic event is

$$l_u(t) = l_s - (1 - \epsilon) l_s \sum_{n=-\infty}^{\infty} F_n e^{in\Omega t} \tag{33}$$

where

$$F_n = \frac{\sin n\Omega\tau + i(\cos n\Omega\tau - 1)}{2\pi n} \tag{34}$$

The fraction of the steady lift experienced by the EGV during the encounter with the blade wake is assumed to depend on the distance between the rotating blade and the EGV. The measure of this separation is the distance x_d in blade chords of the EGV leading edge behind the rotating blade leading edge. The velocity downstream in the wake is given by

$$v_w = \left(1 - \frac{1}{x_d}\right) v_2 \tag{35}$$

The parameter ϵ is therefore

$$\epsilon = \left(1 - \frac{1}{x_d}\right)^2 \tag{36}$$

In equation (29), the steady lift is associated with the steady flow. In the acoustic formulation the fluctuating load is the acoustic source, so that body force per unit volume will be related to the fluctuating lift per unit span given by

$$l(t) = -(1 - \epsilon) l_s \sum_{n=-\infty}^{\infty} F_n e^{in\Omega t} \tag{37}$$

The EGV is represented spatially by a lifting line on which acts the force per unit volume

$$\rho \bar{f} = l(r)\ \delta(x^*)\ \delta(r\theta) \tag{38}$$

The Dirac delta function is written as a periodic function with period 2π,

$$\delta(r\theta) = \frac{\delta(\theta)}{r} = \frac{1}{r} \sum_{n=-\infty}^{\infty} G_n e^{in\theta}, \quad G_n = \frac{1}{2\pi} \tag{39}$$

The body force per unit volume, the reaction to the lifting force, is

$$\rho\bar{f}_{11} = (1-\epsilon)l_s \frac{\delta(x^*)}{r} \sum_{n=-\infty}^{\infty} F_n e^{in\Omega t} \sum_{m=-\infty}^{\infty} G_n e^{im\theta} \quad (40)$$

Equation (3) represents the fluctuating body force per unit volume on the reference EGV, numbered vane 1, due to the passage of the reference blade, designated blade 1.

For other than the reference vane there are temporal and spatial phase shifts

$$(k-1)\Delta t = (k-1)\frac{2\pi}{N_v\Omega}, \qquad k = 1, N_v \quad (41)$$

$$(k-1)\Delta\theta = (k-1)\frac{2\pi}{N_v}, \qquad k = 1, N_v \quad (42)$$

Equation (41) is the phase shift in time at the vane k due to the intervane angular spacing $2\pi/N_v$ and the angular velocity of the blade Ω. Equation (42) is the spatial phase shift due to the angular spacing. Hence at vane k due to the passage of the reference blade

$$\rho\bar{f}_{k1} = (1-\epsilon)l_s \frac{\delta(x^*)}{r} \sum_{n=-\infty}^{\infty} \sum_{m=-\infty}^{\infty} F_n G_m e^{in\Omega[t-(k-1)\frac{2\pi}{N_v\Omega}]} \times e^{im[\theta-(k-1)\frac{2\pi}{N_v}]} \quad (43)$$

At vane k there is a further temporal phase shift due to the passage of blade l

$$(l-1)\Delta t = (l-1)\frac{2\pi}{N_B\Omega} \quad (44)$$

The body force per unit volume for this interaction is

$$\rho\bar{f}_{kl} = (1-\epsilon)l_s \frac{\delta(x^*)}{r} \sum_{n=-\infty}^{\infty} \sum_{m=-\infty}^{\infty} F_n G_m \times e^{in\Omega[t-(k-1)\frac{2\pi}{N_v\Omega}-(l-1)\frac{2\pi}{N_B\Omega}]} e^{im[\theta-(k-1)\frac{2\pi}{N_v}]} \quad (45)$$

The total acoustic source contribution is obtained by summing over all vanes and blades

$$\rho\bar{f} = (1-\epsilon)l_s \frac{\delta(x^*)}{r} \sum_{k=1}^{N_v} \sum_{l=1}^{N_B} \sum_{n=-\infty}^{\infty} \sum_{m=-\infty}^{\infty} F_n G_m e^{in\Omega t} e^{im\theta} \times e^{-i(k-1)[\frac{2\pi(m+n)}{N_v}} e^{-i(l-1)[\frac{2\pi n}{N_B}]} \quad (46)$$

Equation (46) can be simplified by making use of the result that

$$\sum_{k=1}^{N} e^{-i(k-1)\frac{2\pi n}{N}} = 0, \qquad n \neq n_B N$$
$$= N, \qquad n = n_B N,\ n_B = 0, \pm 1, \pm 2, \ldots$$

In equation (46) for a fixed value of m and n, consider the summation over k and ℓ. This summation will vanish unless

$$n = n_B N_B, \qquad n_B = \pm 1, \pm 2, \ldots \quad (47)$$

$$m + n = n_v N_v, \quad n_v = 0, \pm 1, \pm 2, \ldots \quad (48)$$

Equation (48) can be replaced by

$$m = n_v N_v - n_B N_B \quad (49)$$

The case $n_B = 0$ is not relevant acoustically because it contributes to the time invariant part of the body force per unit volume. With these observations the body force per unit volume can be written

$$\rho_o \bar{f} = (1-\epsilon)l_s \frac{\delta(x^*)}{r} N_v N_B \sum_{n=-\infty}^{\infty} \sum_{m=-\infty}^{\infty} F_n G_n e^{inN_B\Omega t} \times e^{-i(nN_B - mN_v)\theta} \quad (50)$$

where

$$F_n = \frac{\sin n N_B\Omega\tau + i(\cos n N_B\Omega\tau - 1)}{2\pi n N_B}, \qquad G_n = \frac{1}{2\pi}$$

Since the EGV is assumed to have zero twist the angle of attack is given by α_2. The body force per unit volume is then resolved into thrust and torque components according to the non-dimensional relations

$$f_t = \frac{(1-\epsilon)}{\rho_o c_o^2}\left(\frac{l_s(r)}{r}\right)\sin\alpha_2\ \delta(x) N_v N_B \sum_{n=-\infty}^{\infty} \sum_{m=-\infty}^{\infty} F_n G_n e^{inN_B\Omega t} \times e^{-i(nN_B - mN_v)\theta} \quad (51)$$

$$f_m = \frac{(1-\epsilon)}{\rho_o c_o^2}\left(\frac{l_s(r)}{r}\right)\cos\alpha_2\ \delta(x) N_v N_B \sum_{n=-\infty}^{\infty} \sum_{m=-\infty}^{\infty} F_n G_n \times e^{inN_B\Omega t} e^{-i(nN_B - mN_v)\theta} \quad (52)$$

FINITE ELEMENT FORMULATION

Equation (2) is the field equation which governs the radiated sound field generated by the distribution of body forces $\bar{f}$ which are defined in the case of rotor alone noise by equations (22) and (23) and in the case of EGV interaction noise by equations (51) and (52). References (4-9) give details of the finite element discretization of equation (2). Here the important features are reiterated.

A Galerkin weighted residual formulation seeks a solution for the acoustic pressure p among the class of functions C^1 with continuous first derivatives which satisfy the weighted residual statement

$$\iiint_V W_i\left[\nabla\cdot(\nabla p - M^2\frac{\partial p}{\partial x}\bar{i} - \bar{f}) - 2i\eta M\frac{\partial p}{\partial x} + \eta^2 p\right]dV - \iint_S W_i\left[(\nabla p - M^2\frac{\partial p}{\partial x}\bar{i})\cdot\bar{n} - (\nabla\bar{p} - M^2\frac{\partial\bar{p}}{\partial x}\bar{i})\cdot\bar{n}\right]dS = 0 \quad (53)$$

for piecewise continuous weighting functions W_i. Equation (53) is the combination of the volume weighted residual of the field equation and the surface area weighted residual of a combination of terms which turns out to be the natural boundary condition. The overbar on $\bar{p}$ signifies that it is to be designated on S. The weak form of equation (53) is obtained by using the divergence theorem to reduce the level of continuity required of the solution p. In this form a solution p is sought in the class of continuous functions C^*, with piecewise continuous first derivatives such that

$$\iiint_V \left[\nabla W_i \cdot \left(\nabla p - M^2 \frac{\partial p}{\partial x}\vec{i}\right) + 2i\eta M W_i - \eta^2 W_i p\right] dV = \iint_S \nabla W_i \cdot \vec{f}\, dV + \iint W_i \left(\nabla \bar{p} - M^2 \frac{\partial \bar{p}}{\partial x}\vec{i}\right) \cdot \vec{n}\, dS \tag{54}$$

for all weighting functions W_i in C^*. Use is made of the fact that $\vec{f}$, the body force, vanishes on the boundary S of the domain V. The body forces are distributed over the volume V_f. $\vec{n}$ is the unit normal vector out of the volume V.

Because of the axial symmetry of the geometry of the nacelle, equation (54) is implemented in cylindrical coordinates. Figure 4 shows the bounding surfaces of the computational domain in a θ = constant slice. The surfaces of the center body S_c and the nacelle S_N are rigid so that $\nabla p \cdot \vec{n} = 0$. On these surfaces the natural boundary condition is given by the surface integral in equation (54), which if it were to vanish on S_c and S_N would require that

$$\left(\nabla p - M^2 \frac{\partial p}{\partial x}\vec{i}\right) \cdot \vec{n} = 0 \tag{55}$$

on S_c and S_N. As noted previously, the pressure formulation used here does not allow the specification of the details of the mean flow in the neighborhood of the nacelle lip and the centerbody tip due to the restriction of a uniform axially directed flow inside and outside the nacelle. The important features that are missing are the tangency of the mean flow in the vicinity of the nacelle lip and centerbody tip and the flow gradients which exist there. The flow gradients exist over a length scale which is short compared to a wave length and can reasonably be neglected. The boundary condition of equation (55) is derived on the basis of the restriction of uniform axial flow and hence that the normal $\vec{n}$ is perpendicular to the x axis so that $\vec{i} \cdot \vec{n} = 0$. Just as the flow is not tangent to the surface of the nacelle near the nacelle lip and centerbody tip, $\vec{i} \cdot \vec{n}$ does not vanish. In the pressure formulation described here, equation (55) is taken as the natural boundary condition for all rigid surfaces with the argument that in a more exact formulation, for example, the velocity potential formulation of References [8,9], the equivalent boundary condition would be based on the tangential component of mean flow, and would therefore vanish. The validity of these assumptions can only be tested by checking the computational results and looking for anomalies in the radiated acoustic field near the nacelle lip and centerbody tip.

In the case when the propeller is unshrouded, the surface integral on S_c and S_N does not exist (in the present study the center body does not exist if the propeller is unshrouded). For the unshrouded case the uniform axial flow assumption is also not rigorously true because of flow gradients which must exist to account for the momentum increase which creates the thrust. No known propeller

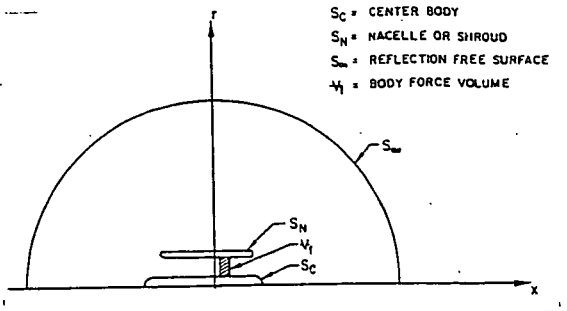

Figure 4.

Computational Domain for FEM Formulation.

acoustic model accounts for this. In this context, the formulation for the shrouded case is viewed as equivalent. With these arguments, equation (54) is taken as the weak form with the surface integral existing only on S_∞ the reflection free outer boundary. The important features of the finite element mesh used in the discretization of equation (54) are discussed in [4,8,9].

The volume integral over the distribution of body forces representing rotor alone or EGV interaction noise generation requires some special treatment because of the nature of the loading in the form of a Dirac delta function. Details are discussed in Reference [4].

The large set of algebraic equations created by the FEM discretization of equation (54) is solved by using a frontal solution routine. The resulting nodal pressures are postprocessed to create an acoustic directivity pattern, which is a contour of equal sound pressure level (SPL) on an x-r plane sliced out of the cartesian system, side line SPL, which is a plot of SPL on a line parallel to the axis and at a specified distance, and polar SPL, which is a plot of SPL at a fixed polar radius centered on the nacelle. Polar SPL results for several cases can be superposed on a summary polar SPL plot. Only polar SPL results are shown here.

COMPUTATIONAL RESULTS

In this study both rotor alone noise and EGV interaction noise for a shrouded propeller will be compared to unshrouded propeller noise for a fixed thrust. In the rotor alone case there is a distinct difference in the subsonic and supersonic tip speed cases, while in the EGV interaction no fundamental difference is attributed to the difference in rotor speed.

A. Nacelle and Propeller Configuration

A model scale propeller and nacelle is considered here. The propeller has four or eight blades and is of dimensional radius 0.311 m (1.02 ft). The blade chord is taken to be uniform at 0.052 m (0.17 ft). The non-dimensional propeller angular velocity is taken as $\eta = 0.8$ and $\eta = 0.9$ in the subsonic case and $\eta = 1.2$ in the supersonic case. For a speed of sound of 1125 ft/sec, this corresponds to angular speeds Ω = 8426 RPM and Ω = 9479 RPM for the subsonic case and Ω = 12639 RPM for the supersonic case. The nacelle geometry is shown in Figure 5. In the unshrouded propeller case no centerbody is present. This has only a slight effect on the propeller loading. The source location, whether rotor alone or EGV

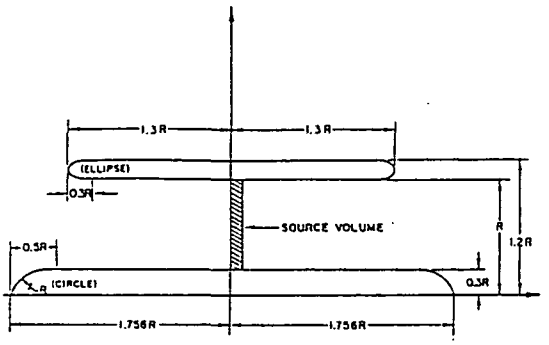

Figure 5.

Idealized Shrouded Rotor for Example Cases.

interaction, is just ahead of the center of the nacelle. The flow velocity inside and outside of the nacelle is M = 0.4.

B. Rotor Alone Noise

Figures 6 and 7 are summaries of the polar radiation directivity for four and eight blade shrouded propellers with comparisons to similar unshrouded propellers. Both supersonic and subsonic tip speeds are shown. Figure 6 is the four blade case. For supersonic tip speed, η = 1.2, the (4,1) mode (fourth angular, first radial) is cut off with cutoff ratio ξ_{41} (1.2) = 0.988 while at subsonic tip speeds it is cut off with cut off ratios ξ_{41} (0.9) = 0.74 and ξ_{41} (0.8) = 0.66. The corresponding attenuations based on the cut off ratio in the duct length of 1.3R are 10 dB, 44 dB, and 49 dB. It is seen that the peak radiated noise at a distance of ten duct radii is 120 dB created by the unshrouded propeller (this sets the scale level for the plot). The shrouded supersonic propeller has a peak level of about 109. The unshrouded subsonic propeller with η = 0.9 peaks at 114 dB and the case with η = 0.8 peaks at 112 dB. The corresponding shrouded propellers peak at 80 dB and 74 dB. The relationship of the SPL levels of the shrouded propellers below those of the unshrouded propellers is consistent with the projected attenuations due to the cutoff phenomenon, though not numerically equivalent. The comparison of the SPL levels of the two subsonic shrouded propellers with the supersonic shrouded propeller shows additional attenuations for the subsonic cases which are also consistent.

For the eight blade propeller a somewhat different picture emerges, as shown in Figure 7. For supersonic tip speed the (8,1) mode is propagating with ξ_{81} (1.2) = 1.085, but for the subsonic tip speeds it is cut off with ξ_{81} (0.9) = 0.81 and ξ_{81} (0.8) = 0.72 with calculated attenuations of 70 dB and 83 dB. Reference to Figure 7 shows that the shrouded propeller at supersonic tip speed creates the highest SPL and sets the scale level at 130 dB. The corresponding unshrouded propeller has a peak level about 10 dB lower. The unshrouded subsonic propeller at η = 0.9 peaks at about 112 dB and the corresponding shrouded case is heavily attenuated at only about 74 dB. This attenuation of 56 dB with respect to the shrouded supersonic propeller is consistent with the cutoff phenomenon. A similar result applies when η = 0.8. The unshrouded propeller peaks at 108 dB while its shrouded counterpart peaks at 39 dB (hardly visible on the figure). This attenuation of 91 dB with respect to the shrouded supersonic propeller is also consistent with the cutoff phenomenon. The interesting feature here is the high peak SPL of the shrouded propeller. The (8,1) mode for the supersonic case is cut on, as opposed to the (4,1) mode being slightly cut off for the four blade propeller. It appears that the mechanics of wave propagation in the duct enhances the radiation of the ducted propeller noise when the mode is cut on.

C. EGV Interaction Noise

To demonstrate the radiation of EGV noise a case with eight rotating blades and seven stationary vanes located one blade chord downstream is considered. The lowest angular mode excited at blade passage frequency is M_θ = 1. Figure 8 shows the radiated sound field for supersonic and subsonic rotors at η = 1.2, η = 0.9, and η = 0.8. The radiation patterns are similar with high SPL near the axis of symmetry, characteristic of the well cut on M_θ = 1 mode. There is also significant SPL away from the axis due to the presence of higher order radial modes which are propagating. An interesting feature is the relative insensitivity of the peak SPL to the rotor speed, which is in contrast to the great sensitivity observed in the rotor alone noise. It is difficult to confidently compare the peak SPL in the rotor alone and interaction cases, since both source models are approximate and are probably not entirely consistent. It is safe to note that the peak SPL in the EGV case is much higher than in the case of subsonic rotor alone noise. EGV noise clearly becomes dominant in the subsonic case.

SUMMARY

Several important observations can be made. 1) Contrary to the usual understanding of the Tyler and Sofrin result [1], supersonic tip speed rotor noise can be cut off if the tip Mach number is only slightly in excess of unity and if the number of blades is relatively small. If there are many blades, the fundamental angular mode number is large, and the Tyler and Sofrin result for thin annuli becomes more relevant. 2) Shrouding of subsonic tip speed propellers is a very effective means of controlling rotor alone noise. 3) There appears to be no benefit in terms of the peak radiated SPL for shrouded supersonic propellers when the fundamental mode is propagating. 4) For shrouded subsonic rotors, EGV noise becomes the dominant source.

ACKNOWLEDGEMENT

The investigation described here was carried out with the support of NASA Langley Research Center.

REFERENCES

1. Tyler, J. M. and Sofrin, T. G., "Axial Flow Compressor Noise Studies," Society of Automotive Engineers Transactions 70, pp. 309-332, 1962.
2. Hanson, D.B., "Near Field Frequency Domain Theory of Propeller Noise," AIAA Paper 83-0688, 1983.
3. Gutin, L., "On the Sound Field of a Rotating Propeller," NACA TM 1195, 1948 (originally in Russian 1936).

4. Eversman, W. and Steck, J. E., "Finite Element Modeling of Acoustic Singularities with Application to Propeller Noise," Journal of Aircraft, Vol. 23, No. 4, April 1986, pp.275-282.
5. Eversman, W. and Baumeister, K. J., "Modeling of Wind Tunnel Wall Effects on the Radiation Characteristics of Acoustic Sources," Journal of Aircraft, Vol. 23, No. 6, June 1986, pp. 455-463.
6. Baumeister, K. J. and Eversman, W., "Effects of Wind Tunnel Wall Absorption on Acoustic Radiation of Propellers," Journal of Propulsion and Power, Vol. 5, No. 1, January-February 1989, pp.56-63.
7. Eversman, W., "Analytical Study of Wind Tunnel Acoustic Testing of Propellers," Journal of Aircraft, Vol. 27, No. 10, October,1990, pp.851-858.
8. Eversman, W., Parrett, A. V., Preisser, J.S., and Silcox, R. J., "Contributions to the Finite Element Solution of the Fan Noise Radiation Problem," ASME Journal of Vibration, Acoustics, Stress, and Reliability in Design, Vol. 107, No. 2, February 1985, pp. 216-223.
9. Preisser, J. S., Silcox, R. H., Eversman, W. and Parrett, A. V., "A Flight Study of Tone Radiation Patterns Generated by Inlet Rods in a Small Turbofan Engine," Journal of Aircraft, Vol. 22, No. 1, January 1985, pp. 57-62.
10. Dommasch, D. O., Sherby, S. S. and Connally, T. F., Airplane Aerodynamics, Pitman, New York, 1967, pp. 219-233.
11. Vincent, E. T., The Theory and Design of Gas Turbines and Jet Engines, McGraw-Hill, New York, 1950, pp.324-335.

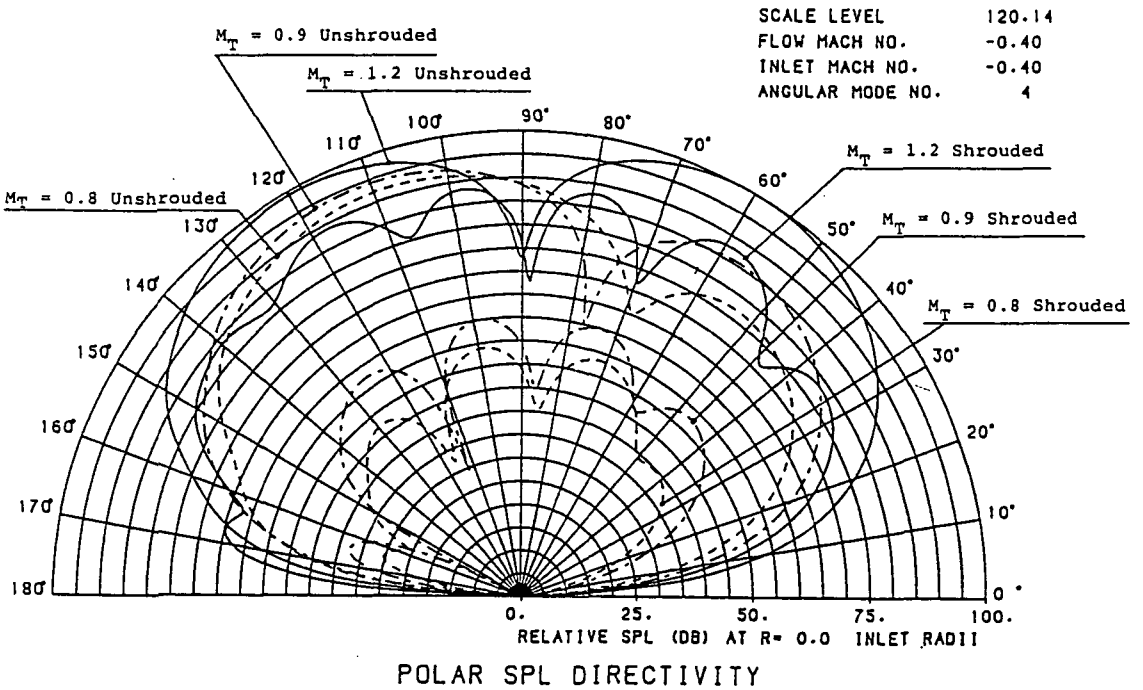

Figure 6. Radiated Acoustic Field for a Four Blade Propeller, Rotor Alone. Actual SPL is Relative SPL + 20.14 dB.

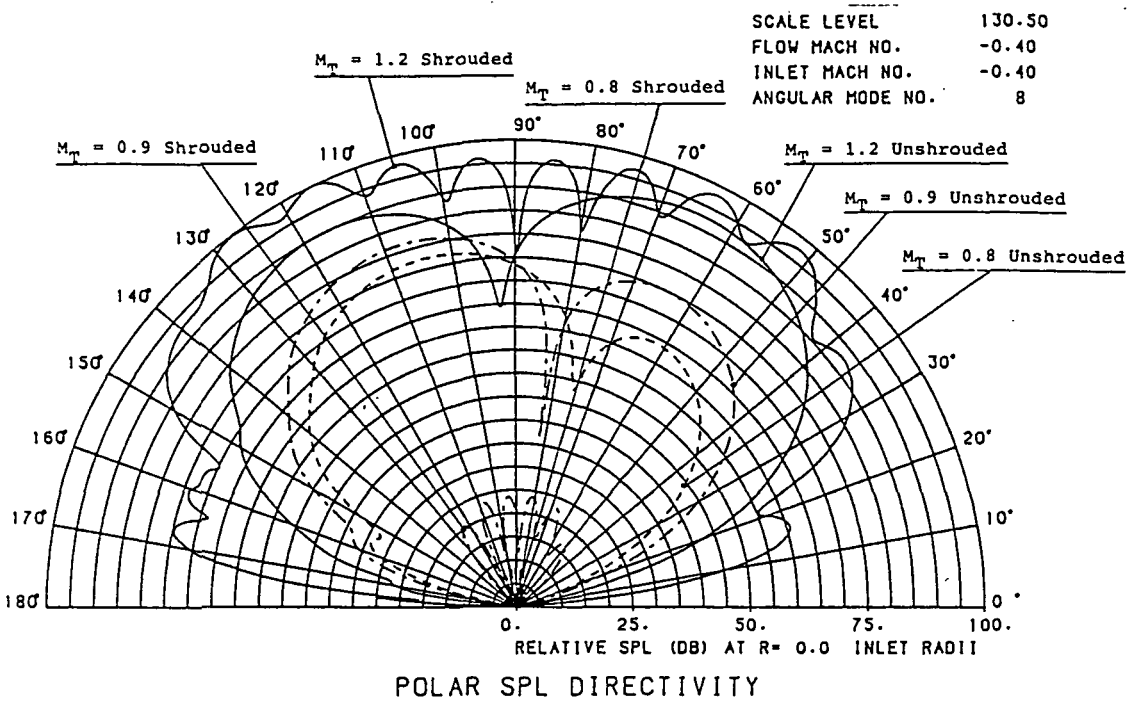

Figure 7. Radiated Acoustic Field for Eight Blade Propeller, Rotor Alone. Actual SPL is Relative SPL + 30.5 dB.

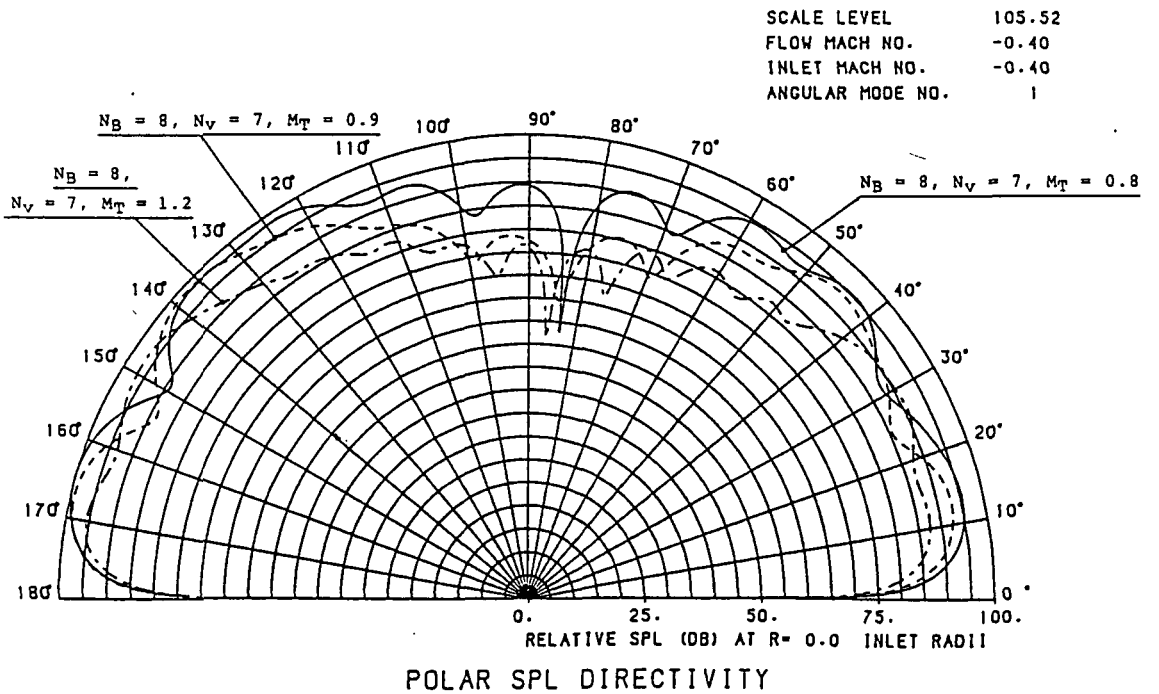

Figure 8. Radiated Acoustic Field for EGV Interaction. N_B = 8, N_V = 7, M_θ = 1. Actual SPL is Relative SPL + 5.52 dB.

APPENDIX B

MESH GENERATION

APPENDIX B. MESH GENERATION SCHEME

This section discusses the generation of the finite element mesh which plays a vital role in the formulation of the problem. Figure 1 shows an eight-node parent element with the local numbering of its nodes. For the convenience of constructing the mesh, the entire computational domain has been divided into three regions. Figure 2 illustrates the three regions clearly. Region I occupies the interior of the nacelle, both forward and aft of the propeller, region II extends from outside the inlet to the transition boundary C_1 and region III (the wave envelope region) extends from C_1 to the outer boundary C_∞.

A. REGION I

Due to the complex nature of the acoustic field inside the nacelle, a fine mesh is generated in order to resolve the variation in acoustic properties. It is separated from region II by a circle which we shall call the highlight circle. There are, in fact, two highlight circles, one fore and the other aft of the propeller. The highlight circles are drawn from the nacelle tip (also known as the highlight) in such a way that their centers lie at the point of intersection of the x-axis and a line passing through the tip of the nacelle at 45° with the x-axis (see Figure 3).

The inner surface of the nacelle C_n extends from the propeller to the tip of the nacelle, both fore and aft. The centerline of the inlet geometry extends from the intersection of the centerbody curve with the x-axis (fore and aft) and the intersection of the highlight circles with the x-axis (fore and aft respectively). Three-node quadratic line elements lie along the inner surface of the nacelle, the centerbody and the centerline. The coordinates of these nodes are given as input to generate the mesh in region I. The number of input nodes on the inner surface of the nacelle and on the centerbody and centerline is the same, to produce a mesh

of generally rectangular elements.

The vertical line segment $x = 0$ between the inner surface of the nacelle and the centerbody has also been divided into several elements not necessarily of equal width, each to be represented by a three-node quadratic line element. Figure 4 illustrates the meshing scheme in this region. The "vertical" element boundaries inside the nacelle are formed by arcs of circles. These arcs are drawn through corresponding nodal points on the upper and lower boundaries (for example, the fifth node on the nacelle inner surface and on the centerbody and centerline, counted from the line $x = 0$) with the center of the circles lying on the x-axis. Such circles are easily constructed as illustrated by Figure 5. (x_1, y_1) and (x_2, y_2) are coordinates of any two corresponding nodal points on the nacelle inner surface and the centerbody and centerline respectively. Then the x-coordinate of the center of a circle passing through these two points and having its center on the x-axis is given by

$$x_c = \frac{(x_2^2 - x_1^2 + y_2^2 - y_1^2)}{2(x_2 - x_1)} \tag{1}$$

Now, to preserve the rectangular mesh, each of these circular arcs should have the same number of three-node line elements on them and this should equal the number of three-node line elements on the line segment corresponding to $x = 0$. Therefore, each of these arcs is divided into the same number of elements with the same fractional length (fraction based on the arc length) as on the vertical r $(x = 0)$ axis. Thus, the nodal coordinates of the line elements on each of these circular arcs is determined. The vertical column of elements adjacent to the right of $x = 0$ is chosen to represent the propeller. The nodal coordinates are stored in a topology array $AD(I, J, K)$ where I is the global element number, J is the local node number and $K = 1$ assigns the x coordinate, $K = 2$ the r coordinate, respectively, to the array. Proper connectivity relating the local node to its global

numbering is also generated and stored in a connectivity array $AN(I,J)$, where I = element number, J = local node number. This array stores the global node number for each node.

The global node numbering goes from top to bottom of each of the circular arcs starting from $x = 0$ and alternating between the fore and the aft of the propeller (see Figure 6). The element numbering is down each column of elements between adjacent circular arcs sequencing from $x = 0$ and alternating between fore and aft of the propeller (see figure 6).

B. REGION II

The mesh in region II becomes polar in nature essentially because of the configuration of the domain outside the inlet duct. Region II is separated from the wave envelope region III by a constant phase circle, as described previously, whose x-intercept is given as input. The constant phase circles are expanding radially with the local speed of sound (c) and their centers are moving away along the x-axis with the speed of uniform exterior flow (U) (see Figure 7). This phenomenon is very similar to the successive circles of outward ripples created on the surface of still water when a pebble is thrown into it. The only difference is that in still water the centers of the successive layers of outward moving circular ripples coincide and here the centers of the constant phase circles move at a constant velocity.

From Figure 7, we obtain the equation of a constant phase circle (of radius R_c) displaced along the positive x-axis with velocity U (positive direction of U is indicated in Figure 7)

$$(x - Ut)^2 + r^2 = R_c^2 \tag{2}$$

where $R_c = ct$ is the radius of the circle Therefore,

$$(x - U\frac{R_c}{c})^2 + r^2 = R_c^2 \tag{3}$$

or,

$$(x - MR_c)^2 + r^2 = R_c^2 \tag{4}$$

where M is the Mach number of the uniform exterior flow. By setting $r = 0$ in equation (4) we obtain the x-intercept of the circle

$$\bar{x} = (M \pm 1)R_c \tag{5}$$

The positive sign corresponds to the x-intercept on the positive x-axis,

$$\bar{x} = (1 + M)R_c$$

while the negative x-axis corresponds to the x-intercept on the negative x-axis,

$$\bar{x} = -(1 - M)R_c$$

The circles can be expressed in polar coordinates R and θ by,

$$(Rcos\theta - MR_c)^2 + (Rsin\theta)^2 = R_c^2 \tag{6}$$

Solving for R in terms of θ yields,

$$R = R_c[\sqrt{1 - M^2 + (Mcos\theta)^2} - Mcos\theta] \tag{7}$$

Hence, the radial distance R at every angular position θ on the outer boundary of region II is known.

The outer surface of the nacelle which forms a part of the inner boundary of region II has three-node quadratic line elements along it. Since the mesh generation in region I precedes that in this region, the coordinates of the three-node line elements lying along the two highlight circle arcs are known. The nodal points

on the outer surface of the nacelle and those on the highlight circle arcs serve as input for the mesh generation in region II (see Figure 8).

In this region and also in the subsequent region III, the nodes have been generated on and along the acoustic rays from origin. Since the mesh is polar, the angular thickness of the elements increases with radial distance because the acoustic rays are radial lines diverging from the origin. To maintain proper aspect ratio of the elements in this region, the radial thickness of the elements should also increase accordingly along acoustic rays moving away from the origin. Now, corresponding to each nodal point on the outer nacelle surface and highlight circle arc, an acoustic ray is defined and its point of intersection with the outer bounding circle of region II is calculated (see Figure 8). Therefore, the radial distance along that ray in region II is known. This radial distance is then divided according to the number of elements required along the general direction of noise propagation, in geometric progression, from the inner boundary to the boundary C_1. From elementary mathematics, we know that if $r_1, r_2, \ldots, r_n$ are n members of a series in geometric progression, then the members are related to each other in the following way,

$$\left.\begin{array}{rcl} r_2 &=& cr_1 \\ r_3 &=& cr_2 \\ \vdots & \vdots & \vdots \\ r_n &=& cr_{n-1} \end{array}\right\} \tag{8}$$

where c is the *common ratio* of increment. So, the last member is related to the first member by

$$r_n = c^{n-1} r_1 \tag{9}$$

Referring to Figure 9 where an acoustic ray intersects with the two boundaries of region II, it is obvious that the first and the last members of the geometric progression series, i.e. intersection points on the inner boundary and the outer bounding circle C_1 respectively, are known. Since the number of elements n in the

radial direction of region II is an input, the common ratio of geometric progression is found out using equation (9),

$$common\ ratio = \left(\frac{\text{outer bounding circle}}{\text{inner bounding circle}}\right)^{\frac{1}{n}}$$

Once the *common ratio* is known, the successive intervals are found out by multiplication with the *common ratio* as in equations (8). Hence, the nodal points of the line elements along that acoustic ray are located. Geometric progression provides a gradual increment in the radial thicknesses of elements which is sufficient to a maintain proper aspect ratio.

The nodal coordinate values are stored in rectangular cartesian form in a topology array $AD(I, J, K)$ as mentioned before. The connectivity array $AN(I, J)$ is also created. The element numbering and the global node numbering in this region is illustrated in Figure 6.

C. REGION III

Region III which consists entirely of wave envelope elements is bounded by the transition boundary C_1, the outer boundary C_∞, and the x-axis. The wave envelope elements, as discussed before, are large elements bounded by acoustic rays and constant phase circles. The string of elements between any two successive constant phase circles is referred to as a wave envelope layer. The input for mesh generation in this region is the number of wave envelope layers and the x-intercept of the constant phase circles bounding each layer. Using equations (5) and (7), the inner and outer radii of the constant phase circles bounding each such layer is determined. The mean radius of each layer, which is just the average of the inner and outer radii, is also calculated. Since the mesh generation in region II is complete at this stage, the three-node line elements (note that a three-node line element forms a side of an eight or nine-node isoparametric element) on the

outer bounding circle C_1 of region II have been located completely and their global numbering is also known. Therefore, corresponding to each nodal point on C_1, an acoustic ray is defined (see Figure 8) and thereby its points of intersection with the inner, mean and outer radii of each wave envelope layer are calculated. The rectangular cartesian coordinate values of these intersection points on which the nodes lie are stored in the topology array $AD(I,J,K)$. The connectivity array $AN(I,J)$ is similarly calculated as in region II. The element and the global node numbering follows after region II and is similar to region II. Since the mesh in region II is quite fine and that in region III is coarse, care should be taken to make a gradual transition in the size of the elements.

After the mesh is generated, a connectivity check is performed to ensure a proper connection between local and global numbering of nodes and uniqueness of nodal coordinate values.

E. SOME COMMENTS ABOUT THE FINITE ELEMENT MESH

The acoustic radiation problem is highly mesh dependent but the mean flow problem is not very sensitive to the mesh parameters. Since both of these problems have been solved on the same finite element mesh, a mesh conforming to the acoustic parameters is desired. One of the important factors governing the mesh is the number of elements per wavelength which must always be maintained above a minimum value in the main direction of noise propagation to resolve the fine variation in acoustic properties. According to the rule of thumb the minimum ratio of the number of elements to the wavelength for quadratic elements should be 4 or 5. Here a somewhat crude estimate has been made to evaluate that ratio along the main direction of sound propagation.

Since the nondimensional input frequency η_r (it is an input to the problem)

of the sound source on C_f is known, we obtain a ratio of the effective wavelength λ_e (the wavelength of the sound radiated is altered in the presence of mean flow) to the reference duct radius R in the following way :

$$\eta_r = \frac{\omega R}{c} = \frac{2\pi R}{\lambda}$$

since

$$\lambda_e = (1 - M)\lambda$$

therefore,

$$\eta_r = \frac{2\pi R}{\lambda_e}(1 - M)$$

or,

$$\frac{\lambda_e}{R} = \frac{2\pi}{\eta_r}(1 - M) \tag{10}$$

The Mach number M is positive if directed towards the inlet. Now if the number of elements per duct radius length is N_R and Δ is the average width of an element within that length, then

$$\frac{R}{\Delta} = N_R$$

Therefore, using equation (10), the ratio of the number of elements per unit duct radius can be expressed as

$$N_R = \frac{\eta_r}{2\pi(1 - M)} N_{\lambda_e} \tag{11}$$

where $N_{\lambda_e}(= \lambda_e/\Delta)$ is the number of elements per effective wavelength. For a specified number of elements per effective wavelength (for the elements used here N_{λ_e} is the goal), equation (12) can be used to determine the number of elements per unit of nondimensional length required. This varies as the flow towards the inlet varies, and would generally be highest within the nacelle near the propeller. The number of elements in the transverse direction within the nacelle or in the angular direction in region II is not as critical and is adjusted to maintain the aspect ratio of the elements.

Since the position of the constant phase circles bordering the wave envelope layers are user input, care should be maintained to make a gradual transition from the small conventional finite elements to the relatively large wave envelope elements. For this, the user should be aware of the radial thickness of the last layer of conventional elements along C_1. Since the radial thicknesses of the elements in region II have been incremented in geometric progression, the radial thickness of the last element in region II on the x-axis is

$$\Delta r = (c^n - c^{n-1})r_o$$

where c is the common ratio of increment, n is the number of elements radially in region II and r_o is the x-intercept of C_1. This information is valuable to the user for making a smooth transition from region II to III.

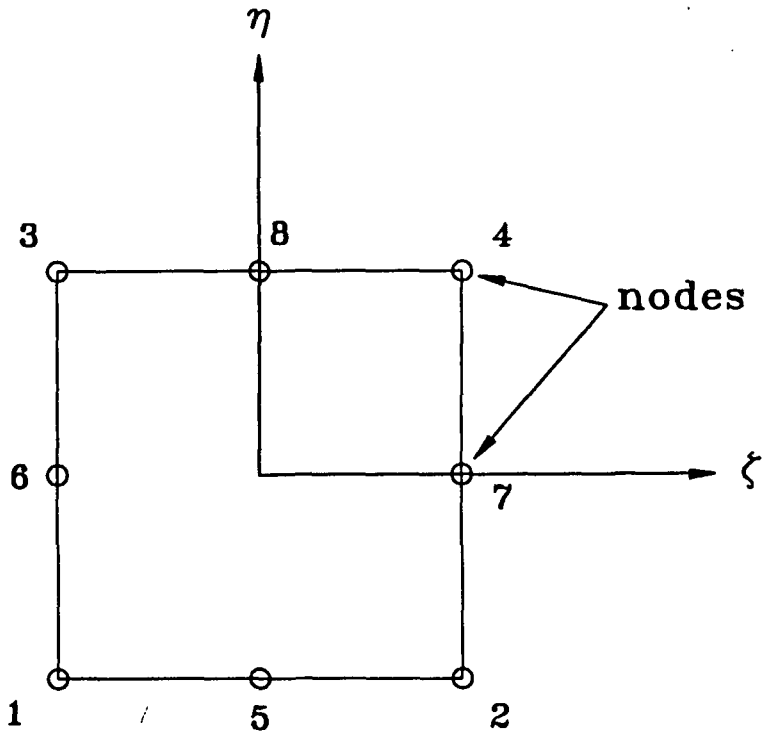

Figure 1: Parent element in local coordinates

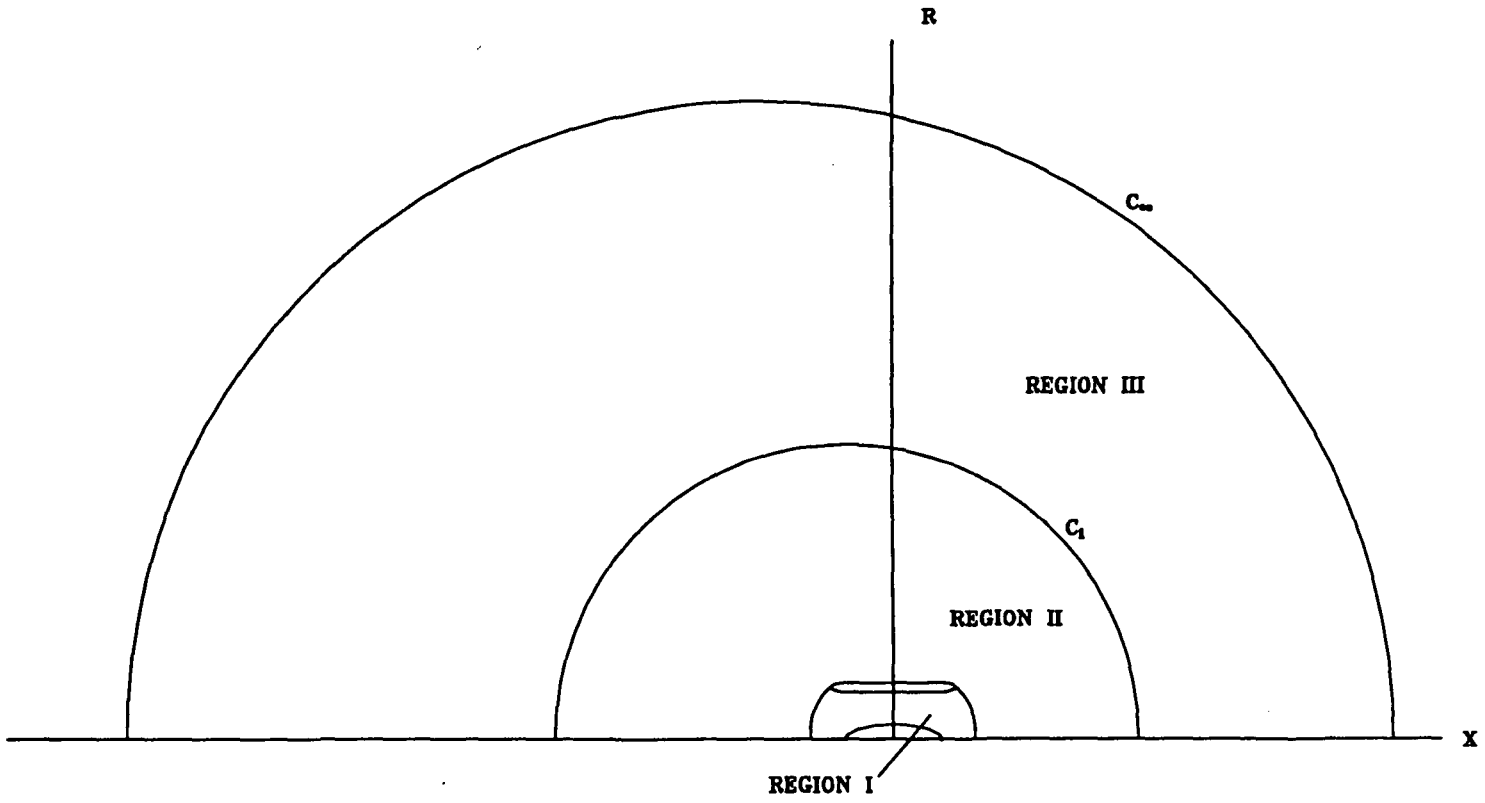

Figure 2: Mesh generation regions

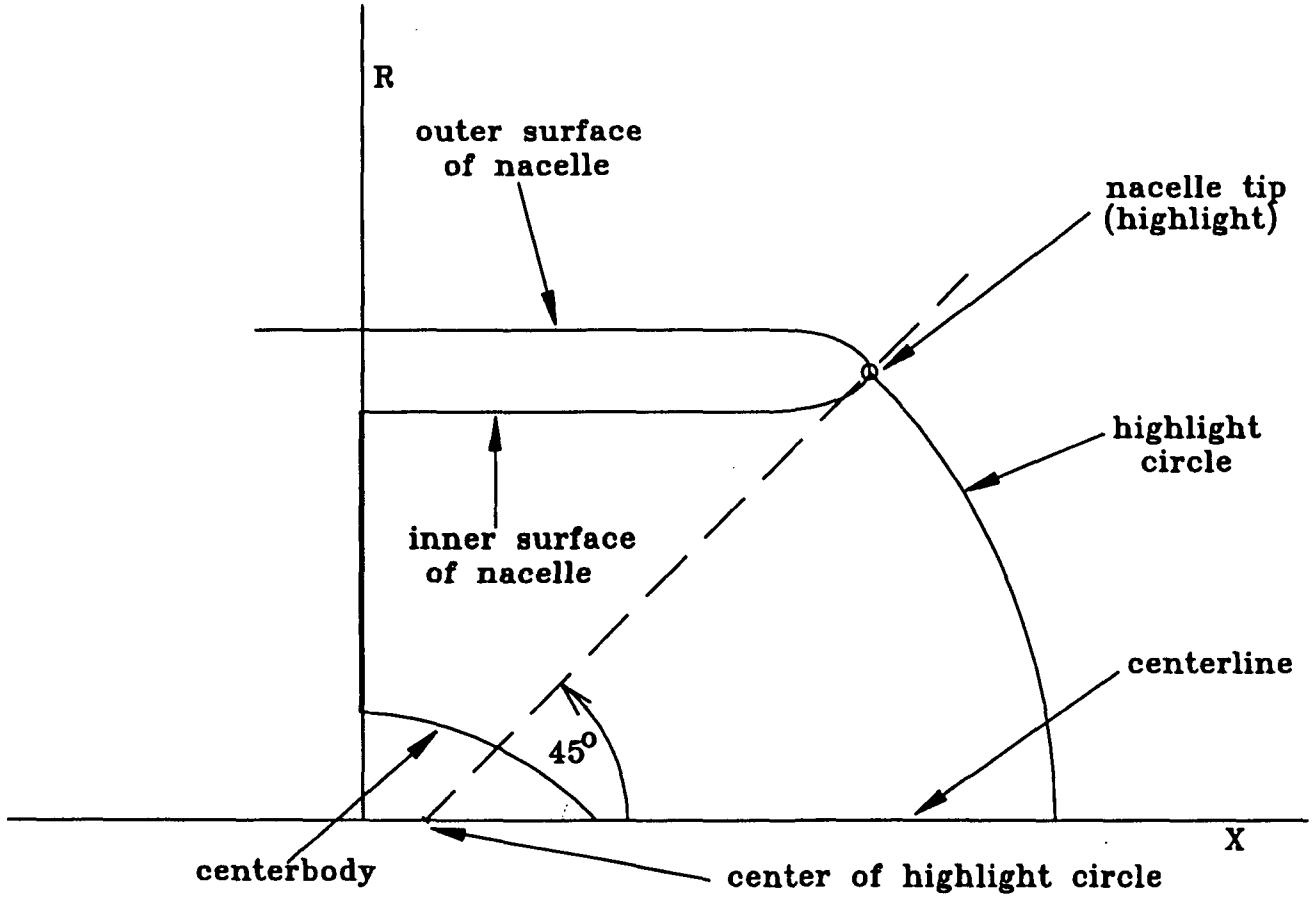

Figure 3: Geometry of region I

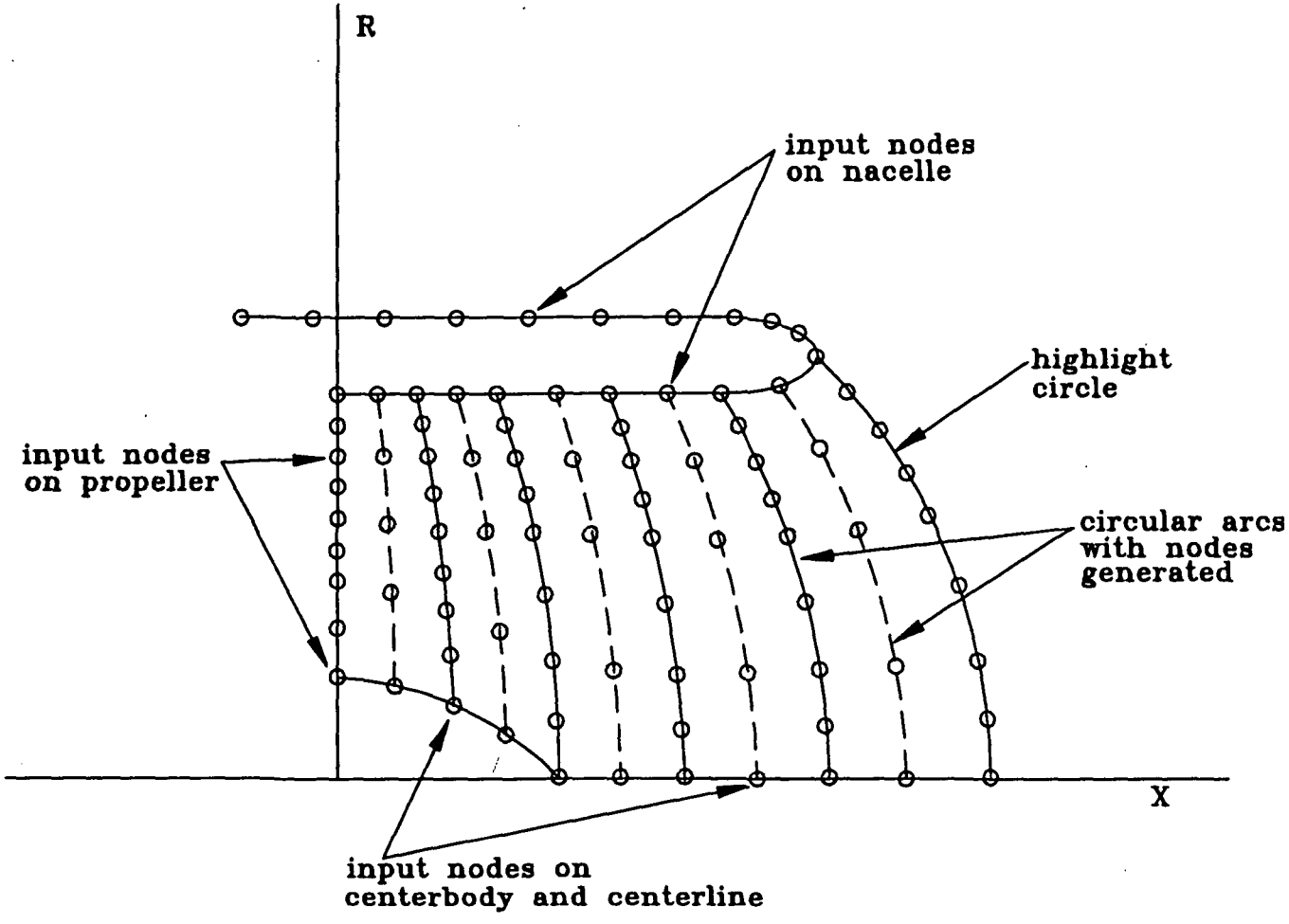

Figure 4: Node generation in region I

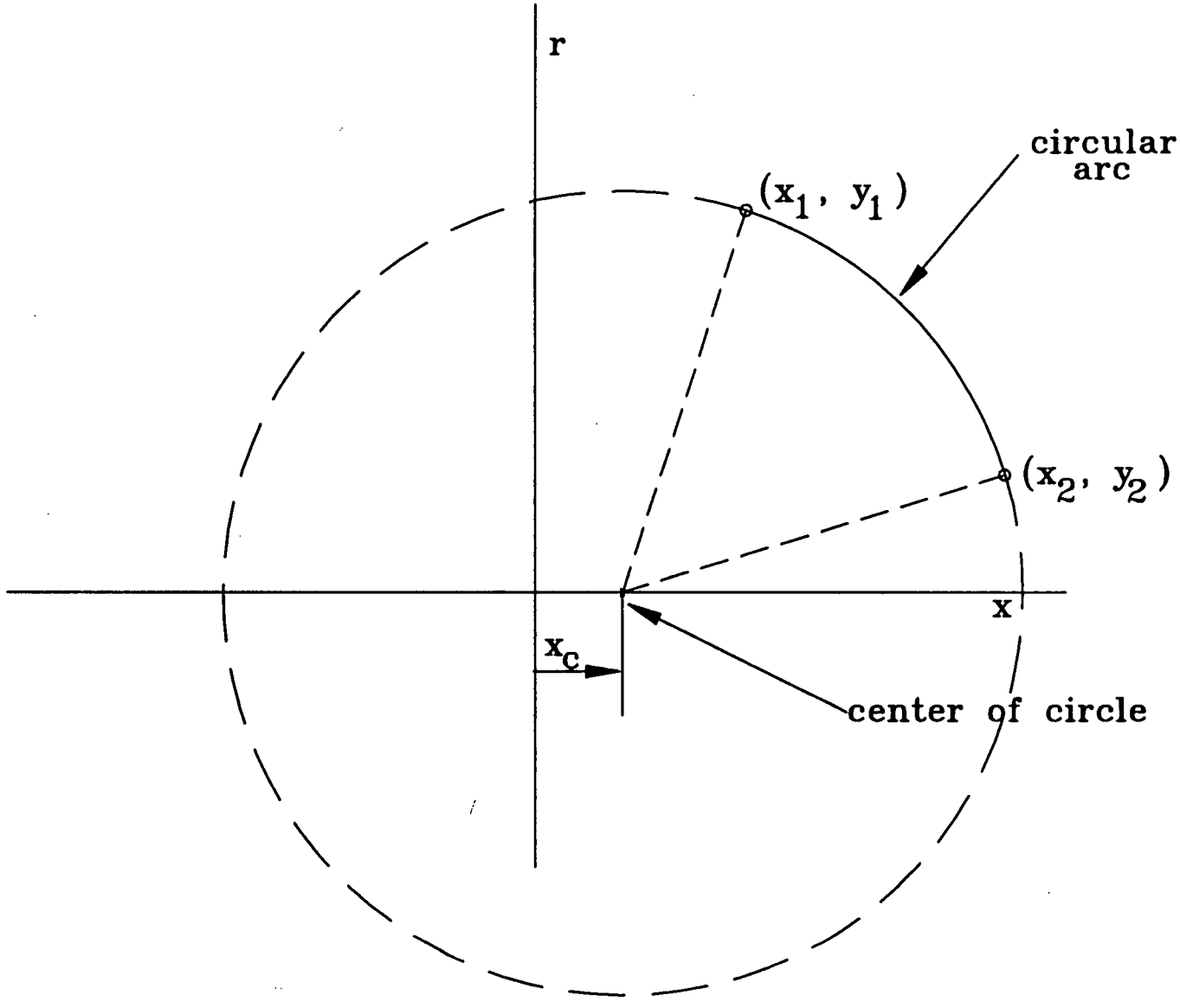

Figure 5: Geometry of a circular arc in region I

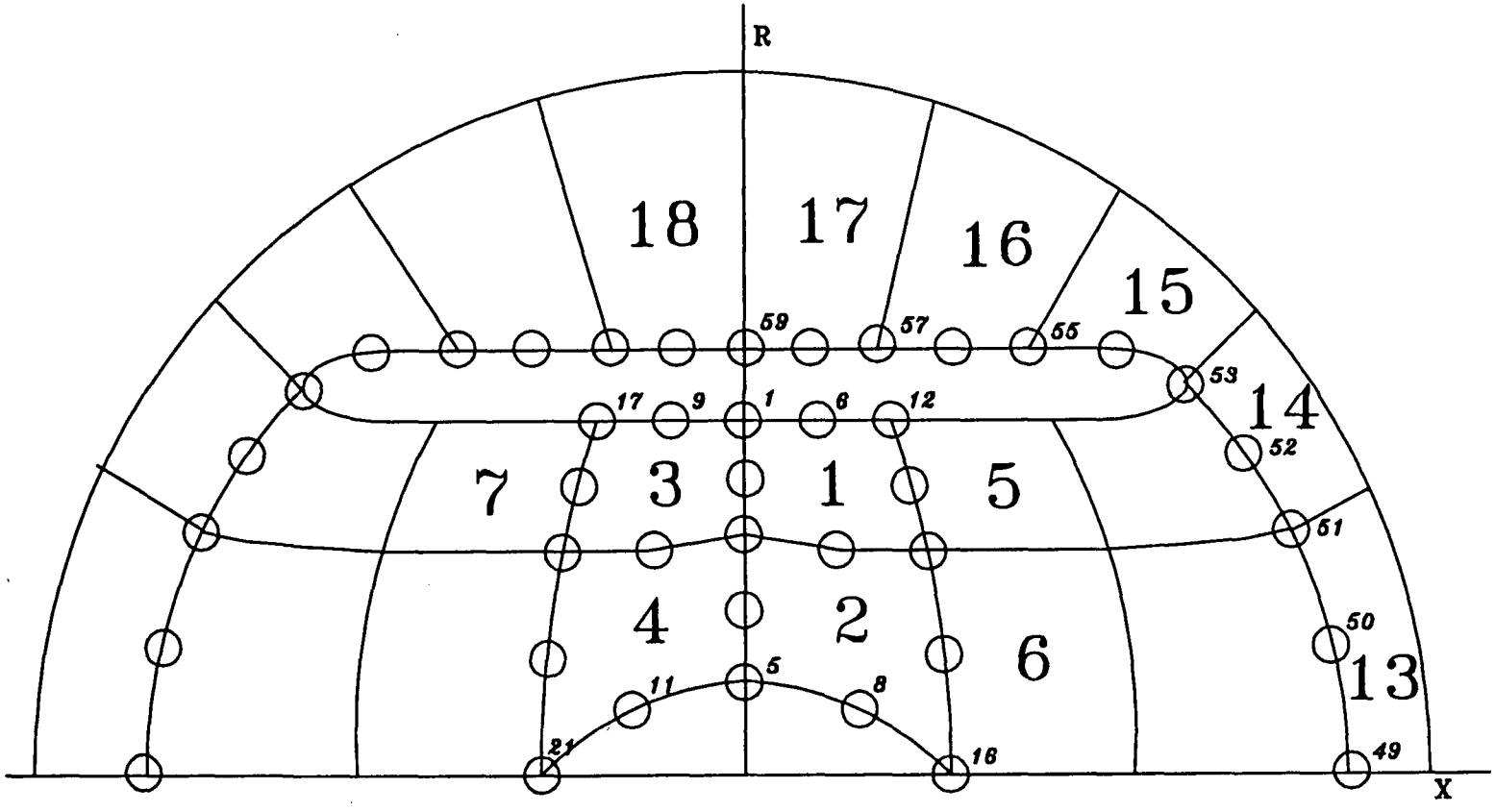

Figure 6: Element and node numbering in the finite element mesh

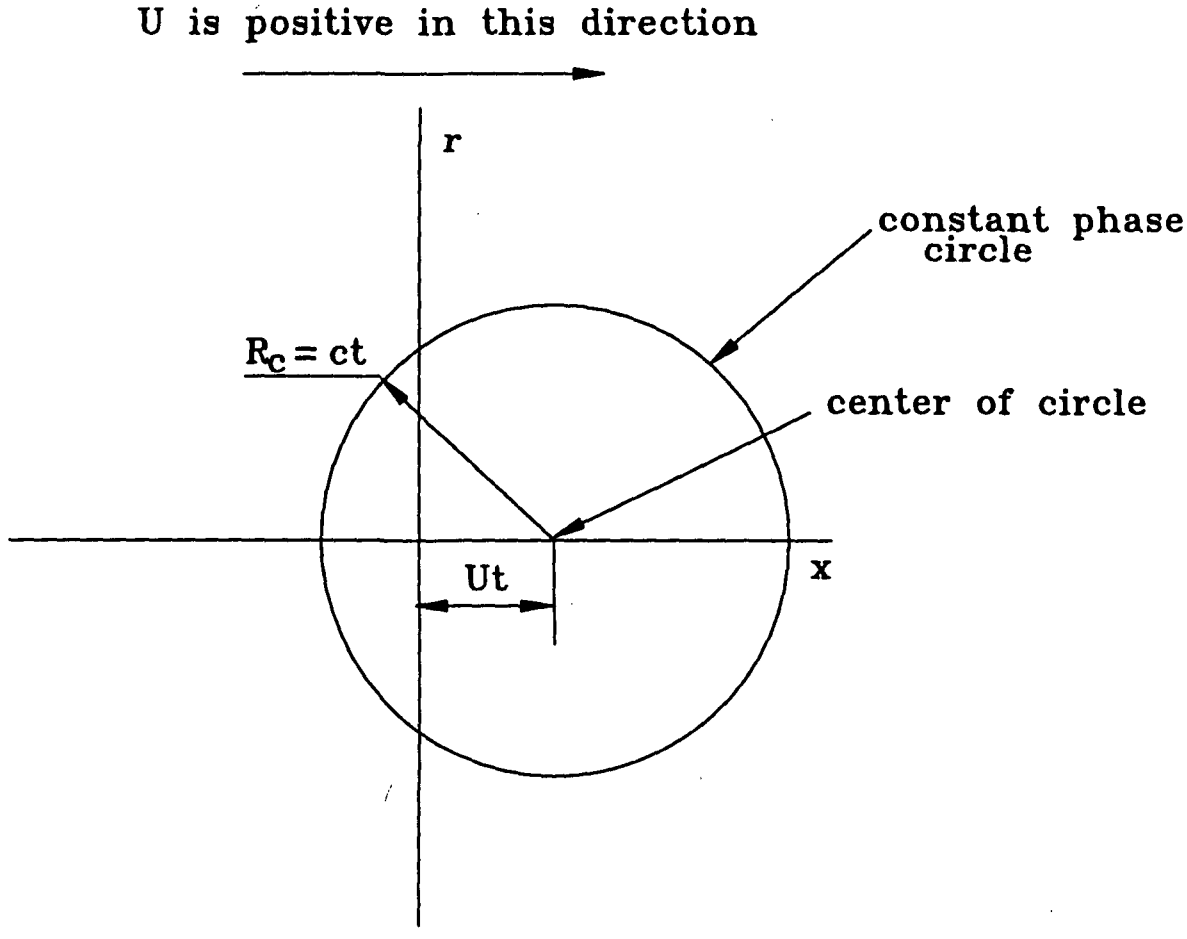

Figure 7: Geometry of a constant phase circle in uniform flow

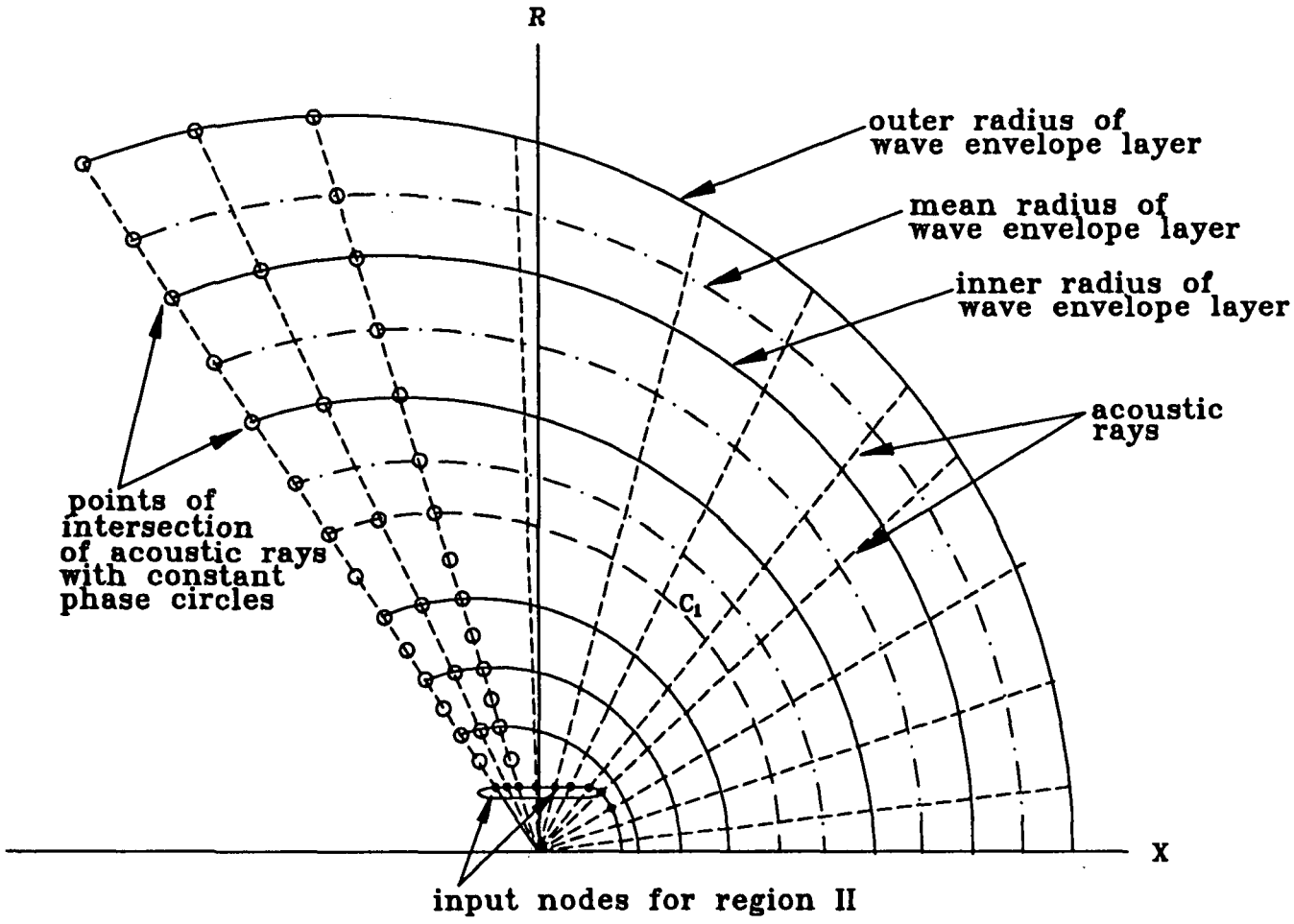

FIG. 8

Figure 8: Node generation in regions II and III

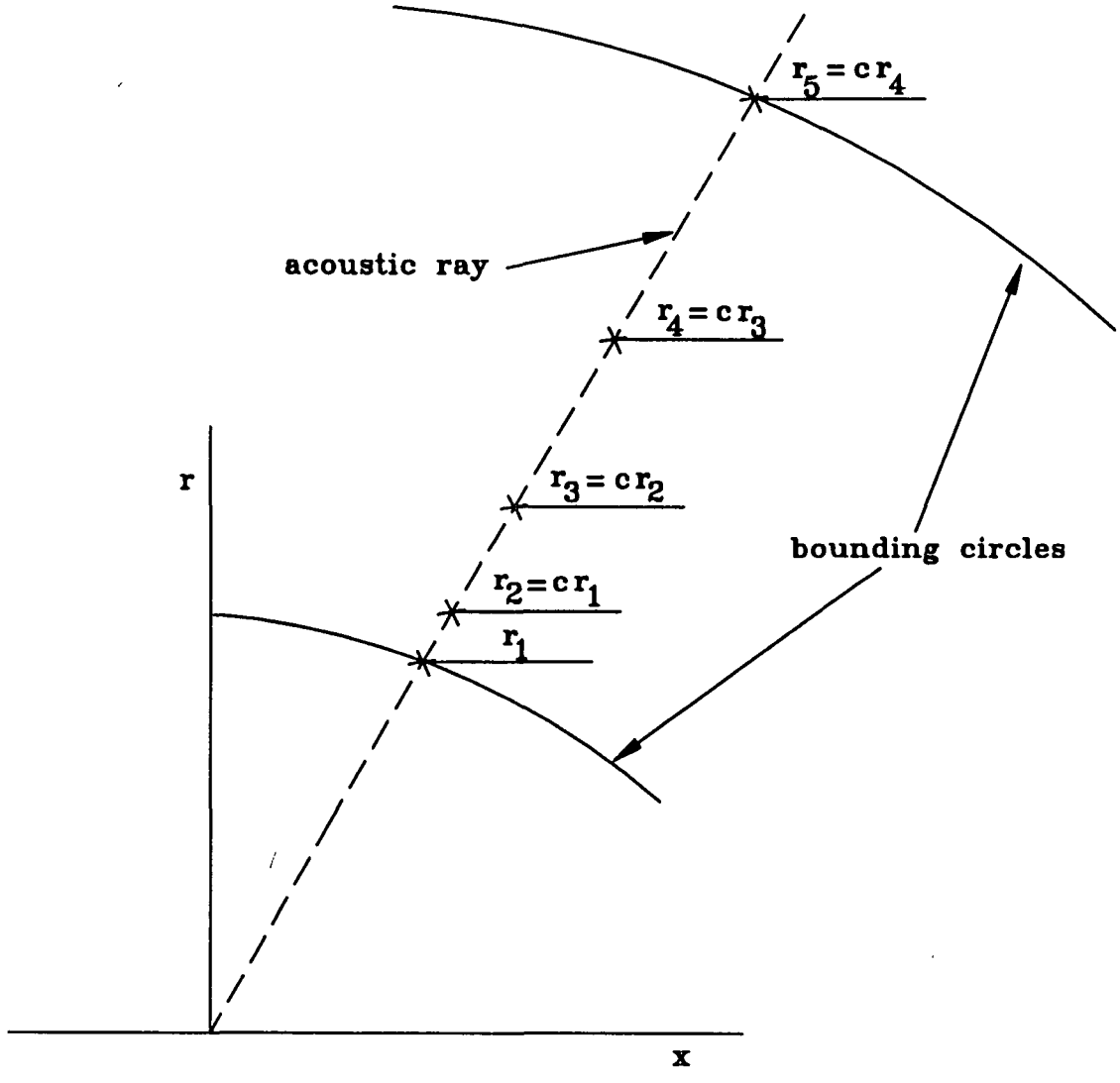

Figure 9: Geometric progression in region II

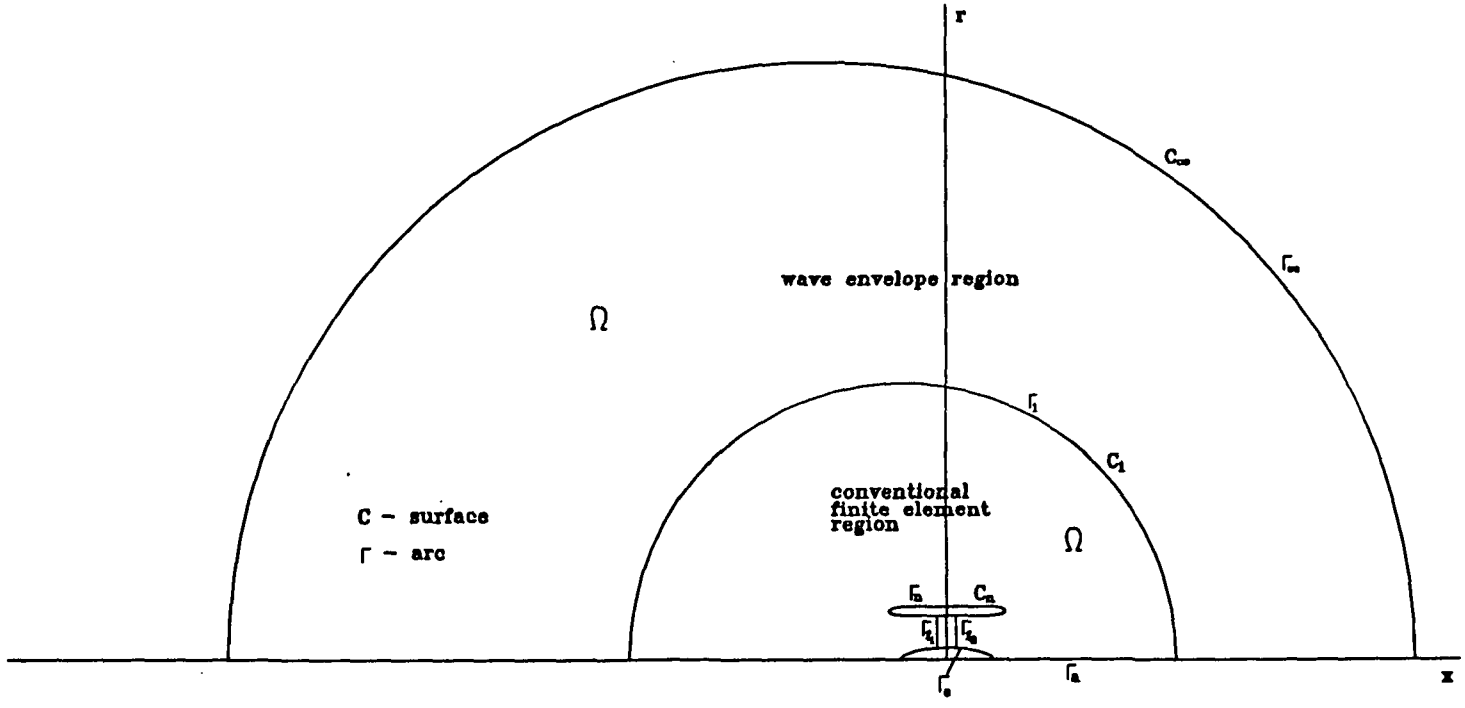

Figure 10: The computational domain

APPENDIX C

POTENTIAL FLOW CALCULATION

APPENDIX C. MEAN FLOW CALCULATIONS

A. DERIVATION OF THE FLOW PROBLEMS

Under the assumption of sufficiently low flow Mach number, the flow around the inlet of the shrouded propeller can be approximated as an incompressible one, and the equation for mean flow can be approximated by

$$\nabla^2 \phi_o = 0 \tag{1}$$

which is the Laplace equation.

In Figure 10, the curves Γ in the x-r plane correspond to surfaces in the axisymmetric space around the inlet. The axis of symmetry Γ_a is not a physical boundary of the domain. In the axisymmetric integral formulation of the problem, the boundary integral corresponding to this axis ($r = 0$) vanishes. Therefore, no boundary condition needs to be specified. The far field boundary Γ_∞ is circular (spherical in axisymmetric space). Though it is several duct radii from the inlet, the flow effects due to the presence of the inlet cannot be assumed negligible. The boundary condition on this curve will be discussed later. The nacelle Γ_n and centerbody Γ_c are impervious to flow. The curves Γ_{f_1} and Γ_{f_2} represent exit planes (convenient boundaries near the propeller where mean flow velocities are specified) fore and aft of the propeller, respectively.

Since the differential equation (1) is linear, it can be split up into four different problems, each of which can be solved separately and upon employing the method of superposition, the velocity potential of the actual flow field can be determined. The velocity potential for the mean flow is decomposed as follows:

$$\phi_o = \phi_u + \phi_p \tag{2}$$

where ϕ_u is the flow field due to the external uniform flow field only (without the

presence of the inlet) and ϕ_p is the flow perturbation due to the presence of the inlet only. The boundary condition to be applied at the boundarie Γ_∞ is not clear until and unless we formulate the problem in terms of flow perturbation. Our aim is to formulate the entire problem in such a way that the fan face and the external flow velocity do not become dependent on the perturbations; rather they govern it.

The perturbation velocity potential ϕ_p is further decomposed into

$$\phi_p = \phi_1 + \phi_2 + \phi_3 \tag{3}$$

where ϕ_1 is the perturbation potential due to flow to a blank inlet (effect of the presence of the shroud in the external uniform flow), ϕ_2 is the perturbation potential due to inlet flow through fore exit plane alone, and ϕ_3 is the perturbation potential due to inlet flow through aft exit plane only. Therefore, the four flow problems may be posed as

1. Problem I This problem represents the perturbation potential field due to a flow to a blank inlet.

$$\nabla^2\phi_1 = 0 \quad \text{in } \Omega \tag{4a}$$

$$\nabla\phi_1 \bullet \mathbf{n} = -\nabla\phi_u \bullet \mathbf{n} \quad \text{on } \Gamma_f \tag{4b}$$

$$\nabla\phi_1 \bullet \mathbf{n} = -\nabla\phi_u \bullet \mathbf{n} \quad \text{on } \Gamma_n \text{ and } \Gamma_c \tag{4c}$$

$$\nabla\phi_1 \bullet \mathbf{n} = \frac{A_1}{R^2}\mathbf{r} \bullet \mathbf{n} \quad \text{on } \Gamma_\infty \tag{4d}$$

where ϕ_u is the external uniform flow velocity potential, A_1 is a constant to be determined, $\mathbf{n}$ is the unit outward normal on the boundary and $\mathbf{r}$ is the outward radial vector on the outer boundary Γ_∞ as shown in Figure 10. It is assumed that on the outer boundary Γ_∞ the effect of the flow field is that of a simple source

placed at the origin. Hence, the velocity perturbation at the outer boundary is assumed to be radially directed inwards and inversely proportional to the square of the radial distance from the origin[1].

2. Problem II This problem represents the perturbation potential field due to inlet flow through fore exit plane alone.

$$\nabla^2\phi_2 = 0 \quad \text{in } \Omega \tag{5a}$$

$$\nabla\phi_2 \bullet \mathbf{n} = U_{f_1} \quad \text{on } \Gamma_{f_1} \tag{5b}$$

$$\nabla\phi_2 \bullet \mathbf{n} = 0 \quad \text{on } \Gamma_n \text{ and } \Gamma_c \tag{5c}$$

$$\nabla\phi_2 \bullet \mathbf{n} = -\frac{A_2}{R^2}\mathbf{r} \bullet \mathbf{n} \quad \text{on } \Gamma_\infty \tag{5d}$$

where U_{f_1} is the uniform exit face velocity, A_2 is a constant to be determined, $\mathbf{n}$ is the unit outward normal on the boundary and $\mathbf{r}$ is the outward radial vector on the outer boundary Γ_∞ as shown in Figure 10. Here also the flow at the outer boundary is assumed to be that of a simple source placed at the origin. The flow perturbation is assumed to be radially outwards and varying as $1/R^2$, where R is the radial distance from the origin.

1. Problem III This problem represents the perturbation potential field due to inlet flow through aft exit plane alone.

$$\nabla^2\phi_3 = 0 \quad \text{in } \Omega \tag{6a}$$

$$\nabla\phi_3 \bullet \mathbf{n} = -U_{f_2} \quad \text{on } \Gamma_{f_2} \tag{6b}$$

$$\nabla\phi_3 \bullet \mathbf{n} = 0 \quad \text{on } \Gamma_n \text{ and } \Gamma_c \tag{6c}$$

[1]The velocity field of a simple source varies as $1/R^2$.

$$\nabla\phi_3 \bullet \mathbf{n} = \frac{A_3}{R^2}\mathbf{r} \bullet \mathbf{n} \quad \text{on } \Gamma_\infty \tag{6d}$$

where U_{f_2} is the uniform fan face velocity, A_2 is a constant to be determined, $\mathbf{n}$ is the unit outward normal on the boundary and $\mathbf{r}$ is the outward radial vector on the outer boundary Γ_∞ as shown in Figure 10. Here again the flow at the outer boundary is assumed to be that of a simple source placed at the origin. The flow perturbation is assumed to be radially outwards and varying as $1/R^2$, where R is the radial distance from the origin.

3. Problem IV The uniform external flow field is generated by

$$\nabla^2\phi_u = 0 \quad \text{in } \Omega \tag{7a}$$

$$\nabla\phi_u \bullet \mathbf{n} = U_o \mathbf{i} \bullet \mathbf{n} \quad \text{on } \Gamma_\infty \text{ and } \Gamma_b \tag{7b}$$

where U_o is the external uniform flow velocity.

Problems I through III are boundary value problems with Neumann boundary conditions. Solutions to these problems are non-unique if the value of the unknown variable is not specified at one point in the domain Ω. The problems also have to satisfy a compatibility criterion which balances the flux of flow across different boundaries. This criterion fixes the values of the constants A_1 through A_3 relative to the flow parameters and, therefore, they are not arbitrary.

A linear superposition of the problems I through III gives us the overall boundary value problem of the mean flow

$$\nabla^2\phi_o = 0 \quad \text{in } \Omega \tag{8a}$$

$$\nabla\phi_o \bullet \mathbf{n} = U_f \quad \text{on } \Gamma_f \tag{8b}$$

$$\nabla\phi_o \bullet \mathbf{n} = 0 \quad \text{on } \Gamma_n \text{ and } \Gamma_c \tag{8c}$$

$$\nabla\phi_o \bullet \mathbf{n} = \frac{A_1}{R^2}\mathbf{r} \bullet \mathbf{n} - \frac{A_2}{R^2}\mathbf{r} \bullet \mathbf{n} + \frac{A_3}{R^2}\mathbf{r} \bullet \mathbf{n} + U_o \mathbf{i} \bullet \mathbf{n} \quad \text{on } \Gamma_\infty \tag{8d}$$

The flow perturbation effects of the inlet at the outer boundary are small due to the distance of the boundary from the inlet. Also it is to be noted that the perturbation boundary condition at the outer boundary Γ_∞ for problems I through III tend to balance each other. Therefore, under these conditions the superposed boundary condition (8d) on Γ_∞ can be written approximately as $\nabla\phi_o \bullet \mathbf{n} \approx U_o \mathbf{i} \bullet \mathbf{n}$. The superposition of the elementary solutions from problems I, II, III, and IV is based on the assumption that the outer boundary condition is imposed at a large distance from the inlet. This effectively makes U_f and U_o independent of each other. For a given value of U_o, any value of U_f can be chosen once the elementary solutions are available. Variations in U_o requires new potential flow solutions to be computed because the mesh depends on U_o.

B. FINITE ELEMENT FORMULATION

1. Flow to a blank inlet Since the mean flow field is axisymmetric, there is no variation of flow variables in the angular direction. Therefore, the test and trial functions are independent of the angular coordinate θ. Let ψ be a real valued smooth function defined in the axisymmetric domain Ω. Multiplication of the Laplace equation with the test function ψ and integration over the domain yields

$$\int_\Omega \nabla^2\phi_1 \psi \, d\Omega = 0 \tag{9}$$

By using Green's theorem, it is determined that

$$\int_\Omega \nabla\phi_1 \bullet \nabla\psi \, d\Omega = \int_S \psi \nabla\phi_1 \bullet \mathbf{n} \, dS \tag{10}$$

where S denotes surfaces of the axisymmetric volume Ω. Since the problem is independent of θ, the volume integral becomes a surface integral in the x-r plane,

and the surface integral becomes a line integral, so that

$$\int_r \int_x \left(\frac{\partial \phi_1}{\partial x}\frac{\partial \psi}{\partial x} + \frac{\partial \phi_1}{\partial r}\frac{\partial \psi}{\partial r}\right) r dx dr = \int_\Gamma \psi \nabla \phi_1 \bullet \mathbf{n}\, r d\Gamma \tag{11}$$

Incorporation of the natural boundary conditions into equation (62) results in the weak form of the problem

$$\int_r \int_x \left(\frac{\partial \phi_1}{\partial x}\frac{\partial \psi}{\partial x} + \frac{\partial \phi_1}{\partial r}\frac{\partial \psi}{\partial r}\right) r dx dr = -\int_{\Gamma'} \psi \nabla \phi_o \bullet \mathbf{n}\, r d\Gamma + A_1 \int_{\Gamma_\infty} \psi \frac{1}{R^2}\mathbf{r} \bullet \mathbf{n}\, r d\Gamma \tag{12}$$

Therefore the following weak problem may be posed: find $\phi_1 : \Omega \longrightarrow \mathbf{R}^2 \ni$ equation (63) holds $\forall$ smooth $\psi : \Omega \longrightarrow \mathbf{R}^2$. It is to be noted that ϕ_1 and ψ are suitable classes of functions whose derivatives are square integrable (from the space H^1).

A standard Galerkin finite element approximation has been used for the matrix formulation. Basis functions $N_1, N_2, \ldots, N_n$ have been chosen from a finite dimensional (of dimension n) subspace of H^1. Hence, the test and trial functions can be finitely approximated as

$$\psi = c_i N_i(x, r) \tag{13}$$

$$\phi_1 = d_j N_j(x, r) \tag{14}$$

where c_i's and d_j's are suitable scalars[2]. Substitution of equations (64) and (65) in (63) results in the matrix formulation of the problem

$$\underbrace{\left[\int_r \int_x \left(\frac{\partial N_i}{\partial x}\frac{\partial N_j}{\partial x} + \frac{\partial N_i}{\partial r}\frac{\partial N_j}{\partial r}\right) r dx dr\right]}_{K'_{ij}} d_j =$$

$$\underbrace{-\int_{\Gamma_\prime} N_i \nabla \phi_o \bullet \mathbf{n}\, r d\Gamma + A_1 \int_{\Gamma_\infty} N_i \frac{1}{R^2}\mathbf{r} \bullet \mathbf{n}\, r d\Gamma}_{F'_i} \tag{15}$$

where K'_{ij} is the i, j entry of the stiffness matrix $[K']$ and F'_i is the i^{th} entry in the load vector $\{F'\}$.

---

[2]Since ϕ is being suitably interpolated between the nodes, d_j's here imply nodal values of the mean flow potential.

2. Inlet flow through fore exit plane only In a procedure similar to that of problem I, the weak form of problem II is

$$\int_r \int_x \left(\frac{\partial \phi_2}{\partial x}\frac{\partial \psi}{\partial x} + \frac{\partial \phi_2}{\partial r}\frac{\partial \psi}{\partial r}\right) r dx dr = U_{f_1} \int_{\Gamma_f} \psi\, r d\Gamma - A_2 \int_{\Gamma_\infty} \psi \frac{1}{R^2} \mathbf{r} \bullet \mathbf{n}\, r d\Gamma \qquad (16)$$

where $\Gamma' = \Gamma_n \cup \Gamma_f \cup \Gamma_c$ and, ϕ_2 and ψ are from H^1.

As in problem I, a standard Galerkin finite element approximation has been used for the matrix formulation. The matrix formulation of problem II yields

$$\underbrace{\left[\int_r \int_x \left(\frac{\partial N_i}{\partial x}\frac{\partial N_j}{\partial x} + \frac{\partial N_i}{\partial r}\frac{\partial N_j}{\partial r}\right) r dx dr\right]}_{K_{ij}} d_j = \underbrace{U_{f_1} \int_{\Gamma_f} N_i\, r d\Gamma - A_2 \int_{\Gamma_\infty} N_i \frac{1}{R^2} \mathbf{r} \bullet \mathbf{n}\, r d\Gamma}_{F_i} \qquad (17)$$

where K_{ij} is the i, j entry of the stiffness matrix $[K]$ and F_i is the i^{th} entry in the load vector $\{F\}$.

Details of the stiffness matrix and load vector calculations are dealt with in the next sub-section. The constants A_1 and A_2 for the problems I and II are found by imposing the compatibility condition which balances the flux across the boundaries. For problem I, it balances the flux across the nacelle, centerbody and fan face with the flux across Γ_∞, i.e.,

$$\int_{\Gamma'} \nabla \phi_o \bullet \mathbf{n}\, r d\Gamma = A_1 \int_{\Gamma_\infty} \frac{1}{R^2} \mathbf{r} \bullet \mathbf{n}\, r d\Gamma$$

or,

$$A_1 = \frac{\int_{\Gamma'} \nabla \phi_o \bullet \mathbf{n}\, r d\Gamma}{\int_{\Gamma_\infty} \frac{1}{R^2} \mathbf{r} \bullet \mathbf{n}\, r d\Gamma} \qquad (18)$$

For problem II, it balances the flux across the fan face with the flux across the outer boundary Γ_∞, i.e.,

$$U_{f_1} \int_{\Gamma_f} r d\Gamma = A_2 \int_{\Gamma_\infty} \frac{1}{R^2} \mathbf{r} \bullet \mathbf{n}\, r d\Gamma$$

or,

$$A_2 = \frac{U_{f_1} \int_{\Gamma_f} r d\Gamma}{\int_{\Gamma_\infty} \frac{1}{R^2} \mathbf{r} \bullet \mathbf{n}\, r d\Gamma} \qquad (19)$$

The constant A_3 is calculated likewise.

C. FINITE ELEMENT CALCULATIONS

The global stiffness matrices and the global load vectors as defined in equations (66) and (68), can be written as the composition of the element stiffness matrices and element load vectors respectively. Therefore, for example, in problem II, we can write

$$[K] = \sum^{n_e} [K^e]$$

$$\{F\} = \sum^{n_e} \{F^e\}$$

where n_e is the number of elements in the domain. The element stiffness matrix $[K^e]$ and the element load vector $\{F^e\}$ for the problem are given by

$$K_{ij}^e = \int_{\Omega_e} \left(\frac{\partial N_i^e}{\partial x}\frac{\partial N_j^e}{\partial x} + \frac{\partial N_i^e}{\partial r}\frac{\partial N_j^e}{\partial r}\right) r\,dx\,dr$$

$$F_i^e = U_{f_1} \int_{\Gamma_f^e} N_i^e\, r\,d\Gamma - A_1 \int_{\Gamma_\infty^e} N_i^e \frac{1}{R^2}\mathbf{r}\bullet\mathbf{n}\, r\,d\Gamma$$

where $\int_{\Omega_e}$ is the surface integral over the domain of the element, $\int_{\Gamma_f^e}$ and $\int_{\Gamma_\infty^e}$ are line integrals along element boundaries on the fan face and the outer boundary respectively, and N_i^e is the shape function of the i^{th} node of the element.

Finite element calculations are done based on a parent element with local coordinates ς and η as shown in Figure 4. The element shape functions $\tilde{N}_i^e$ corresponding to each node i in the parent element are standard functions and therefore known.

1. Surface Integrals To perform the finite element calculations on a parent element, an element map is constructed. The transformation under which each

element Ω_e in the mesh is the image of a fixed parent element under a coordinate map T_e is constructed as

$$T_e : x = \sum_{i=1}^{nodes} x_i \tilde{N}_i^e(\zeta, \eta) \tag{20a}$$

$$T_e : r = \sum_{i=1}^{nodes} r_i \tilde{N}_i^e(\zeta, \eta) \tag{20b}$$

where *nodes* is the number of nodes on the parent element, and is 8 or 9 depending on whether it is an eight or nine-node element. The element Ω_e to which T_e maps the parent element is completely determined by specifying the x, r coordinates (x_i, r_i) of all the nodal points of Ω_e. Element shape functions $N_i^e(x, r)$ are simply obtained from standard parent element shape functions $\tilde{N}_i^e(\zeta, \eta)$ by

$$N_i^e(x, r) = \tilde{N}_i^e(\zeta(x, r), \eta(x, r)) \tag{21}$$

The derivatives of shape functions are obtained by the chain rule of differentiation,

$$\frac{\partial N_i}{\partial x} = \frac{\partial \tilde{N}_i}{\partial \zeta}\frac{\partial \zeta}{\partial x} + \frac{\partial \tilde{N}_i}{\partial \eta}\frac{\partial \eta}{\partial x} \tag{22a}$$

$$\frac{\partial N_i}{\partial r} = \frac{\partial \tilde{N}_i}{\partial \zeta}\frac{\partial \zeta}{\partial r} + \frac{\partial \tilde{N}_i}{\partial \eta}\frac{\partial \eta}{\partial r} \tag{22b}$$

According to the element map,

$$\frac{\partial x}{\partial \zeta} = \sum_{k=1}^{nodes} x_k \frac{\partial \tilde{N}_k^e}{\partial \zeta} \tag{23a}$$

$$\frac{\partial x}{\partial \eta} = \sum_{k=1}^{nodes} x_k \frac{\partial \tilde{N}_k^e}{\partial \eta} \tag{23b}$$

$$\frac{\partial r}{\partial \zeta} = \sum_{k=1}^{nodes} r_k \frac{\partial \tilde{N}_k^e}{\partial \zeta} \tag{23c}$$

$$\frac{\partial r}{\partial \eta} = \sum_{k=1}^{nodes} r_k \frac{\partial \tilde{N}_k^e}{\partial \eta} \tag{23d}$$

By using the above relations (equations (20) through (23)), the element stiffness expression K_{ij}^e may be expressed as

$$\int_{\Omega_e} f(x, r)\, r dr dx = \int_{\Omega_p} \tilde{g}(\zeta, \eta)\, \tilde{r}(\zeta, \eta) J(\zeta, \eta) d\zeta d\eta \tag{24}$$

where $\int_{\Omega_p}$ is the domain integral over the parent element and $J(\zeta,\eta)$ is the Jacobian of the transformation T_e given by

$$J(\zeta,\eta) = \frac{\partial x}{\partial \zeta}\frac{\partial r}{\partial \eta} - \frac{\partial x}{\partial \eta}\frac{\partial r}{\partial \zeta} \tag{25}$$

A standard 4×4 Gaussian quadrature rule has been used to evaluate the integral. It is important to note that the mean flow calculations have been done both with and without the wave envelope elements. In one case, no distinction has been made between the elements in regions I and II and the elements in region III. All the regions have isoparametric rectangular finite elements. In another case, shape functions for the wave envelope elements in region III, differ from the rest in the mesh due to the fact that they simulate the inverse square decay behaviour as expected in a field due to a simple source. Mathematically a shape function may be expressed as

$$N_i^{we} = N_i^e\left(\frac{r_i}{r}\right) \tag{26}$$

where N_i^e is the standard shape function of node i at radius r_i. The results in both cases were virtually identical for the flow velocity we are concerned with. For compatibility with the radiation calculations the wave envelope elements were retained.

2. Boundary Integrals Three-node quadratic line elements lie along the boundaries and the generation of their topology and their nodal connectivity have already been discussed in the mesh generation scheme. The calculations of the line integrals are carried out by integrating along those sides of the parent element that are mapped onto the sides Γ^e of the actual element Ω_e along which natural boundary conditions are prescribed. For definiteness, it has been assumed that the side $\zeta = 1$ has been mapped onto Γ^e. The line integrals have been parametrized with respect to η.

The shape functions used for the line integrals are identical to the standard shape functions for the three-node Lagrangian line element. Element maps are created as discussed before and the elemental arc length is found by

$$d\Gamma = \sqrt{dx^2 + dr^2}$$

or,

$$d\Gamma = \underbrace{\sqrt{(\frac{\partial x}{\partial \eta})^2 + (\frac{\partial r}{\partial \eta})^2}}_{j} d\eta \tag{27}$$

where j is the jacobian of the transfomation of η onto the arc length parameter in the x-r plane. The dot products, $\nabla\phi_o \bullet \mathbf{n}$ for problem I and $\mathbf{r} \bullet \mathbf{n}$ for problems I through III need to be computed at each node on the relevant boundaries to evaluate the line integrals. Note that the constants A_1 through A_3 need to be evaluated before constructing the load vector.

D. THE SOLUTION PROCEDURE

All of the boundary conditions are of the Neumann type and the differential equation is the Laplace equation. Hence, there is no unique solution to the problems unless a reference value of the mean flow velocity is specified at any point in the domain. This does not affect the results because we are interested in the derivatives of the potential and not in the absolute values of the mean flow potential. By penalization, the potential has been made zero at an arbritary point on the outer boundary Γ_∞. This penalization has been made at the elemental level. When the stiffness matrix of the element which occupies the penalized node is calculated, a very large value (1.0e15) is added to the diagonal entry in the matrix corresponding to that boundary node. Hence the velocity potential at that node is forced to zero after solution. The penalized stiffess matrix for that boundary

element looks like the following :

$$\begin{bmatrix} K_{11} & \dots & K_{1m} & \dots & K_{1n} \\ \vdots & \vdots & \vdots & \vdots & \vdots \\ K_{m1} & \dots & K_{mm} + \frac{1}{\epsilon} & \dots & K_{mn} \\ \vdots & \vdots & \vdots & \vdots & \vdots \\ K_{n1} & \dots & K_{nm} & \dots & K_{nn} \end{bmatrix}$$

where m is the penalized node number (local) and ϵ (1.0e-15) is the penalty parameter. As a check, penalization was carried out at a different point in the domain, and the solution was found to differ from the previous solution by an arbitrary constant only.

Since the penalization is carried out at the element level, the stiffess matrix and the load vector are never stored in assembled form. As each element stiffness matrix and load vector is formed, it is written down onto disk along with its nodal connectivity. The frontal solution method of Bruce Irons has been used to solve the algebraic system of equations $[K]\{\phi\} = \{F\}$. The principles of this technique are implied by the Gaussian process of forward elmination and back substitution. The frontal process alternates between accumulation of element coefficients (assembly) and elimination. Whenever an element is assembled its nodes are kept in active storage until their elimination. The active in-core storage at a point of time depends only on the "frontwidth" (number of active nodes at that time) which is much smaller than the dimension of the assembled matrix. This drastic reduction in in-core storage is the most important aspect of this scheme. Details of the scheme are, however, not discussed here.

E. SUPERPOSITION OF THE SOLUTION FROM THE THREE PROBLEMS

After the solutions to problems I through III are obtained, they are added to the exterior field velocity potential to obtain the overall mean flow velocity potential of the flow field. Solution to the problem IV is the uniform flow field

whose velocity potential is given by

$$\phi_u = U_o x \tag{28}$$

The overall mean flow velocity potential is found out by pointwise addition of the solution vectors from the four flow problems

$$\phi_o = \phi_1 + \phi_2 + \phi_3 + \phi_u \tag{29}$$

However, the solutions to the problems I through IV have been obtained by an input of unit velocity at the exit planes, fore and aft, and in the exterior flow field i.e. $U_{f_1} = 1$, $U_{f_2} = 1$, and $U_o = 1$ respectively. Therefore, if the exit planes (fore and aft) flow Mach number and exterior flow field Mach number are M_{f_1}, M_{f_2}, and M_u respectively, the superposed solution is found by

$$\phi_o = M_u(\phi_1 + \phi_u) + M_{f_1}\phi_2 + M_{f_2}\phi_3 \tag{30}$$